FRICTION STIR PROCESSING OF ALUMINUM ALLOYS

by

Ning Sun

A Dissertation

Submitted to the Faculty

Of the

WORCESTER POLYTECHNIC INSTITUTE

in partial fulfillment of the requirements for the

Degree of Doctor of Philosophy

in

Material Science & Engineering

October 2012

APPROVED:

Dr. Diran Apelian, Major Advisor

Dr. Richard D. Sisson, Head of Department

Abstract

Friction stir processing (FSP) has been developed based on the basic principles of friction stir welding (FSW), a solid-state joining process originally developed for aluminum alloys. What is attractive about FSP is that it can be incorporated in the overall manufacturing cycle as a post-processing step during the machining operation to provide localized modification and control of microstructures in near-surface layers of metallic components. FSP has emerged as an important post-processing technique, and has been identified as a process that may have a high impact, and perhaps is a disruptive manufacturing process. In this study, FSP has been applied to Al cast alloy A206, which is a high strength, widely used cast alloy in the manufacturing industry. Motivations behind this work are to (1) investigate the feasibility of FSP on manipulating the cast microstructure and strengthening the material, and (2) to explore the viability of FSP to produce a localized particle reinforced zone in cast A206 aluminum components.

The thesis will show that we have optimized FSP for processing of Al alloys to locally manipulate the cast microstructure, eliminate casting defects, and attain grain refinement and second phase homogenization. We have established the mechanism leading to the microstructure evolution and have evaluated the resultant mechanical properties, i.e. hardness, tensile property and fatigue properties. We have also synthesized a localized composite material in the A206 work piece with three different reinforcement materials via FSP. These results will be presented and discussed.

Acknowledgements

First and foremost, I would like to extend my deepest gratitude to my advisor, Dr. Diran Apelian for his outstanding guidance, support, enthusiasm and encouragements throughout my graduate studies and research progress. Further appreciation is due to the members of the dissertation committee, professors Richard D. Sisson Jr., Makhlouf M. Makhlouf, Diana Lados, and ACRC Focus Group members: Dr. Kevin Anderson and Dr. David Weiss for their encouragement, critical comments and stimulating questions.

I would like to thank the member of the Advanced Casting Research Center (ACRC) at the Metal Processing for their support of this work, and their continued support of research focused on the science and technology of metal casting at Worcester Polytechnic Institute. I am so grateful for all the help that I received fully as I was making my way through this journey.

My friends and colleagues in the Materials Science and Engineering department and the Metal Processing Institute made my years at WPI an enjoyable experience. Being surrounded by such a positive group of people bestowed the feelings of family and forged lifelong relationships. Thank you for providing the support while pursuing my academic and personal goals. I would like to specifically thank Libo Wang and Toby Bergstrum.

Finally, but most importantly, I would like to pay my deepest gratitude and love to my family. Their love and belief in me lit my path in life and helped me strive to reach towards horizon and beyond.

Table of Content

Executive Summary

Introduction

The casting process is a complex one in that three key transport processes take place simultaneously: heat flow, fluid flow, and mass flow. This complexity gives rise to heterogeneities within the microstructure, such as porosity and other defects. Ironically, successful castings are made not only by controlling the microstructure, but also through controlling (or management of) defects. In this vein, we have pursued a processing method, friction stir processing (FSP), by which one can locally manipulate the structure, as well as locally strengthen it. Friction Stir Processing (FSP) has been studied and applied to Al cast alloys for such applications. What is attractive about FSP is that it can be incorporated in the overall manufacturing cycle as a post-processing step during the machining operation. Friction Stir Processing (FSP) has shown the capability of eliminating casting defects and refining the microstructure at the processed area, resulting in improved mechanical properties. FSP has also demonstrated to be an innovative means of producing components with localized composite structures.

Though extensive studies have been conducted on FSP for Al alloys, the applications have been mostly in wrought alloys but no well-established process was developed for cast alloys. The work to date using FSP in Al cast alloys has not addressed the fundamental mechanism governing the evolution of microstructure as well as the resultant mechanical properties – static and dynamic. The stirring action of FSP deforms the workpiece vigorously, and thus the alloy's formability influences FSP functionality. The results of studies and the developed process for wrought alloys with high formability may not be applicable to cast alloys. Using FSP in cast alloys should have some specific characteristics different from those of wrought alloys. The low formability makes manufacturing cast alloys more difficult and produces challenges using FSP; thus, more detailed studies are needed. In this vein, the current investigation was initiated with the objectives of moving forward the study, identifying the specific features, understanding the mechanisms, evaluating dynamic properties, creating a larger database for developing the practical technique and exploring the potential of applying FSP in Al cast alloys.

Objectives

- Investigate the microstructure of Al A206 cast alloy that was processed by FSP and establish the mechanism for microstructure evolution
- Evaluate the enhancement of the mechanical properties Al A206 cast alloy via FSP
- Investigate the potential of FSP to form a localized particle reinforcement zone in the standard Al cast component

Methodology

In order to achieve the above objectives, the following methodologies and strategies were pursued:

- ***Phase I*** – Investigate the microstructure of Al A206 cast alloy that was processed by FSP and establish the mechanism of microstructure evolution
    - Establish a FSP setup, assess and validate its capabilities
    - Run FSP with the developed setup and appropriate working parameters
    - Conduct microstructural analysis with the optical microscope, SEM, TEM, and EBSD technique to find out the microstructure features of the FSP processed material
    - Establish the potential mechanism for microstructure evolution

- ***Phase II*** – Evaluate the enhancement of the mechanical properties A206 via FSP. These properties were studied:
    - Microhardness
    - Tensile property
    - Fatigue property

- ***Phase III*** – Investigate the potential of FSP to form a localized particle reinforced zone or a composite material in the standard Al cast component
    - Fabricate the composite material by using nano-sized Ta powders
    - Fabricate the composite material by using nano-sized SiC powders
    - Fabricate the composite material by emplacing discontinuous reinforced aluminum (DRA) into the A206 work piece
    - Investigate effects of some key parameters, i.e., the number of FSP passes, amount of the reinforcement material
    - Conduct the microhardness test in the localized particle reinforced zone

Outcomes/Conclusions

In this study, we have optimized FSP for processing of Al alloys to locally manipulate the cast microstructure, achieving grain refinement, porosity elimination, and second phase homogenization. We have established the mechanism of microstructure evolution and evaluated the resultant mechanical properties. We have also synthesized a localized composite material in the A206 work piece with three different reinforcement materials via FSP.

Thesis Organization:

The thesis consists of an executive summary following by three main chapters and six appendices. Chapter I is "Article I - Microstructure Evolution of cast Al A206 via Friction Stir Processing"; Chapter II is "Article II - Localized Strengthening of cast Al A206 via Friction Stir Processing"; Chapter III is "Article III: Composite Fabrication in cast Al A206 via Friction Stir Processing"; these articles are three archival journal manuscripts. Appendix F is a compendium of all papers we have presented at various meetings.

The three main articles of the thesis – the three Chapters on microstructure evolution; on mechanical properties; and on composite manufacture are briefly summarized below, and the full text follows in Chapters 1, 2, and 3, respectively.

Article I: Microstructure Evolution of Cast Al A206 via Friction Stir Processing (Submitted to International J. of Metal Casting)

FSP was applied to locally manipulate the cast aluminum alloy A206 microstructure. In doing this, porosity and the dendritic microstructure have been eliminated. Second phase particles were distributed uniformly in the aluminum matrix after FSP, and the size and aspect ratio of these particles decreased significantly. The FSP nugget contained fine equiaxed grains with high-angle boundaries.

The dominant mechanism leading to grain refinement was continuous dynamic recrystallization. High misorientation angles were achieved via subgrain rotation, lattice rotation, and high-strain deformation-induced grain subdivision. The temperature and strain rate of the deformed material were two important factors that influenced the recrystallized grain structure. Refined grains with different diameters were observed along the vertical direction of the FSP nugget due to various temperature and strain rate conditions.

The appearance of the onion ring pattern was due to a periodic texture variation. The EBSD map showed an alternating existence of the strong <110> orientation and random crystallographic orientations. The as-cast A206 specimen had a random texture on the {111} pole figure, whereas the FSP nugget was dominated by a rotated cube texture, which was the typical texture of the recrystallized material. At a few locations within the onion ring, the {111} pole figure showed the B/ $\overline{B}$ + C components simple shear texture.

Article II: Localized Strengthening of Cast Al A206 via Friction Stir Processing (Submitted to Met. And Mat. Transactions)

FSP resulted in an increase in the average microhardness value and a reduction in the microhardness scatter. The improved microhardness property was attributed to grain refinement, precipitation hardening, cast defect alleviation, and uniform fine second phase particle dispersion.

FSP resulted in the simultaneous improvement in the strength and ductility of the A206 alloy. The yield strength was increased due to dislocation pinning/grain boundary strengthening. The enhanced ductility was due to a higher work hardening rate. FSP was applied on T4 and T7 heat-treated A206 work pieces. Strengthening phases precipitated in pre-FSP heat treatments went into solution during FSP and the thermal-cycle was inadequate for the strengthening phases to re-precipitate during/after FSP. Post-FSP heat treatments resulted in further improvement of tensile properties. Grain growth occurred when the solution treatment of the FSPed specimen was carried out in a conventional furnace. The abnormal grain growth can be prevented or alleviated in two ways: (i) using

a higher heating rate for the solution treatment, or (ii) introducing fine particles that have high thermal resistance to increase the pinning effect.

Fatigue properties of the FSPed A206 and as-cast A206 were investigated by running ultrasonic fatigue tests. The S-N curve of the FSPed specimen was shifted to the region where both the stress amplitude and the fatigue life were higher. The fatigue strength of the material at 10^8 cycles was estimated via the staircase test method. The fatigue endurance limit was two times in value after FSP compared with the limit of the as-cast A206. The improved fatigue property was due to the increased fracture resistance in both the crack initiation stage and the crack growth and propagation stage. Essentially via FSP we have expanded the design space for fatigue properties of cast alloys into the zone of wrought alloys. This has significant ramifications for localized strengthening of cast components.

Article III: Composite Fabrication in Cast Al A206 via Friction Stir Processing (Submitted to Scripta Metallurgica)

FSP has emerged as an advanced post-processing technique to produce surface or localized composites and synthesize second phases into the Al matrix in the solid state. The feasibility of applying this technique in fabricating localized composites was investigated. Different kinds and conditions of reinforcement materials were used: nano-sized Ta powders, nano-sized SiC powders, and discontinuously SiC reinforced aluminum. The composites produced at all tested conditions were characterized and evaluated, demonstrating the successes of this technique.

In the composite fabricated using nano Ta particles the particles were distributed uniformly. This uniform distribution is attributed to (i) sufficient material movement, (ii) encapsulation of reinforcement, and (iii) enough contact between the reinforcement and the tool. The study also showed that dispersion of the powders could be further improved by multi-pass FSP.

When fabricating composites with SiC particles, the effects of the amount of powder addition on the particle distribution and property (hardness) were studied. In the fabrication, the SiC powder was packed in a machined slot. The composite produced with the slot fully filled with SiC powder had a much better particle dispersion than that made with the slot half filled. The former was also harder than the latter. The composites produced with the slot either fully or half filled were harder than the alloy that was only FSPed.

This study found that in fabricating composites using DRA the particle dispersion was affected by the location of the DRA material and the number of stirring passes. Since DRA was a solid composite, the Si/SiC particles were well bonded with the Al matrix and more difficult to be moved by friction stirring than the SiC powders. To make a good Al/DRA composite region, the location where the DRA bar is embedded is critical. The

particle dispersion can also be improved by multi-pass friction stirring. The composite made with DRA was harder than that made with the SiC particle. Because using DRA can incorporate more reinforcement particles in the Al alloy matrix than can be achieved using other methods. In addition, we have observed that the grain size in the Al/DRA composite is much finer than in the material that has only been processed by FSP. The finer grains were attributed to the pinning effect of particles.

Chapter I: Microstructure Evolution via Friction Stir Processing in Al A206 Alloy

Abstract: Friction stir processing (FSP) is an outgrowth of Friction stir welding (FSW) that locally manipulates the microstructure by imparting a high level of energy in the solid state resulting in improved mechanical properties. FSP provides localized dramatic microstructure modification and grain refinement and significantly improves the properties in the processed region. In this study, alloy A206, a high-strength commonly used cast aluminum alloy, was subjected to FSP to locally manipulate the microstructure and achieve grain refinement and eliminate the heterogeneities, such as porosity as well as coarse phases, within the castings. The mechanism leading to such microstructural modifications in A206 alloy has been studied and is presented and discussed.

Introduction

Friction stir processing (FSP) is an emerging solid-state metal processing technique. Through FSP localized and significant microstructure modification and grain refinement is attained with concomitant mechanical property improvements in the processed region. One of its unique and attractive features is that it can be incorporated in the overall manufacturing cycle (post casting), and can be used to modify the properties locally and render different properties to different regions in the same component. The application of FSP has particular appeal in locally refining casting heterogeneities [1-5].

FSP was developed from friction stir welding (FSW) [6], a process that joins two pieces of metal by mechanically stirring them at the place of the join, transforming the metal into a softened state, and connecting them through mechanical mixing, diffusion, and recrystallization under an applied load. FSP is similar in concept, except that it is applied onto one piece of metal. Fig. 1 illustrates the FSP process; tool (rod) has a flat shoulder and the cone-shaped probe attached below has threads on the lateral surface. During operation, the machine first forces the high-speed rotating rod to penetrate into the fixed work piece. Once the tool shoulder fully makes contact, it moves across the work piece. The tool is non-consumable and when it rotates and traverses in the work piece it generates a large amount of heat from the friction between tool and work piece. When the temperature is ~ $0.7T_{mp}$, the matrix around the tool softens and will undergo significant deformation. The affected area is highly deformed and is in an unstable state; and has stored energy from friction stirring. The stored energy is the driving force for the dynamic recrystallization, leading to grain microstructure refinement [7-12].

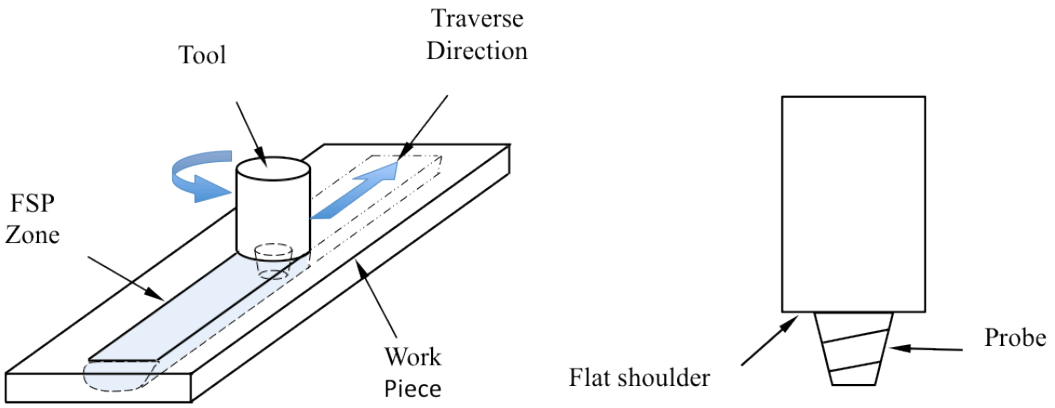

Figure 1: Schematic diagram of FSP set-up and the rotating tool.

Soon after its invention, FSP emerged as an important processing tool, and is now an important tool in refining the grains of metallic components, leading to ultra-fine grains (nano-sized level) [13-15]. Studies conducted to date have mostly been carried out on Al alloys such as 2XXX and 7XXX series alloys for the aerospace industry [16-18]. Most of the work to date has focused on wrought alloys, and not much work has been done in cast Al alloys. A major project was initiated at the Advanced Casting Research Center (ACRC) with several goals: to advance the study of FSP for casting alloys; to identify its specific features, and to understand the mechanism leading to microstructural evolution.

Generally, the optical microscope and SEM are common tools used for microstructural analysis. However, these tools are not sufficient to study microstructure evolution arising due to FSP. Transmission electron microscope (TEM) and electron backscatter diffraction (EBSD) techniques were utilized in this study. TEM can reveal sub-grain structure, dislocations, and grain boundary morphology that takes place during dynamic recrystallization [19-21]. TEM also allows one to study particle precipitation and dispersion,, and the interaction of precipitates with grains and dislocations; such understanding is essential for establishing the mechanism of recrystallization and precipitation evolution during FSP or post-FSP heat treatments [22, 23]. EBSD enables at a high level of statistical detail the study of grain boundary characteristics, grain orientations distribution, as well as texture evolution during FSP at specific areas of interest [24-30]. The micro-texture (grain orientation) distribution provides the information to deduce material flow during FSP.

This study was performed on alloy A206, which is a commonly used cast aluminum alloy with high-strength and widespread applications. The microstructure of the A206 alloy via FSP was locally manipulated to achieve grain refinement and eliminate the heterogeneities, such as porosity as well as coarse phases, within the castings. Detailed microstructural analyses were carried out to study the effects of FSP on the resultant microstructures, and to establish the operating mechanism.

Experimentation

The apparatus for FSP consists of the main FSP platform (machine table), the fixture, and instruments (thermocouple and dynamometer) used to detect and record the temperature distribution and the load profile during processing. The main platform for FSP is a HAAS CNC machine to which a specifically designed tool has been attached. The diameter of the tool shoulder is 16 mm, and at the end of the shoulder there is a tapered probe whose length is 3.2 mm. A tilt angle of three degrees (angle between machine spindle and work piece normal) has been applied to induce forging action at the trailing edge of the shoulder. This is achieved by inserting a back plate whose surface is machined into a slant surface. Proper tool penetration depth is very important in generating enough friction heat between the tool and the work piece and producing good FSP finish on the work piece. The minimum tool penetration depth requires the shoulder of the tool to have enough contact with the work piece, and this number is calculated based on the real contact condition between the tool and the material.

A commercially sand-cast A206 plate was used as the work piece. The alloy composition was Al-4.33Cu-0.077Si-0.046Fe-0.256Mg-0.343Mn and was supplied by Eck Industries. Dimensions of the work piece were 15 (L) x 7.5 (W) x 0.6 (T) cm. Processing parameters used were: tool rotation speed - 1000 RPM; tool traverse speed - 50.8 mm/min; and tool penetration depth - 4mm. The length of the FSP region was 12.7 cm. The local temperature of the work piece was monitored with K-type thermocouples and the data were recorded via FLIR S40 system. Four equi-distant holes were manufactured along the FSP traverse direction to accommodate four thermocouples, and the distance between each thermocouple was 2.54 cm. These thermocouples were inserted into the work piece at 2 mm below the top surface, and the tip of each thermocouple was near the centerline of the FSP nugget. Fig. 2 shows the workpiece and the location of the thermocouples.

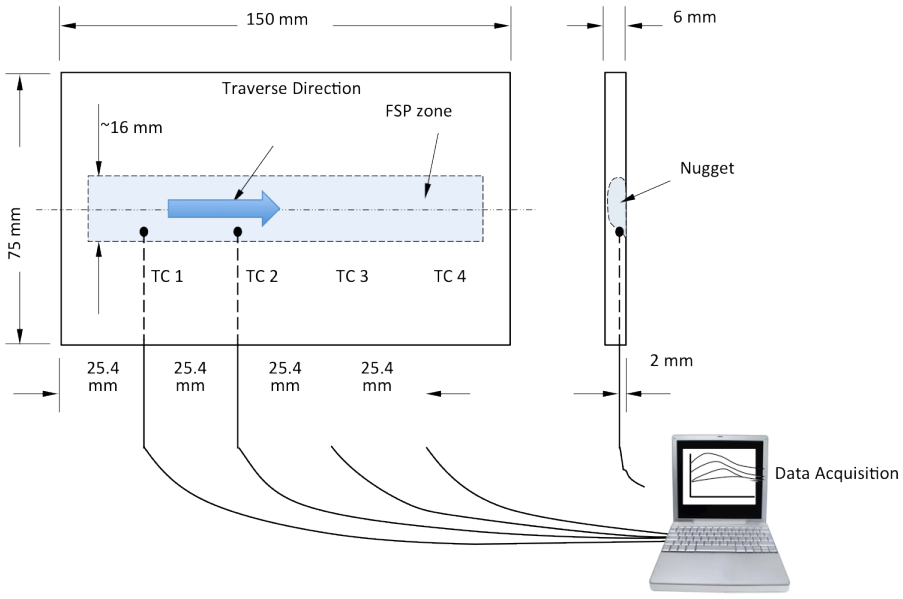

Figure 2: Schematic diagram showing workpiece with inserted thermocouples.

Samples for metallographic analysis were sectioned perpendicular to the FSP traverse direction and prepared for microstructural analysis. Barker's etchant and polarized light were used to reveal grain morphology. Thin films for TEM analysis were prepared via focus ion beam (FIB) technique at selected locations in the processed region. TEM work was carried out with a JOEL 2000 microscope operated at 200 kV. Specimen preparation for the EBSD analysis was carefully performed in order to properly image the structure and obtain high-quality diffraction patterns. A Carl Zeiss SUPRA-55 SEM equipped with the EBSD detector was used for EBSD data acquisition. The step size chosen for the FSPed specimen was 0.5 μm, and for the as-cast specimen was 5 μm.

Results and Discussion

Fig. 3 shows thermal profiles at four locations during FSP illustrating temperature change as a function of time. Each curve covers a similar area in the plot, signifying that the thermal history in the processing direction was quite steady [31]. The 0 second point denotes the time when the tool begins to contact the work piece, and the penetration process lasted about 20 seconds. The temperature begins to rise once the tool penetrated the work piece, and the peak value was observed when the tool moved right above the thermocouple. Peak values measured by four thermocouples were 338^0C, 363^0C, 405^0C and 422^0C, respectively. One should note that since the thermocouple cannot reach the tip of the tool during FSP, the actual local temperature of the material is higher than the measured values by about 30^0C.

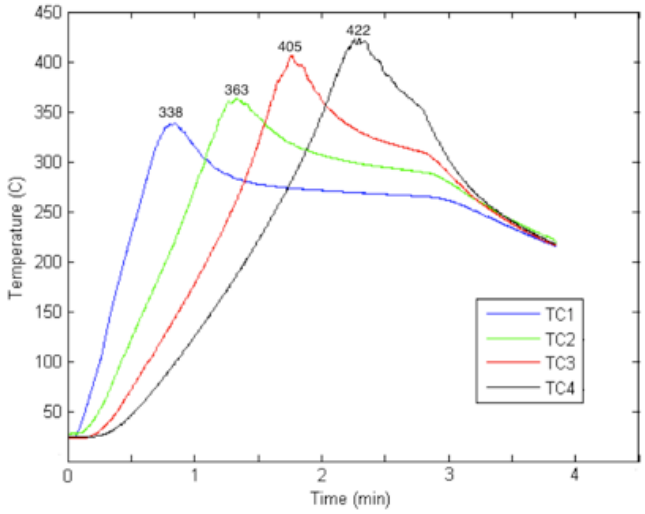

Figure 3: Localized thermal profiles at four different locations within the workpiece.

Fig. 4 shows optical micrographs of the as-cast sample. The microstructure of the as-cast A206 contained second phases that were mainly coarse needle-like $CuAl_2$-CuAl compounds (Fig. 4a). The average grain size is about 400 μm, and the dendritic microstructure is clearly delineated in Fig. 4b. Significant porosity was observed; pores up to 200-300 μm in length. Fig. 5 shows macrographs and micrographs taken from the FSPed sample. The FSP region has a basin-shaped nugget with a wide top; the left side of the FSP region is not symmetrical with the right side. In Fig. 5a, "A" refers to the

advancing side, on which the tool rotation direction is the same as the tool traverse direction; "R" refers to the retreating side of the work piece, where the tool rotation direction and tool traverse direction are opposite to each other. The advancing side (A) is on the right side of the nugget, and it is characterized by a steep boundary, whereas the retreating side (R) has a curved boundary. The boundaries are evidence of the asymmetric strain distribution experienced by the material during processing [14]. From Fig. 5b one can see that large amounts of fine second phase particles resulting from the breaking effect of the tool during FSP were uniformly distributed in the processed zone; moreover, porosity was nearly eliminated. Grain boundaries and grain size are clearly depicted in Fig. 5c. After FSP, grains are equiaxed and their size decreased to ~10 μm, a reduction of more than one order of magnitude compared with the original grain size. Fig. 5d and Fig. 5e show microstructures of the transition zones (retreating and advancing sides) between the FSP region and the matrix material. The boundary between the FSP region and the original starting dendritic structure is quite evident. In transition areas, grains are elongated and bent, and seem to deform along the shape of the nugget. Moreover, grains deformed more intensely and severely on the advancing side than on the retreating side.

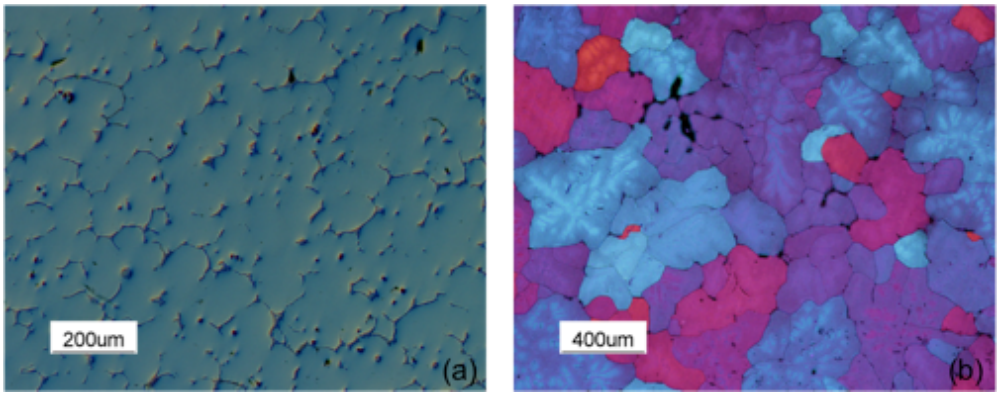

Figure 4: Micrographs showing (a) second phase distribution in the as-cast A206; (b) grain morphology of as-cast A206.

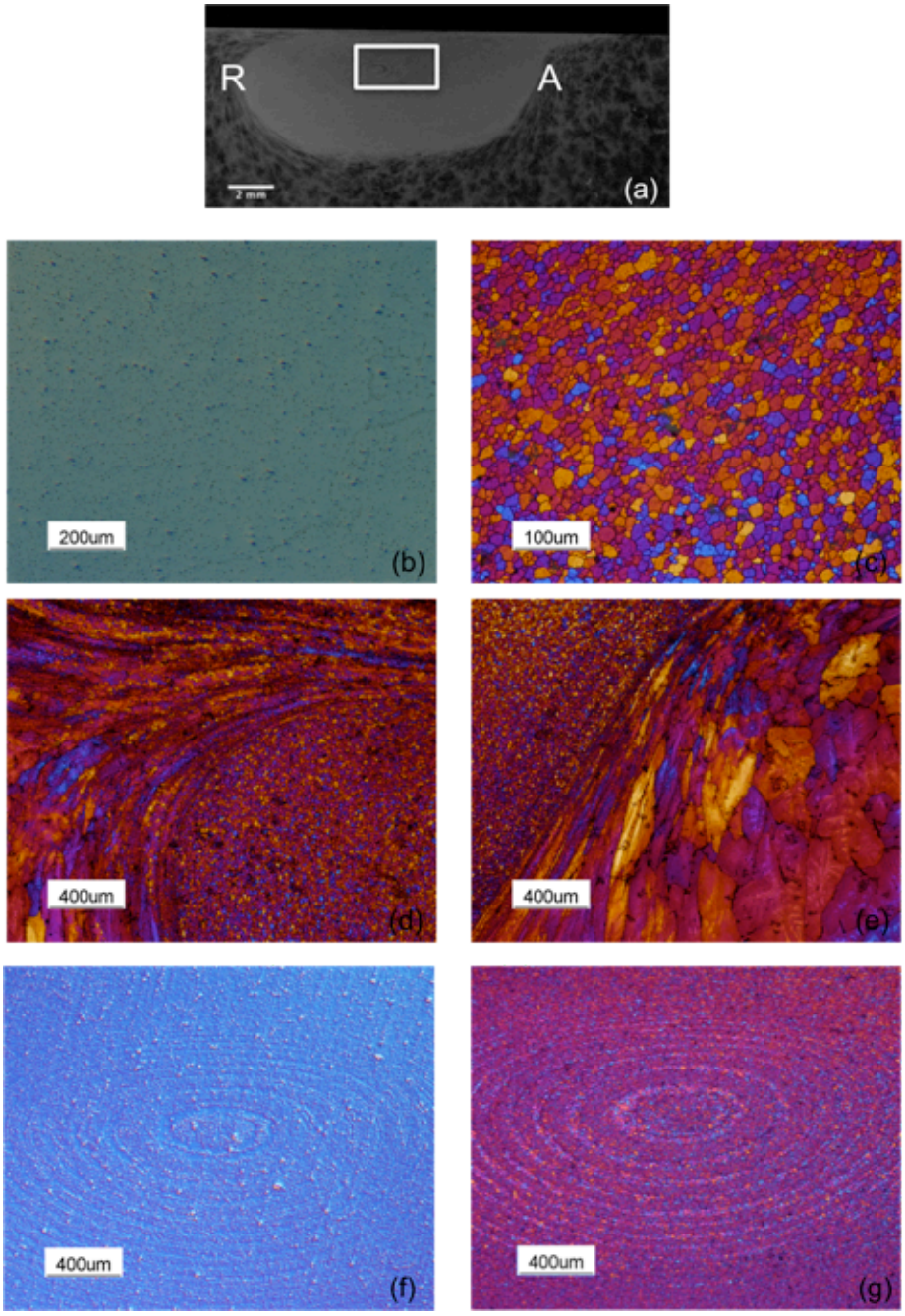

Figure 5: Macro and micro images of FSP region (a) macrograph of FSP region; (b) second phase distribution of FSPed A206; (c) grain morphology of FSPed A206; (d) micrograph of retreating side; (e) micrograph of advancing side; (f) micrograph of the onion ring; (g) grain orientations inside the onion ring region.

The FSP region contains a special microstructure feature, “the onion ring” structure, which is also called the banded structure [32-34]. The onion ring structure is marked with a white rectangular shape in Fig. 5a. From the transverse cross-section view (Fig. 5f), we can see that the onion rings consist of concentric, elliptical rings located in the middle of

the FSP nugget. The banded structure can also be observed in the top cross-section, and the space between each ring corresponds to the advance per revolution of the tool [34]. Previous studies reported that the appearance of onion rings was due to a periodic particle density variation or grain size variation [35]. However, as shown in Figs. 5f and 5g one cannot observe variations of grain size or particle density in the onion ring region. Polarized light was used to reveal grain morphologies; different colors indicating different grain orientations. As shown in Fig. 5g, within each ring there are many grains that show the same orientation (shown in light blue color). This result is supported by a number of researchers [28, 29, 36-38] indicating that there exists a texture or grain orientation component to the onion ring structure.

Grain size varies from the top to the bottom of the FSP nugget (Fig. 6). The finest grains were observed in the top layer of the FSP region, where the shoulder directly contacted the work piece. The average grain size in this region was about 5 μm. Grains are coarser in the middle of the nugget, and the average grain size is in the range of 10 μm. Some finer grains were observed in the bottom region of the nugget, and the grain size in this region is comparable to that in the top layer. This significant grain size variation along the vertical direction of the FSP region is due to the variable strain rate and temperature from the top to the bottom.

Grain boundary characteristics were analyzed via EBSD. Fig. 7a and Fig. 7c are image quality (IQ) maps taken from the as-cast A206 and FSPed A206 samples. The IQ map is overlaid with grain boundary angles. The “high angle” boundaries are defined as boundaries with misorientations exceeding 15 degrees, whereas the “low angle” boundaries are defined as boundaries with misorientations between 1 degree and 15 degrees. High-angle grain boundaries (HAB) are marked in blue color. When quantitatively analyzing the grain boundary character, for instance, calculating the fraction of high-angle boundaries, the minimum boundary misorientation must be defined. In this case, the minimum boundary misorientation was set to one. Fig. 7b and Fig. 7d are histograms showing the frequency distribution of grain boundary misorientation angles in the as-cast and FSPed specimen. The fraction of high angle grain boundaries increased from 26.6 % to 76.7% after FSP.

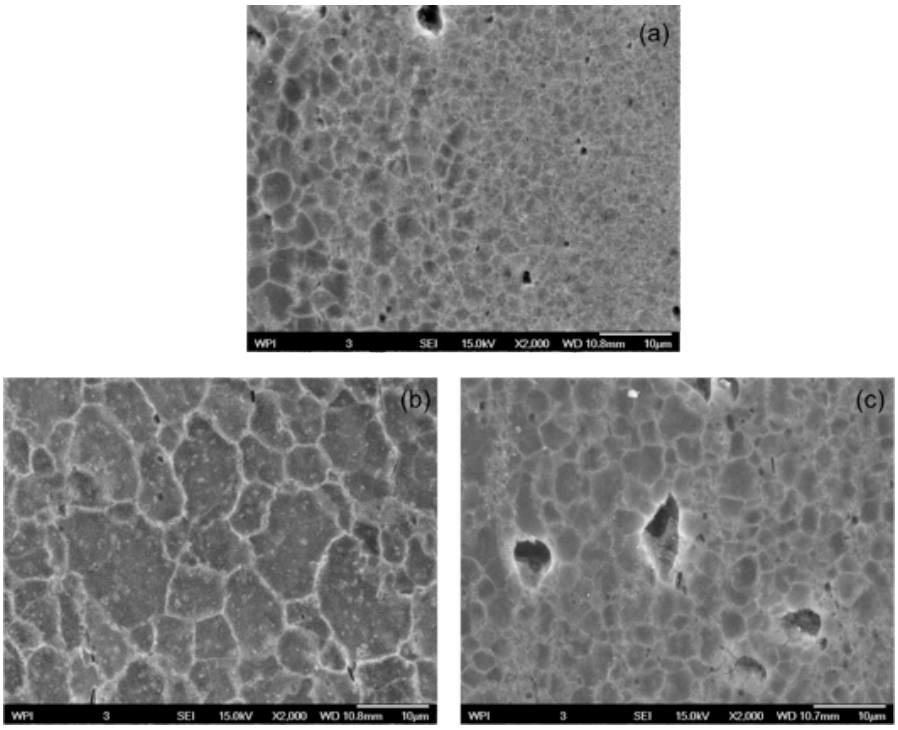

Figure 6: SEM micrographs showing grain size from the top to the bottom of the FSP nugget: (a) top layer; (b) middle region; (c) bottom layer.

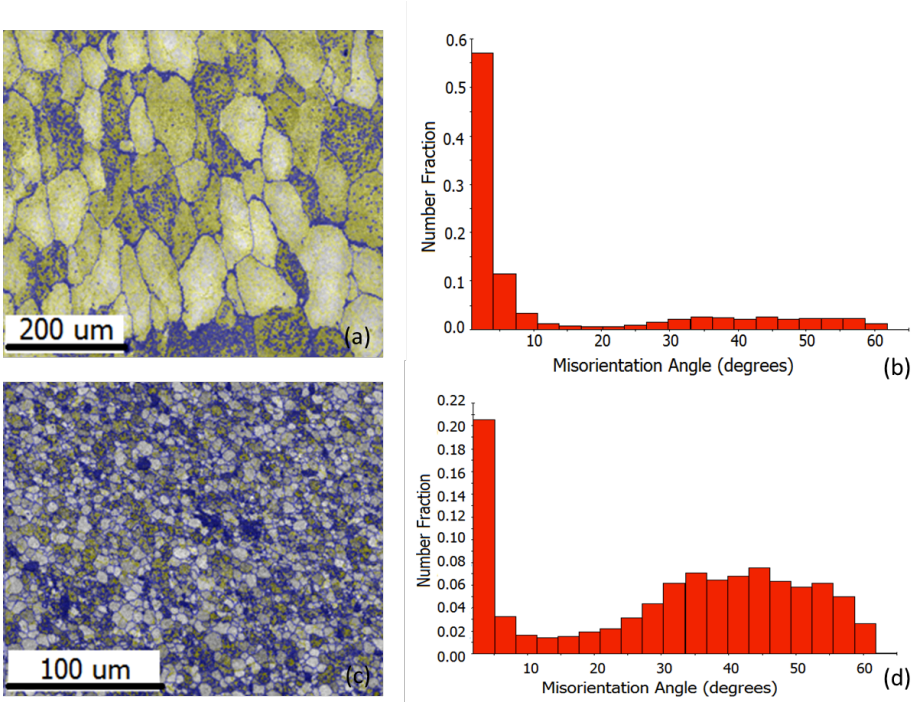

Figure 7: Image quality maps overlaid with low angle and high angle boundaries and misorientation angle distribution histogram plots of the as-cast A206 in (a) and (b); and FSPed A206 in (c) and (d).

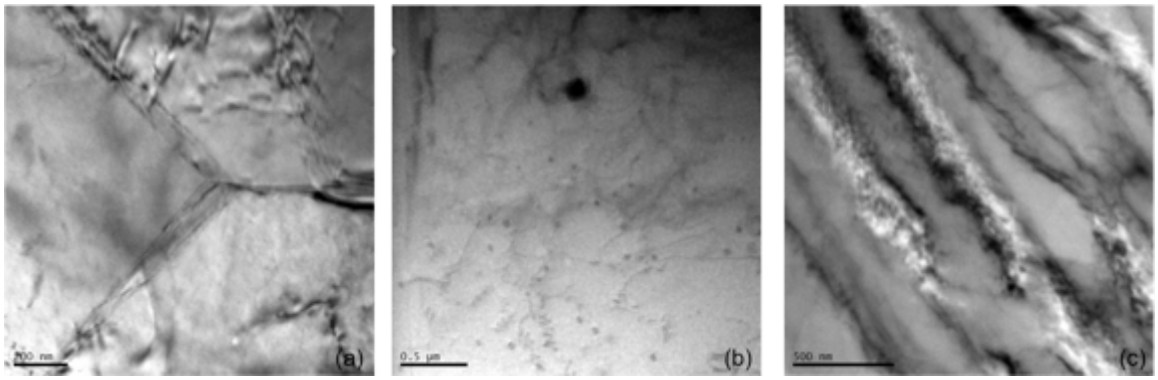

Figure 8: TEM micrographs showing the DRX microstructure: (a) clear grain boundaries of the recrystallized grains; (b) dislocation loops in the grain interior; (c) subgrains with lamellar boundaries.

Several research groups have studied the mechanism leading to microstructure evolution in the FSP nugget, i.e. grain refinement and large fraction of HABs [7-12, 28, 39, 40]; however, there is disagreement as to how microstructural features are developed during FSP. Four possible mechanisms have been put forward: (i) dynamic recovery; (ii) continuous dynamic recrystallization (CDRX), (iii) discontinuous dynamic recrystallization (DDRX), and (iv) geometric dynamic recrystallization (GDR). Recrystallization is the formation and migration of high angle grain boundaries; the driving force is the stored energy of deformation [41]. The essential difference between recovery and recrystallization is whether the stored energy is released with the movement of high angle boundaries [41].

FSP introduces a large number of dislocations in the work piece. The rearrangement or elimination of these dislocations reduces the internal energy of the system; this is the thermodynamic driving force for dynamic recovery. During dynamic recovery, subgrains or cell structures are formed by dislocation rearrangement and accumulation, and these substructures are revealed by TEM. Moreover, because there is no migration of high angle boundaries, most subgrains are formed with low angle boundaries. Contrary to dynamic recovery, there is large scale high-angle grain boundary migration during dynamic recrystallization. If grain refinement is caused via dynamic recrystallization, boundaries of the refined grains can be clearly delineated by both optical microscopy and TEM. From these results, it can be concluded that grain refinement via FSP is mainly due to dynamic recrystallization. To further confirm this conclusion, we note clear grain boundaries (Fig. 5 c and Fig. 8 a) as well as a high fraction of high angle boundaries. However, as shown in Fig. 8 b, some dislocation tangles and cell structures remain in the interior of refined grains, which indicates that dynamic recovery also took place during FSP. Although dynamic recovery occurs during FSP, it cannot be the dominant mechanism.

As noted above, the mainstream conclusion is that grain refinement during FSP is caused by dynamic recrystallization; however, there is no consensus among researchers whether recrystallization is continuous or discontinuous during FSP. Rhodes et al [10] and Su et

al. [11] have proposed the DDRX mechanism. Several others have concluded that grain refinement mechanism is by CDRX [7-9, 28, 39]. DDRX is operated by the formation and growth of a nucleus, and requires large-scale high angle boundary migration [40]. The data in this work suggests that grain refinement during FSP is due to CDRX. The high stacking fault energy of aluminium and high processing temperature during FSP make CDRX favourable over DDRX [40, 43]. The misorientation distribution (shown in Figs. 7b and 7d) indicates that although the number of high angle boundaries increased after FSP, the peak number frequency is located in the low-angle regime. The progressive transfer of the low angle boundaries to high angle boundaries developed a large fraction of HABs, which is the distinctive feature of CDRX.

In CDRX, a subgrain embryo that is capable of transitioning to a grain must have a high misorientation angle with respect to the adjacent deformed material [41]. There are several mechanisms that permit the subgrain to achieve a high misorientation angle. Su et al have proposed that the absorption of dislocations into subgrain boundaries is the dominant mechanism [8]. Drury has observed the lattice rotation at elevated temperatures in some aluminum alloys containing high solute levels [44]. In addition to these two mechanisms, this work shows that high misorientation angle can also be achieved via grain subdivision under high strain rates. Due to the extremely high strain levels reached in the FSP nugget, dislocation cells become flat and are sandwiched by lamellar dislocation boundaries [41]. These cell blocks are one to two cells wide and several cells in length (See Fig. 8c). The lamellar dislocation boundary is one type of the geometrically necessary boundaries (GNBs) [42], which can increase their misorientation angle and decrease their spacing at a much higher rate than other the cell boundaries [41].

The temperature and strain rate of the deformed material are two critical factors that affect dynamic recrystallization during FSP. These factors can be represented by the Zenner-Hollomon parameter, which has been shown to have significant influence on the recrystallized grain size [45]. The Zenner-Hollomon parameter is expressed as:

$$Z = \dot{\boldsymbol{\varepsilon}} \exp (Q/RT) \quad (1)$$

in which $\dot{\boldsymbol{\varepsilon}}$ and T denote the strain rate and temperature of the material. Q is the related activation energy of the material and R is the gas constant. The relation between the recrystallized grain size and the parameter Z can be expressed as:

$$\text{Ln } D = A - B \text{ X Ln } Z \quad (2)$$

where A and B are constants. When combining equations (1) and (2), one can see that the larger grain size results from a higher temperature or a lower strain rate. The main heat source in FSP is the tool shoulder [31]; generally, along the vertical direction within the FSP nugget, the temperature decreases from top to bottom. In addition to the temperature gradient, a strain rate gradient also exists in the FSP nugget. The strain rate is proportional to the ratio of the effective radius to the effective depth of the dynamic recrystallization zone [45]. As shown in Fig. 6a, the shape of the FSP nugget is an asymmetric eclipse. The strain rate had the highest value in the top layer, where the tool shoulder directly deformed the material. Although the temperature is higher in the top

layer, the extremely high strain rate had more of an impact on the parameter Z, which resulted in the smaller grain size compared with the grain size in the middle of the FSP nugget (see Fig. 6a). The grain size in the bottom of the FSP nugget is also smaller than the grain size in the middle of the FSP nugget, which indicates that the lower temperature has a large effect on Z. It is worth noting that there is a time lapse after the FSP tool traverses the material and the deformed material cools down; static recrystallization, recovery, and grain growth can occur at such temperatures during this interval. The grain structures that are observed in Fig. 6 are the final coarsened microstructure. However, the trend of the grain size distribution at different locations within the FSP region still follows the relation given by equation (2). Static recrystallization, recovery, and grain growth can be suppressed by the so-called "stop-action" technique, which was developed by Colligan [46] and popularized by Prangnell and Heason [12] to capture the localized in situ material flow and recrystallized microstructure during FSP. This technique entails emergency stopping of the machine and immediate quenching of the final tool position; by doing so, the microstructure during FSP can be frozen and preserved.

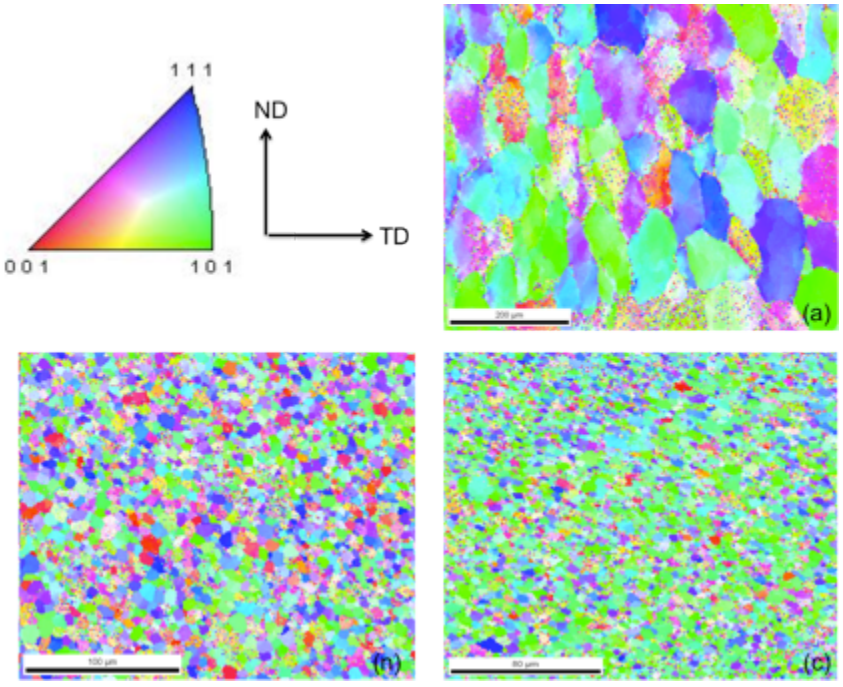

Figure 9: Inverse pole figure (IPF) of (a) as-cast A206; (b) FSP nugget; (c) FSP nugget within the onion ring. Different colors in the IPFs represent different crystallographic axes parallel to the FSP traverse direction.

The inverse pole figures (IPF) taken from the as-cast and FSPed samples are shown in Fig. 9. The reference frame is the crystal axis that is parallel to the FSP traverse direction. Different colors shown in the IPF represent various crystallographic directions. As shown in Fig. 9a, the cast microstructure has a homogeneous grain orientation distribution. FSP produces a random texture in most of the nugget region in the ND-TD plane (Fig. b). However, within one onion ring circle a high fraction of <110> crystallographic

orientation was observed (Fig 9 c). Grains located between two onion rings have random orientations. The crystallographic orientation alternating between the strong <110> and the random crystallographic orientation causes the appearance of the onion ring pattern. The "onion ring" structure corresponds to the periodicity of the layer being deposited behind the tool, and which is equal to the tool traverse per revolution [34]. The alternating texture is due to the variable strain experienced by the material [47]. The ideal simple-shear orientation of FCC metals as they appear in the {111}pole figure are shown in Fig. 10 [48]. It has been shown that in 2195 Al alloy weldments (produced by friction stir welding) in one cycle of the tool revolution, B/ $\overline{B}$ components of the simple shear texture always existed no matter how large the strain was, whereas the C components varied from zero to an extent that was comparable to B/ $\overline{B}$ following the variation of the strain [47]. The alternation between the B/ $\overline{B}$ components and B/ $\overline{B}$ + C components gives rise to the onion ring structure. However, the B/ $\overline{B}$ and C components are stable under high strains. Applying a higher tool rotation speed during FSP can eliminate the onion ring pattern, because a larger strain is achieved when increasing the tool rotation speed. The {111} pole figures of the as-cast A206 and the FSPed A206 are shown in Fig. 11. The as-cast specimen has a random texture, whereas the FSP nugget is dominated by a rotated cube texture, which is the typical texture of the material after recrystallization [25]. It is noteworthy that the textural peaks in the pole figure shown in Fig. 11b are slightly deviated from the ideal position, and this may be caused by the tool-tilting angle or the taper angle of the tool probe applied during FSP. The B/ $\overline{B}$ + C components of the simple shear texture were only found at a few locations within the onion ring region, which indicates that the simple shear texture transferred into the nearly {100}<100> cube texture via static recrystallization during the cooling stage of FSP.

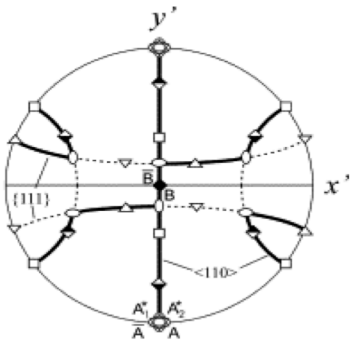

A_1^* △ A_2^* ▽ A ○ $\overline{A}$ 0 B ◆ $\overline{B}$ ◆ C □

Notation	{h k l} <u v w>	Euler angles (°) [a]		
		ϕ_1	ϕ	ϕ_2
A_1^*	$(111)[\bar{1}\bar{1}2]$	35.26/215.26	45	0/90
		125.26	90	45
A_2^*	$(111)[1\,1\,\bar{2}]$	144.74	45	0/90
		54.74/234.74	90	45
A	$(1\bar{1}1)[1\,1\,0]$	0	36.25	45
$\overline{A}$	$(\bar{1}\,1\,\bar{1})[\bar{1}\bar{1}0]$	180	36.25	45
B	$(1\bar{1}\bar{2})[1\,1\,0]$	0/120/240	54.74	45
$\overline{B}$	$(\bar{1}\,1\,\bar{2})[\bar{1}\bar{1}0]$	60/180	54.74	45
C	{001}<110>	90/270	45	0/90
		0/180	90	45

a: Given in the φ_2 =0°, 45°and 90° sections with φ_1 = 0-270° only

Figure 10: Ideal orientation of FCC metals under simple shear as they appear in the {111} pole figure [48].

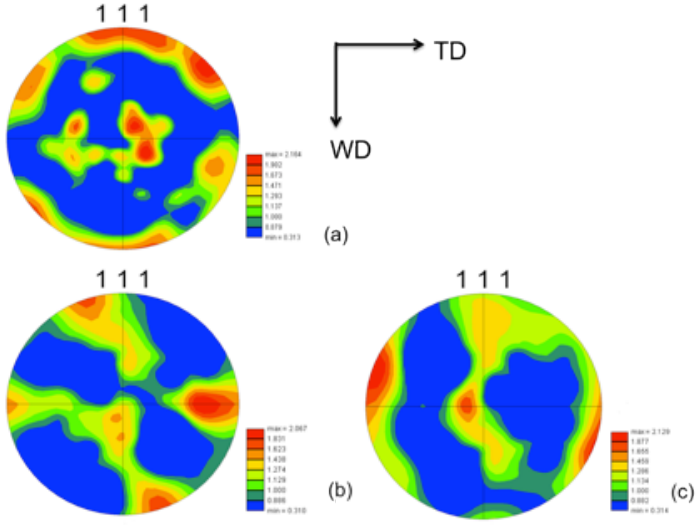

Figure 11: {111} pole figures of the (a) as-cast A206; (b) FSP nugget; (c) FSP nugget within one circle of onion ring structure.

Summary

FSP was applied to locally manipulate cast aluminum alloy A206 microstructure. In doing so, porosity is eliminated and the dendritic microstructure transformed. Second phase particles are distributed uniformly in the aluminum matrix after FSP, and the size and aspect ratio of these particles decreased significantly. The FSP nugget contained fine equiaxed grains with high-angle boundaries.

The dominant mechanism leading to grain refinement is continuous dynamic recrystallization. High misorientation angles were achieved via subgrain rotation, lattice rotation, and high-strain deformation-induced grain subdivision. The temperature and strain rate of the deformed material were two important factors that influenced the recrystallized grain structure. Refined grains with different diameters were observed along the vertical direction of the FSP nugget due to various temperature and strain rate conditions.

The appearance of the onion ring pattern is due to a periodic texture variation. The EBSD map shows an alternating existence of the strong <110> orientation and random crystallographic orientations. The as-cast A206 specimen had a random texture on the {111} pole figure, whereas the FSP nugget was dominated by a rotated cube texture, which was the typical texture of the recrystallized material. At a few locations within the onion ring, the {111} pole figure has the B/ $\overline{B}$ + C components of simple shear texture.

References

[1] Z.Y. Ma, S.R. Sharma, R.S. Mishra, and M.W. Mahoney, "Microstructural Modification of Cast Aluminum Alloys Via Friction Stir Processing," Materials Science Forum, vol. 426-432, pp. 2891-2896. (2003)

[2] Z.Y. Ma, S.R. Sharma and R.S. Mishra, "Microstructural Modification of as-Cast Al-Si-mg Alloy by Friction Stir Processing," Metallurgical and Materials Transactions A, Vol. 37, pp. 3323-3386. (2006)

[3] M.L. Santella, T. Engstrom and D. Storjohann, "Effects of Friction Stir Processing on Mechanical Properties of the Cast Aluminum Alloys A319 and A356," Scripta Materialia, Vol. 53, pp. 201-206. (2005)

[4] Z.Y. Ma, A.L. Pilchak, M.C. Juhas and J.C. Williams, "Microstructural Refinement and Property Enhancement of Cast Light Alloys Via Friction Stir Processing," Scripta Materialia, Vol. 58, pp. 361-366. (2008)

[5] D. Zhang, M. Suzuki and K. Maruyama, "Microstructural Evolution of a Heat-Resistant Magnesium Alloy due to Friction Stir Welding," Scripta Materialia, Vol. 52, pp. 899-903. (2005)

[6] W.M. Thomas, E.D. Nicholas, J.C. Needham, M.G. Murch, P. Templesmith, C.J. Dawes, 1991, (G.B. Patent Application No. 9125978.8).

[7] K.V. Jata and S.L. Semiatin, "Continuous dynamic recrystallization during friction stir welding of high strength aluminum alloys", Scripta Materialia, Vol. 43, pp. 743-749. (2000)

[8] J.-Q Su, T.W Nelson and R Mishra, M Mahoney, "Microstructural investigation of friction stir welded 7075-T651 aluminum", Acta Materialia, Vol. 51, pp. 713-729. (2003)

[9] M. Karlsen, Ø. Frigaard, Jarle Hjelen, Øystein Grong and H. Norum, "SEM-EBSD Characterisation of the Deformation Microstructure in Friction Stir Welded 2024 T351 Aluminium Alloy", Materials Science Forum, Vol. 426-432, pp. 2861-2866. (2003)

[10] C.G. Rhodes, M.W. Mahoney, W.H. Bingel and M. Calabrese, "Fine-grain evolution in friction-stir processed 7075 aluminum", Scripta Materialia, Vol. 48, pp. 1451-1455. (2003)

[11] J.-Q. Su, T.W. Nelson, and C.J. Sterling, "Grain refinement of aluminum alloys by friction stir processing", Philosophical Magazine, Vol. 86, pp. 1-26. (2006)

[12] T.R. McNelley, S. Swwaminathan, J.-Q. Su, "Recrystallization mechanism during friction stir welding/processing of aluminum alloys", Scripta Materialia, Vol. 58, pp. 349-354

[13] Y.J. Kwon, N.Saito and I. Shigematsu, "Friction stir process as a new manufacturing technique of ultrafine grained aluminum alloy", Journal of Materials Science Letters, Vol. 21, pp. 1473-1476. (2002)

[14] D.C. Hofmann and K.S. Vecchio, "Submerged friction stir processing (SFSP): An improved method for creating ultra-fine-grained bulk materials", Materials Science and Engineering A, Vol. 234, pp. 234-241. (2005)

[15] Z.Y. Ma and R.S. Mishra, "Development of ultrafine-grained microstructure and low temperature (0.48 T_m) superplasiticity in friction stir processed Al-Mg-Zr", Scripta Materialia, Vol. 53, pp. 75-80. (2005)

[16] P. Cavaliere, and P.P. De Marco, "Friction stir processing of a Zr-modified 2014 alloy", Materials Science and Engineering A, Vol. 462, pp. 206-210. (2007)

[17] P. Cavaliere, and A. Squillace, "High temperature deformation of friction stir processed 7075 aluminium alloy", Materials Characterization, Vol. 55, pp. 136-142. (2005)

[18] P. Cavaliere, "Effects of friction stir processing on the fatigue properties of a Zr-modified 2014 alloy", Materials Characterization, Vol. 57, pp. 100-104. (2006)

[19] Z.Y. Ma, S.R. Sharma and R.S. Mishra, "Effect of friction stir processing on the microstructure of cast A356 aluminum", Materials Science and Engineering A, Vol. 433, pp. 269-278. (2006)

[20] A.P. Gerlicha and T. Shibayanagi, "Grain boundary sliding during friction stir spot welding of an aluminum alloy", Scripta Materialia, Vol. 60, pp. 236-239. (2009)

[21] A.H. Feng and Z.Y. Ma, "Microstructrual evolution of cast Mg-Al-Zn during friction stir processing and subsequent aging", Acta Materialia, Vol. 57, pp. 4248-4260. (2009)

[22] C.A.W. Olea, L. Roldo, J.F. dos Santos and T.R. Strohaecker, "A sub-structural analysis of friction stir welded joints in an AA6056 Al-alloy in T4 and T6 temper conditions", Materials Science and Engineering A, Vol. 454-455, pp. 52-62. (2007)

[23] H.J. Zhang, H.J. Liu and L. Yu, "Microstructure and mechanical properties as a function of rotation speed in underwater friction stir welded aluminum alloy joints", Materials and Design, Vol. 32, pp. 4402-4407. (2011)

[24] S. Mironow, Y.S. Sato and H. Kokawa, "Applications of EBSD to microstructural control in friction stir welding/processing", Chpater 21 of Electron backscatter diffraction in materials science, edited by Adam J. Schwartz, Mukul Kumar, Brent L. Adams and David P. Field (2009)

[25] U.F.H.R. Suhuddin, S. Mironow, Y.S. Sato and H. Kokawa, "Grain structure and texture evolution during friction stir welding of thin 6016 aluminum alloy sheets", Materials Science and Engineering A, Vol. 527, pp. 1962-1969. (2010)

[26] R. Kapoora, N. Kumara, R.S. Mishra, C.S. Huskampb and K.K. Sankaranb, "Influence of fraction of high angle boundaries on the mechanical behavior of an ultrafine grained Al–Mg alloy", Materials Science and Engineering A, Vol. 527, pp. 5246-5254. (2010)

[27] N. Kumar, R.S. Mishra, C.S. Huskamp and K.K. Sankaran, "Microstructure and mechanical behavior of friction stir processed ultrafine grained Al-Mg-Sc alloy", Vol. 528, pp. 5883-5887. (2011)

[28] P.B. Prangenell and C.P. Heason, "Grain structure formation during friction stir welding observed by the 'stop action technique'", Acta Materialia, Vol. 53, pp. 3179-3192. (2005)

[29] Y.S. Sato, H. Kokawa, K. Ikeda, M. Enomoto, S. Jogan and T. Hashimoto, "Microtexture in the friction-stir weld of an aluminum alloy", Metallurgical and Materials Transactions A, Vol. 32, pp. 941-948. (2001)

[30] M.M.Z. Ahmed, B.P. Wynne, W.M. Rainforth and P.L. Threadgill, "Microstructure, crystallographic texture and mechanical properties of friction stir welded AA2017A", Materials Characterization, Vol. 64, pp. 107-117. (2011)

[31] D.C. Hofmann and K.S. Vecchio, "Thermal history analysis of friction stir processed and submerged friction stir processed aluminum", Materials Science and Engineering A, Vol. 465, pp. 165-175. (2007)

[32] K.N. Krishnan, "On the formation of onion rings in friction stir welds", Materials Science and Engineering A, Vol. 327, pp. 246-251. (2002)

[33] G.R. Cui, Z.Y. Ma and S.X. Li, "Periodical plastic flow pattern in friction stir processed Al–Mg alloy", Scripta Materialia, Vol. 58, pp. 1082-1085. (2008)

[34] Z.W. Chen and S. Cui, "On the formation mechanism of banded structures in aluminum alloy friction stir welds", Scripta Materialia, Vol. 58, pp. 417-420. (2008)

[35] B. Yang, J. Yan, M.A. Sutton and A.P. Reynolds, "Banded microstructure in AA2024-T351 and AA2524-T351 aluminum friction stir welds: Part I. Metallurgical studies", Materials Science and Engineering A, Vol. 364, pp. 55-65. (2004)

[36] D.P. Field, T.W. nelson, Y. Hovanski and K.V. Jata, "Heterogeneity of crystallographic texture in friction stir welds of aluminum", Metallurgical and Materials Transcations A, Vol. 32, pp. 2869-2877. (2001)

[37] J.A. Schneider and A.C. Nunes, Jr. "Charaterization of plastic flow and resulting microstextures in a friction stir weld", Metallurgical and Materials Transcations B, Vol. 35, pp. 777-783. (2004)

[38] R.W. Fonda, J.F. Bingert and K.J. Colligan, "Development of grain structure during friction stir welding", Scripta Materialia, Vol. 51, pp.243-248. (2004)

[39] R.W. Fonda, K.E. Knipling and J.F. Bingert, "Microstructure evolution ahead of the tool in aluminum friction stir welds", Scripta Materialia, Vol. 58, pp. 343-348. (2008)

[40] J.-Qing Su, T.W. Nelson and C.J. Sterling, "Microstructure evolution during FSW/FSP of high strength aluminum alloys", Materials Science and Engineering A, Vol. 405, pp. 277-286. (2005)

[41] R.D. Doherty, D.A. Hughes, F.J. Humphreys, J.J. Jonas, D. Juul Jensen, M.E. Kassner, W.E. King, T.R. McNelley, H.J. McQueen and A.D. Rollett, "Current issues in recrystallization: a review", Materials Science and Engineering A, Vol. 238, pp. 219–274. (1997)

[42] D. Kuhlmann-Wilsdirf and N. Hansen, "Geometrically necessary, incidental and subgrain boundaries", Scripta Metallurgica et Materialia, Vol. 25, pp. 1557-1562. (1991)

[43] N. Kumar, R.S. Mishra, C.S. Huskamp and K.K. Sankaran, "Microstructure and mechanical behavior of friction stir processed ultrafine grained Al-Mg-Sc alloy", Materials Science and Engineering A, Vol. 528, pp. 5883-5887. (2011)

[44] M.R. Drury and F.J. Humphreys, "The development of microstructure in Al-5% Mg during high temperature deformation", Acta Metallurgica, Vol. 34, pp. 2259-2271. (1984)

[45] C.I. Chang, C.J. Lee and J.C. Huang, "Relationship between grain size and Zener–Holloman parameter during friction stir processing in AZ31 Mg alloys", Scripta Materialia, Vol. 51, pp. 509-514. (2004)

[46] K. Colligan, "Material Flow Behavior during Friction Stir Welding of Aluminum", Welding Journal, Vol. 78, pp.229-237. (1999)

[47] R.W. Fonda and J.F. Bingert, "Texture variations in an aluminum friction stir weld", Scripta Materialia, Vol. 57, pp.1052-1055. (2007)

[48] S. Li, I.J. Beyerlein and M.A.M. Bourke, "Texture formation during equal channel angular extrusion of fcc and bcc materials: comparison with simple shear", Materials Science and Engineering A, Vol. 394, pp. 66-77. (2005)

Chapter II: Localized Strengthening of Cast Al A206 Alloy via Friction Stir Processing

Abstract : Friction stir processing (FSP) is an outgrowth of friction stir welding (FSW) that locally manipulates the microstructure by imparting a high level of energy in the solid state resulting in improved mechanical properties. This study has shown that FSP can be implemented as a post-casting method to locally eliminate casting defects, such as porosity due to gas evolution during casting. Coarse second phases are broken into fine nearly equiaxed particles and distributed uniformly in the matrix; grain refinement is also attained by dynamic recrystallization during FSP. This results in improved hardness, tensile properties and fatigue properties of the cast Al A206 alloy. Such improvements have important implications for manufactured components for a variety of automotive and other industrial applications. The convenience of FSP as a post-processing step that can easily be carried out during machining operations makes it an attractive post casting technology. FSP opens up the design space for cast Al alloys into that of wrought alloys; both dynamic and static mechanical properties are significantly improved.

Introduction

Friction stir processing (FSP) was developed from the friction stir welding (FSW) process [1]. Friction stir welding is a solid-state metal joining process that joins two pieces of metal by mechanically stirring them at the place of the join, transforming the metal into a softened state, and connecting pieces through mechanical mixing, diffusion, and recrystallization under mechanical pressure. FSP is similar in concept in that the workpiece is mechanically stirred, however there is no joining involved. It works on a monolithic work piece and functions in modifying and controlling the microstructure in a localized region or near-surface layers and enhances the mechanical properties [2].

FSP has emerged as an important post-processing technique and has drawn much attention. It was first applied to highly alloyed wrought Al alloys such as the 2XXX and 7XXX series for aerospace applications; superplasticity, high strength, and fracture resistance of these alloys were attained via FSP [3-5]. A unique characteristic of FSP is the resultant ultrafine grain structure and simultaneous improvements in the strength and ductility of the processed alloy [6]. This phenomenon is contrary to the Hall-Patch relationship, wherein fine grains result in grain boundary strengthening [7] at the expense of ductility [8]. This implies that FSP has a different strengthening mechanism. Several factors can account for the property improvements observed in the FSPed region, such as, grain size and grain morphology, distribution and density of dislocations, and grain boundary morphology. Friction stir processed microstructures have the following features [9]: (i) equiaxed fine grains or ultra-fine grains (nano-sized level) [10-12], (ii) refinement of second phases, and (iii) large fraction of high-angle grain boundaries. These microstructural features enable superplastic deformation at high strain rates and/or low temperatures [13-15] as well as improved room-temperature formability [16].

The earliest application of FSP was to repair cracks/defects in Al based castings. Previously, defects in cast Al alloys were repaired using arc welding; however its nature of high temperature local melting and subsequent fast cooling resulted in other detrimental issues: oxidation, weak heat affected zone, deformation, and secondary cracks. Thus when FSP emerged as a solid state processing method, it was well received by the processing community. Many studies followed addressing various aspects of FSP; for example, Z.Y. Ma et al [17, 18] conducted a study of FSP on sand-cast A356 alloys. They studied the effects of process parameters and found that FSP broke up and dispersed the coarse acicular Si particles, resulting in a uniform distribution of Si particles in the aluminum matrix with significant microstructural refinement and reduction of cast defects. Such structural refinement resulted in mechanical property improvements, which was an added bonus. Though extensive studies of FSP in Al alloys were carried out [3-5], it was mostly applied to wrought alloys. A well-established process for cast components with a fundamental understanding of the mechanisms leading to such refinement has been lacking.

The stirring action of FSP deforms the workpiece vigorously and, therefore, the difference in alloy formability influences FSP functionality. The work on wrought alloys which have high formability may not apply to cast alloys. In this vein, this work was undertaken to establish the process-operating window for FSP in cast Al alloys; to establish the operative mechanism; and to create a database. We focused on A206 aluminum alloy - an important and widely used Al casting alloy because of its high strength and good machinability. The motive behind this study was to confirm and demonstrate FSP as an enabling technology for post-processing of cast Al alloys. Furthermore, FSP opens the space for cast structures to be locally manipulated to attain wrought material attributes, as well as to expand the design space especially for dynamic properties.

Experimentation

Starting Material, Set-up and Metallographic Preparation

Commercially sand-cast A206 plates made by Eck Industries were used for the work piece; alloy composition being Al-4.33Cu-0.077Si-0.046Fe-0.256Mg-0.343Mn. T4, T6, and T7 heat treatments were applied both before and after FSP. Processing details used are given below:

> T4: Raise temperature from 25 °C to 460 °C in 1 hour è continue to increase temperature to 480 °C in 1.5 hour è hold at 480 °C for 2 hours è raise to 518 °C in 0.5 hour è hold at 518 °C for 10 hours è quench in 65 °C water è hold for 5 days è mechanical testing.
>
> T6: Follow the T4 treatment plus artificial aging: After quenching, hold for 24 hours at room temperature èage 4 hours at 155 °C è cool to room temperature in still air.

T7: Follow the T4 treatment plus an over-artificial aging: After quenching, hold for 24 hours at room temperature èage 4 hours at 200 °C è cool to room temperature in still air.

Several different processing conditions were followed in this study; these were: (i) FSP was directly carried out on the surface of the as-cast work piece; this condition is termed AC+FSP; (ii) FSP was carried out on the work piece that had been heat treated prior to FSP; this condition is termed AC+HT+FSP, and the nomenclature for this condition is termed pre-FSP heat treatment; (iii) heat treatment was carried out after FSP; this condition is termed AC+FSP+HT, and the nomenclature for this condition is termed post-FSP heat treatment.

FSP was carried out on a HAAS M3 CNC machine at WPI. The tool used for FSP has a shoulder whose diameter is 16 mm with a screwed taper probe at its end. The length of the probe is 3.2mm. A tilt angle of three degrees was applied during processing to generate a forging action at the trailing edge of the tool. The two key processing parameters used were: tool rotation speed–1000 RPM, and tool traverse speed–50.8 mm/min.

Hardness, tensile properties, and fatigue properties were measured to evaluate the effects of FSP on the performance of the cast A206 alloy. The specimens for all the tests were sectioned from the FSP affected regions. Since different sizes of specimens were required for different tests, to provide sufficient sizes of FSP-affected regions for different specimens, work pieces of two thicknesses were processed. Specimens for the hardness and tensile tests were sectioned from the 6.26 mm-thick work piece, in which the depth of the FSP region was 5 mm. Specimens for the fatigue test were manufactured from the 16 mm-thick work piece, in which the depth of the FSP region was 15.4 mm.

Metallurgical studies were conducted using optical microscopy and SEM. For analyses using the optical microscope, samples were sectioned perpendicular to the FSP traverse direction. The samples were ground, polished, and analysed at both as-polished and electrochemically etched conditions. Barker's agent was used for etching to reveal the grain size inside the FSP region. The electron backscatter diffraction (EBSD) technique was used to quantify the misorientation angles across grain boundaries, and EBSD measurements were taken on a Supra 55 SEM system with a step size of 0.5 μm. Fractographic examination was conducted using a JOEL 7000 SEM, and EDS was used to identify different phases.

Property Tests

Hardness

The Knoop hardness (HK) test was conducted using the Buehler OmniMet MHT automatic microhardness test system with a load of 500 gf. As shown in Fig. 1, the test specimens were sectioned perpendicular to the FSP traverse direction to reveal the transverse cross-section. Measurements were taken on the transverse cross-section along

two different depths.: location 1 (L1) is ~ 300 μm below the top surface of the FSP region, and location 2 (L2) is at the middle line of the FSP region..

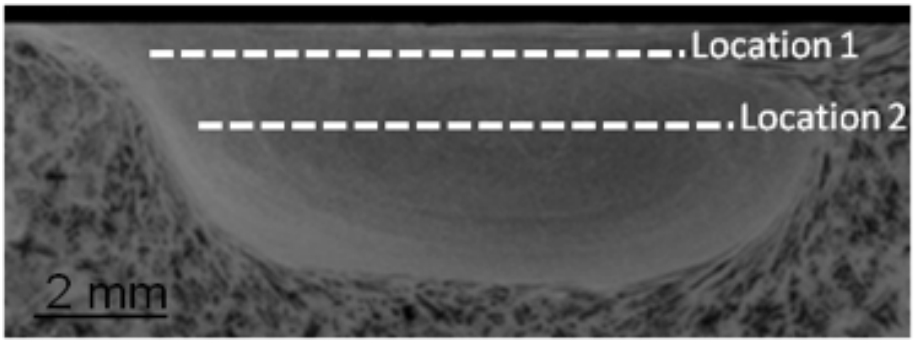

Figure 1: Macrograph of the FSPed region showing two locations where the microhardness data were collected.

Tensile Properties

Specimens for tensile testing were all taken from the FSP nugget region ensuring that the whole of the sample was processed. Each specimen was taken along the transverse direction of the FSP centerline as shown in Fig. 2. The specimen had a 25 mm gauge length with a cross section of 12.5 x 6.3 mm in accordance to ASTM B8. The test was conducted at room temperature using the Instron model 5500. The ramp rate was set at 1 mm/min (strain rate of 4%) and the strain was measured using an extensometer of 25 mm gauge length.

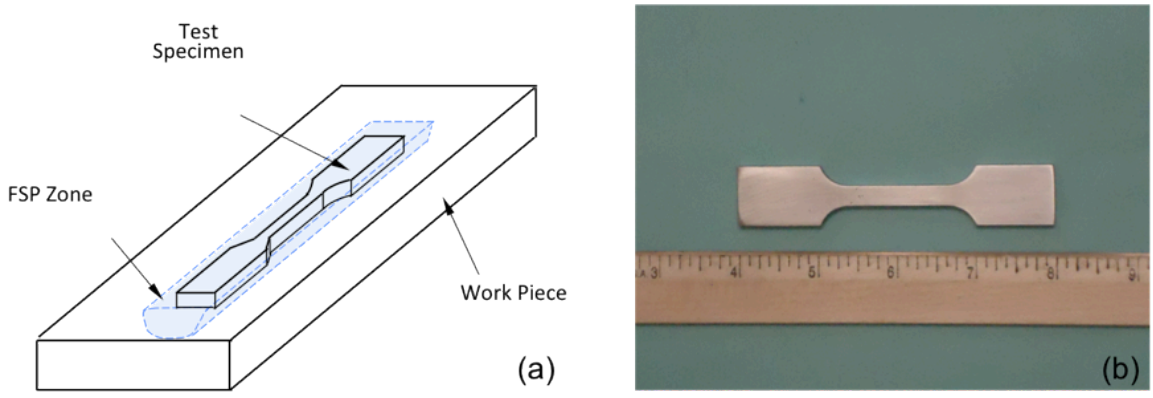

Figure 2: Specimen for the tensile test: (a) schematic diagram of the tensile bar; (b) image of the tensile bar.

Fatigue Properties

Ultrasonic fatigue tests were conducted at room temperature in the ambient air over a range of stresses using fully reversed load (R= -1). Figure 3 shows the ultrasonic fatigue test apparatus and the geometry of the ultrasonic fatigue test specimen. The specimens had a cylindrical gauge section, and were turned down from a rectangular bar; dimensions of the bar were 15 (L) x 1.4 (W) x 1.4 (H) cm. For the FSPed specimen, the gauge section was manufactured from the FSP nugget to ensure homogeneity of microstructure. In order to have a consistent surface finish with low residual stress, samples were polished along the longitudinal direction to reach a Ra 8 value; surface finishing was carried out by Westmoreland Materials Testing in Youngstown, PA.

The specimen was mounted on the ultrasonic fatigue test instrument by fixing only one end; the other end of the specimen could vibrate freely with the mechanical oscillation generated by the acoustic wave. The specimen vibrated in resonance at approximately 20 kHz. Fig. 4 shows the displacement and strain distributions along the specimen. The displacement has two maximum amplitudes at both ends of the specimen and a vibration node in the center of the specimen. The strain amplitude along the length of the specimen has a maximum value in the center, and the strain in the gauge length was held constant so that variation was controlled within 5% [19]. Within the gauge section the displacement was proportional to the strain [19]. Based on this relation, the control mode of the ultrasonic fatigue test could be converted from a displacement-controlled mode to a total-strain controlled mode, which eased the performance of the operation. Two strain gauges were used at the center of the gauge section to measure the strains coherent with low-amplitude displacements, and the data were then used to adjust/control higher strains. The stress amplitude was calculated on the basis of Hooke's law as long as the specimen deformation was nominally elastic. Ultrasonic loading was applied in well-controlled pulses (200 ms on/ 800 ms off) to reduce the heat generated in the specimen [20]. In addition, a circuit of high-pressure airflow was applied to cool down the specimen.

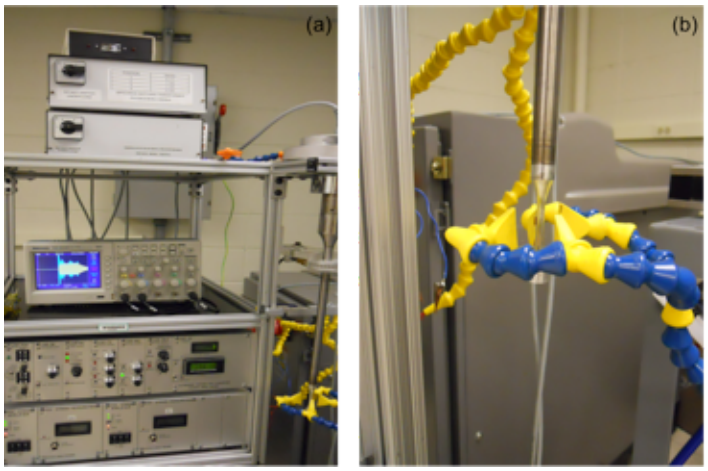

Figure 3: Ultrasonic fatigue test apparatus: (a) ultrasonic fatigue test instrument; (b) specimen mounted on test system with attached cooling system.

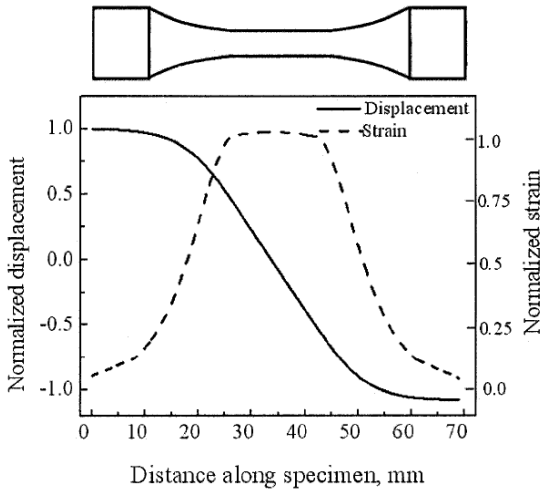

Figure 4: Distributions of displacement and strain along the specimen [19]

Results and Discussion

Microstructure

Fig. 5a is a composite image showing the morphology and distribution of microshrinkage porosity inside the as-cast A206 specimen. To quantitatively analyze the 2-D porosity population distribution, a large area (7 mm x 5 mm) metallographic cross-section was examined to ensure a sufficient number of pores were counted. Sizes and distributions of observed pores were statistically analyzed with the image processing software, Image J. The size of the porosity was characterized with the equivalent circular diameter (ECD), which is defined as:

$$D = 2 \times \sqrt{\frac{A}{\pi}} \tag{1}$$

where A is the 2-D projected area of porosity.

The average porosity ECD was 37 μm, and the total area fraction of the microshrinkage porosity was 0.65%. Fig. 5b shows the ECD frequency distribution histogram. More than 80% of ECDs were between 20 to 50 μm. After FSP more than 97% of pores were closed due to plastic movement of the material under the applied downward and shear forces. Clearly, FSP is a viable means of mitigating porosity in cast components.

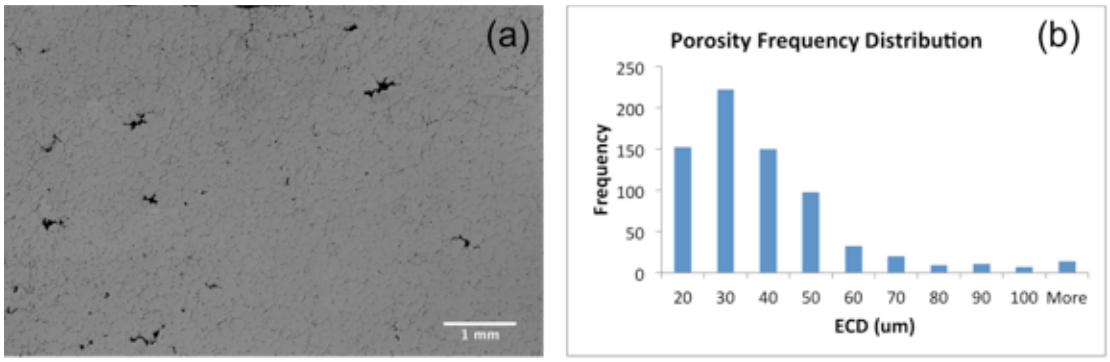

Figure 5: Casting defect analysis: (a) distribution of porosity within a large area of as-cast A206; (b) plot showing the frequency distribution of observed porosity equivalent circular diameters.

Fig. 6 shows optical micrographs of A206 pre- and post-FSP; grain boundaries and grain size are clearly depicted in Figs. 6a and 6b. Dendritic structures and large grains whose diameters are >400 μm in diameter were observed in the as-cast A206 microstructure. However, after FSP, fine and equiaxed grains less than 10 μm in size were observed, a reduction of almost one order of magnitude. In addition, second phases were also refined. The as-cast A206 contained second phases that were mainly coarse needle-like $CuAl_2$-CuAl compounds (Fig. 6c) whose aspect ratio varied from 4 to 8. However, these large second phases transformed during FSP into fine and uniformly dispersed second phase particles (Fig 6d) with an aspect ratio of ~1.

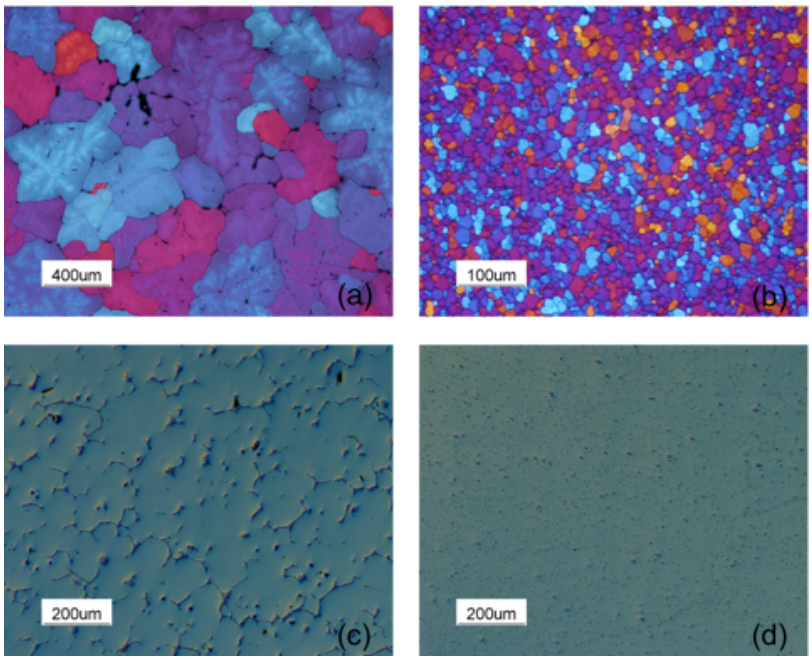

Figure 6: Micrographs of as-cast A206 and FSP A206: (a) grain morphology of as-cast A206; (b) grain morphology of FSP A206; (c) second phase distribution of as-cast A206; (d) second phase distribution of FSP A206.

Fig. 7a and Fig. 7c are image quality (IQ) maps taken from the as-cast A206 and FSPed A206 samples. The IQ map is overlaid with grain boundary angles. The "high angle" boundaries are defined as boundaries with misorientations exceeding 15 degrees, whereas the "low angle" boundaries are defined as boundaries with misorientations between 1 and 15 degrees. High-angle grain boundaries are marked in blue color. When quantitatively analyzing the grain boundary characteristics, for instance, calculating the fraction of high-angle boundaries, the minimum boundary misorientation should be defined. In this case, the minimum boundary misorientation was set to 1. Fig. 7b and Fig. 7d are histograms showing the frequency distribution of grain boundary misorientation angles in the as-cast and FSPed specimens. The fraction of high angle grain boundaries increased from 26.6 % to 76.7% after FSP. It has been proposed that a large fraction of high angle grain boundaries will affect the resultant mechanical properties [21].

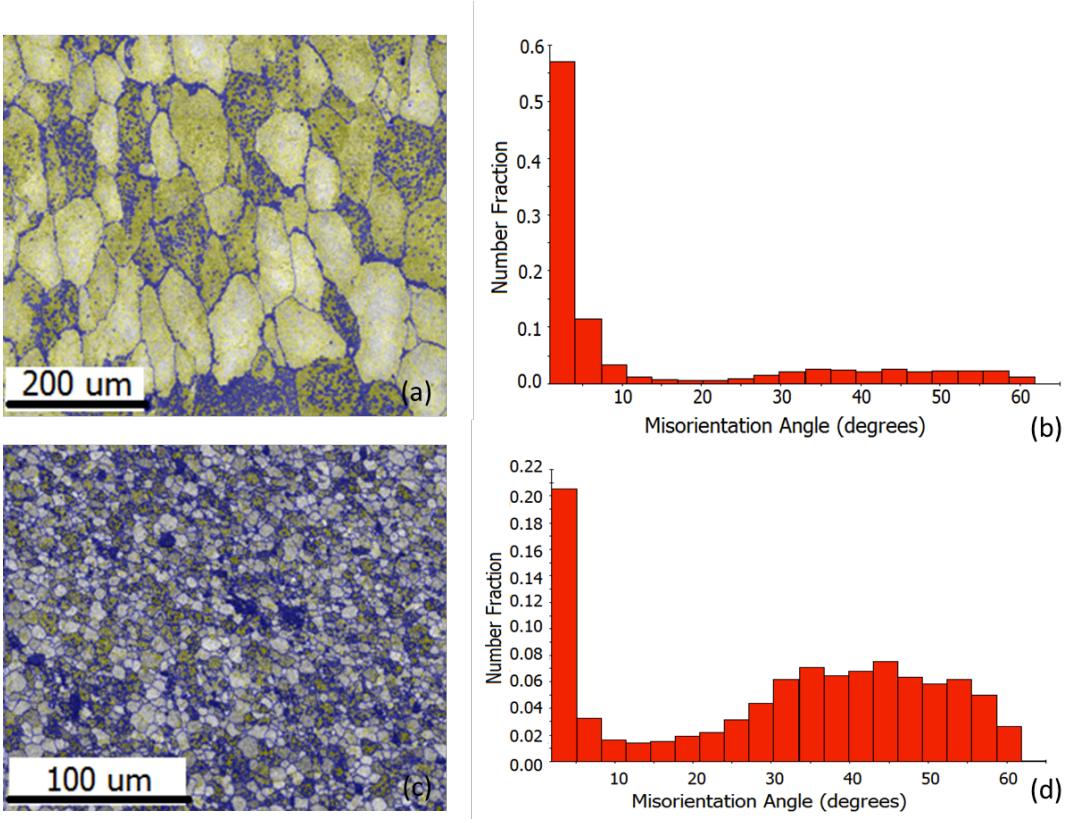

Figure 7: Images showing grain boundary characteristics: (a) as-cast A206 IQ map overlaid with grain boundary angles; (b) frequency distribution of the grain boundary misorientation angles of the as-cast A206; (c) FSPed A206 IQ map overlaid with grain boundary angles; (d) frequency distribution of the grain boundary misorientation angles of FSPed A206.

Hardness

Fig. 8 shows the average Knoop hardness (HK) profiles for the as-cast and FSPed A206 specimens. The average microhardness of the as-cast A206 was 85 HK, and one can note

the variation in values (see the error bar of the as-cast data in Fig. 8b). The existence of casting defects, i.e., porosity and inclusions, as expected decreased the measured hardness values. The microhardness profiles of the FSP processed specimen were selected from two locations in the FSP nugget, as described above. The material between the surface of the work piece and location 1 had sufficient contact with the tool shoulder, and this region is referred to as the shoulder-affected zone. During FSP, the material in the shoulder-affected zone experienced a huge downward force as well as a shear force from the tool shoulder. The strain/strain rate in this region was higher than in other parts of the FSP region. As a result, the stirring action of the tool broke the coarse Al-Cu intermetallic compounds and resulted in fine Al-Cu particles whose sizes were smaller in the shoulder-affected zone than in other regions. These finer Al-Cu particles generated a strong pinning effect and prevented coarsening of the recrystallized grains. As can be noted in Fig. 8a the grain size at location 1 is smaller than that in the middle of the FSP region. Location 2 is in the middle of the FSP nugget, and the material in this region is representative of the typical microstructure of FSPed A206. Microhardness profiles in the shoulder-affected zone (location 1) as well as in the middle of the FSP zone (location 2) were higher in value than the microhardness profile in the parent material. Moreover, the material in the shoulder-affected zone became even harder. The improvement in the observed microhardness of FSPed material is contributed to the following:

(i) Grain refinement – The mechanism of grain refinement during FSP is through dynamic recrystallization. The grain size decreased from ~400 μm (in the as-cast condition) to ~5 μm at location 1, to ~10 μm at location 2. The finer grains impede dislocation movement and strengthen the material. As per the Hall – Patch relation [7,8], the finer microstructure in location 1 resulted in a higher resistance to deformation than the microstructure at location 2.

(ii) Precipitation hardening – The temperature measured near the tip of the tool during FSP was about 480 °C. However, since the thermocouple cannot reach the tip of the tool during FSP, the actual local temperature of the material is about 40-50 °C higher than the measured value. A206 Al alloy is a heat-treatable alloy, and the Al-Cu and Al-Mg-Cu phases dissolve into the α-Al and form a supersaturated solid solute at this temperature. GP zones precipitated from supersaturated solid solution during the cooling stage of FSP and in the interval between FSP and the test. Precipitation hardening contributes to the observed increase in hardness.

(iii) Casting defect alleviation – FSP eliminated porosity, which improved the average hardness of the material.

(iv) Break-up of second phases – Al-Cu intermetallic compounds found in A206 alloy are harder than the α-Al. Once these coarse second phases are broken into fine particles by the stirring action of the FSP tool probe, the homogeneously dispersed second phase particles improve the hardness of the material.

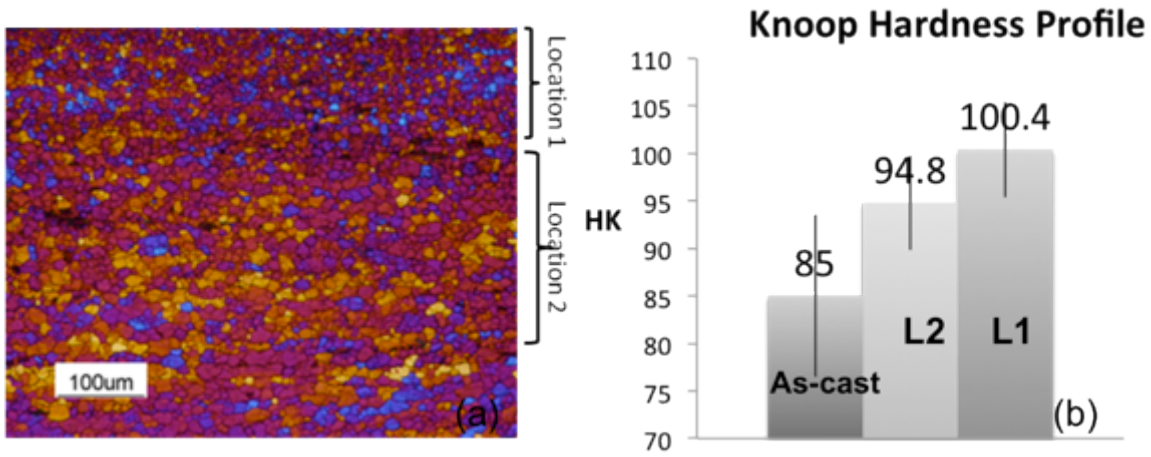

Figure 8: Microhardness profile of the as-cast A206 and FSP A206: (a) grain size difference in the FSP region; (b) microhardness.

Tensile Properties

Fig. 9 shows typical stress-strain curves of as-cast A206 and FSP A206. The yield stress of the as-received A206 was 190 Mpa; the UTS was 262 Mpa, and the elongation was 5.6%. FSP resulted in a simultaneous increase in strength and ductility: Elongation increased to 14.4%. Both yield stress and UTS increased after FSP; yield stress increased from 190 Mpa to 230 Mpa, and the UTS increased from 262 Mpa to 348 Mpa. The Quality Index (QI) has been used [22] to express the quality of a casting in terms of both strength and ductility. A higher index number indicating increased mechanical property values. The quality index (QI) is calculated as per the following relationship [22]:

$$QI = UTS + k \times \log E \tag{2}$$

where UTS is the ultimate tensile strength in MPa; k is a constant whose value is 150 for aluminum alloys; E is the elongation. Since yield strength (YS) is less influenced by casting defects, QI is related to yield strength and elongation, by representing UTS with YS .

$$YS = UTS - 60 \times logE - 13 \tag{3}$$

And thus, QI can be expressed as

$$QI = YS + 210 \times logE + 13 \tag{4}$$

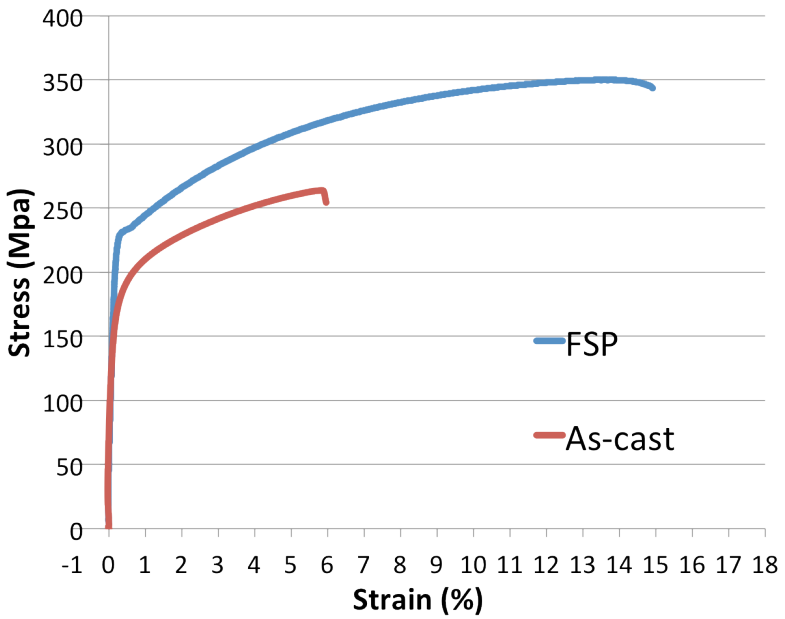

Figure 9: Representative stress-strain curve for (a) as-cast A206; (b) FSPed A206.

Table 1. Tensile Property Values

		Y.S (Mpa)	UTS (Mpa)	El (%)	Q.I
As-cast (AC)		190	262	5.6	360
AC + T4		234	330	8.5	442
AC + T7		265	337	6.2	445
FSP		230	348	14.4	486
Pre-FSP-HT	AC + T4 + FSP	259	366	14.2	513
	AC + T7 + FSP	262	370	12.2	503
Post-FSP-HT (heat treat)	FSP + T4	255	408	17.6	529
	FSP + T4 (FB)	262	407	19.8	547
	FSP + T6 (FB)	283	436	17.7	558
	FSP + T7 (FB)	260	408	16.6	529

The FSPed specimen showed enhanced tensile properties with the QI increasing from 360 to 486; properties for a variety of conditions are shown in Table 1. The enhanced yield stress can be attributed to dislocation pinning effect. FSP introduces a large number of dislocations in the work piece. Although dislocation density was lowered by dislocation annihilation during the recovery stage, there still remain many dislocations within the refined grains or at the grain boundaries. At grain boundaries, dislocations accumulate and interact with one another, and these serve as pinning points or obstacles that significantly impede dislocation motion during loading. Moreover, the fine and uniformly dispersed second phase particles interact with the tangled dislocations, which further prohibit dislocation movement and thus strengthen the material during low strain deformation. This resulted in the high yield strength values measured. The increased UTS is due to porosity elimination as well as refinement of grains and second phases.

Ductility was also improved after FSP with the elongation increasing by more than 150%. The significant ductility enhancement is due to the higher work hardening rate of the FSPed A206 compared with the as-cast A206. Work hardening is the strengthening of a metal during the plastic stage caused by dislocation movement within the crystal structure [23]. In this study, the work hardening rate is expressed by an index that was calculated by taking the first derivative of the stress-strain curve shown in Fig. 9. This index manifests the trend of the change in the work hardening rate. The variation of the work-hardening-rate index as a function of tensile stress is shown in Fig. 10. It should be noted that there were obvious data noise as shown in Fig. 10; however, by considering interpolated stress values at sufficiently separated strain intervals during differentiation the noise was minimized [21]. Compared with the work hardening rate of the as-cast specimen, the work hardening rate of the FSPed specimen is always higher and it decreases at higher stresses, however at a lower rate. The work hardening rate is directly related to dislocation density; a higher dislocation density resulting in a higher work hardening rate. There are two forms of dislocations: intrinsic and extrinsic dislocations. Y.H Zhao et al [24] found that low-angle grain boundaries trap more extrinsic dislocations during deformation, and these extrinsic dislocations interact with intrinsic dislocations, which lead to annihilation of dislocations. In other words, low-angle grain boundaries are sinks for dislocations, and they promote recovery and reduced dislocation density [23]. FSP produced a large fraction of high-angle boundaries, and the ductility was increased because of the high work hardening rate [21, 24, 25].

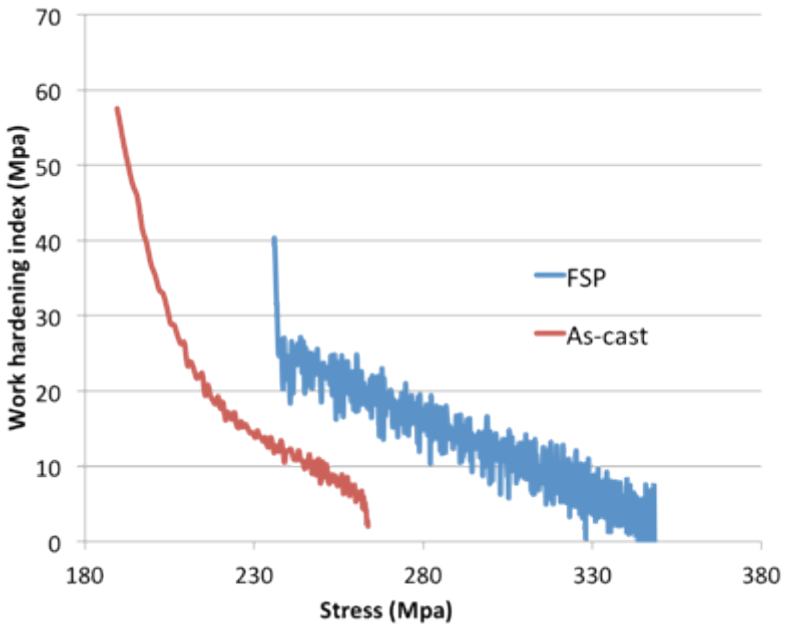

Figure 10: Variation of the index of the work hardening rate as a function of the stress.

FSP was also carried out on heat-treated A206 work piece whereas previous FSP work was done on as-cast structures. Commercial T4 and T7 heat treatments were selected, and they were termed as pre-FSP heat treatments. Al A206 alloy is a heat-treatable alloy; during solution treatment copper goes into solution. Subsequent to quenching, the solid solution is supersaturated and second phases form via solid-state precipitation. At

temperatures below the solidus, the equilibrium state consists of two solid phases: solid solution, α, plus an intermetallic compound phase θ (Al_2Cu); several non-equilibrium precipitates nucleate before the formation of the equilibrium phase θ [26]. Moreover, the addition of magnesium greatly accelerates the reaction by precipitation of the S' phase [27]. The following notations give the various stages of second phase formations for alloy A206:

$$SSS \rightarrow GP\ zones \rightarrow \theta'' \rightarrow \theta' \rightarrow \theta\ (Al_2Cu)$$

$$SSS \rightarrow GP\ zones \rightarrow S'\ (Al_2CuMg) \rightarrow S\ (Al_2CuMg)$$

For T4 heat treatment, the temperature is in the natural aging range, and the distribution of copper atoms changes from random to disk-like planar aggregates (GP zones); these form on particular crystallographic planes of the aluminum matrix [27]. GP zones cause coherency strain fields that increase the alloy's resistance to deformation. When aging at a higher temperatures, i.e., during T6 heat treatment, second phases form (θ'' and θ') having a composition similar to Al_2Cu; θ'' and θ' further increasing the strength of the material. With increasing aging temperature, i.e., in the T7 heat treatment, the material is in the over-aged condition. Precipitates (θ' and θ), incoherent with the matrix and larger in size, form. Although strength decreases in the T7 condition, dimensional stability is increased.

AC+T4+FSP increased the strength as well as the ductility of the work piece compared with AC+T4. However, AC+T7+FSP did not strengthen the material as high as AC+T7. The strength resulting from AC+T4+FSP is similar in the strength range that resulted from AC+T7+FSP. These results indicate that the strengthening phases went into solution during FSP, and the thermal-cycle that resulted during FSP was inadequate to preserve a desirable precipitation upon cooling [28].

Strengthening phases can re-precipitate during post-FSP heat treatment. It was noted that when solution treatment was carried out in a conventional furnace, where the heating rate is ~5 °C/min, grain growth occurred. In Fig. 11 one can see the average grain size increased from 7 μm to more than 200 μm. The coarse grain structure deteriorated tensile properties. The observed grain growth during post-FSP solution treatment was abnormal grain growth (AGG), which is defined as excessive growth of a few grains at the expense of a few small grains that formed subsequent to recrystallization [29]. The abnormal grain growth is also called secondary recrystallization. Many common aluminum alloys experience grain growth during solution treatment; this phenomenon can occur during or after recrystallization, especially if the work piece has been subjected to a critical amount of prior cold work [27]. The critical range of cold work is ordinarily about 5 to 15%. Grain growth that occurs during recrystallization is a function of composition, structure, degree of cold work, and heating rate; temperatures in excess of 455 °C in common alloys can lead to secondary recrystallization grain growth problems [27].

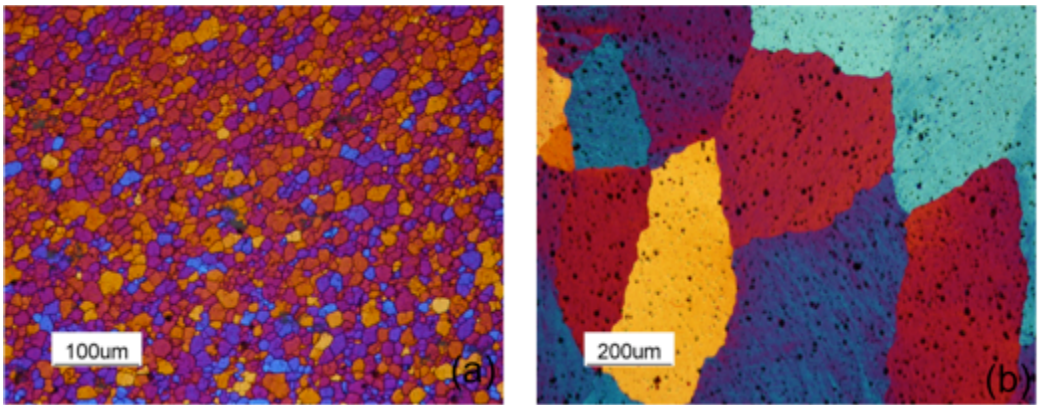

Figure 11: Microstructure of the FSPed A206 after solution treatment showing the occurrence of abnormal grain growth (AGG).

Abnormal grain growth has negative effects on the mechanical properties [13, 14] of FSPed work piece, and the subject of several studies [30-34]. It has been shown that AGG can occur in both wrought Al alloys [30-32] as well as in cast Al alloys [34]; it can be avoided or mitigated by varying the FSP parameters [32, 34]. Charit and Mishra [33] investigated the effects of tool rotation speed and tool traverse speed, and they established a microstructural instability map for FSPed 7075 Al with respect to AGG. Jana et al [34] pointed out that AGG can be controlled by repeated multiple FSP passes in the nugget at a high rotation rate. Several key factors affecting AGG are: (i) amount of input heat; (ii) strain gradient in the FSP nugget; (iii) size and volume fraction of the second phases that can generate a pinning effect; (iv) average grain size, and (v) grain boundary mobility.

Humphrey's model [35] relating microstructural stability and abnormal grain growth has been useful to shed light on microstructural stability of the material during post-FSP thermal cycle [33, 34]. In this model, the size and amount of second phase particles as well as the size of the equiaxed grains contribute to the pinning effect [35]. The particle pinning term is represented by a dimensionless parameter, Z, which is conveyed as

$$Z = \frac{3F_V R}{d} \tag{5}$$

In equation (5), the material is considered to contain a volume fraction F_V of spherical second-phase particles of diameter d and grains/subgrains whose mean equivalent radius is R.

There are two roots defining the bounds between stable growth (normal grain growth) and unstable growth (abnormal grain growth). After simplification, values of the two bounds can be obtained by solving [35]:

$$(4Z\text{-}1)X^2 + 4(1\text{-}Z)X - 4 = 0 \tag{6}$$

Values of the two X roots can be plotted as a function of Z. The lower bound X_{min} is the size ratio of the smallest grain/subgrain that can grow abnormally, and the upper bound

X_{max} is the maximum value that this ratio can achieve once growth is complete [35].

The value of X is a function of Z. Depending on different Z values, there are five regimes on the X-Z plot [35].

Z = 0 normal grain growth
0< Z < 0.1 broadening of grain size distribution
0.1 < Z < 0.25 abnormal growth and normal grain growth
0.25 < Z < 1 abnormal grain growth but no normal grain growth
Z > 1 no growth
In this study, the FSP nugget contained uniformly dispersed fine Al_2Cu particles whose diameters were ~ 2.5 μm. Their volume fraction was approximated with the area fraction of these particles, and the latter was calculated via the image process software. The estimated F_V is ~3% and the mean equivalent grain radius is ~ 5 μm. The pinning parameter, Z, calculated by fitting these numbers into Equation (5), is 0.18, which indicates that abnormal grain growth coexisted with normal grain growth.

Once grain growth occurs, it is not reversible. However, there are ways to reduce the potential of grain growth. The present study investigated two methodologies to mitigate AGG. The first method was developed to intensify the particle pinning effect, in other words, to increase the value of Z. Theoretically, if Z is large enough (>1), there will be no grain growth. Using this concept, FSP was applied on cast Al alloy A224, which was an alloy specially made for this test. The alloy contains ~0.18% Zr, and the amounts of other elements in A224 are similar to that in A206. The nominal composition of this alloy is shown in Table 2. Another method to prevent grain growth was to apply the solution treatment in a fluidized bed, which increased the kinetics of heat treatment.

Table 2. Composition of A224 Alloy

Cu	Zr	Si	Mg	Fe	Mn	Cr	Ni	Ti
5.260	0.180	0.067	0.024	0.083	0.336	0.003	0.007	0.057

Fig. 12 shows two micrographs taken from the post-FSP solutionized A224 specimen. The solution cycle was the same as the one stated in the previous paragraphs. Although AGG was observed in the top layer (~400 μm) of the FSP region, the grain size was confined within 20 μm in most parts of the FSP region (see Fig. 12a). In Fig. 12b we can see that there were many fine particles dispersed at the grain boundaries. Zr additions in the range of 0.1% to 0.3% are commonly used to form a fine precipitate of an intermetallic particle (Al_3Zr) in aluminum alloys. This precipitate does not cause appreciable precipitate hardening; however, the purpose is to produce finely divided and dispersed particles that retard or inhibit recrystallization and grain growth in the subsequent heating [3, 5, 36]. In this case, the Al_3Zr precipitate particles were incoherent with the matrix, and the size of the precipitate particle was ~ 1 μm, much smaller than the

size of the Al_2Cu particle. These fine thermal resistant particles dispersed at the subgrain/grain boundaries, intensifing the pinning effect and reducing the diffusion rate to inhibit grain growth.

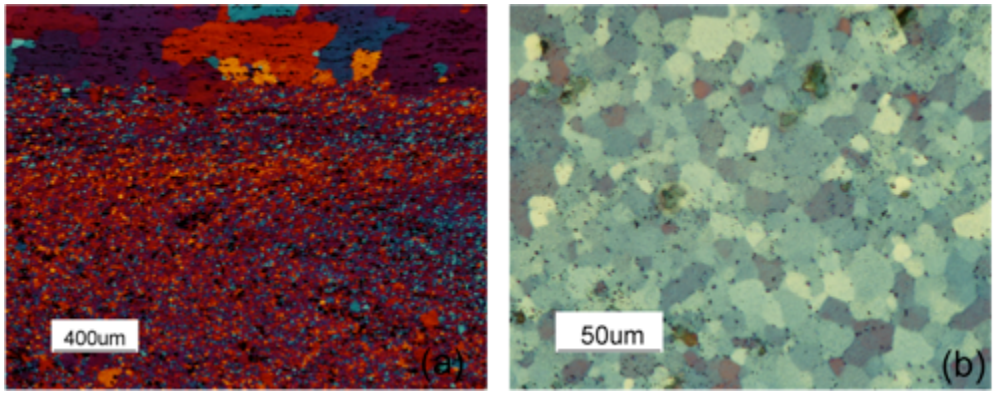

Figure 12: Microstructure of the FSPed A224 after solution treatment: (a) localized grain size; (b) grains in a larger region.

The amount of Zr element in A206 is not as great as in A224; however, applying a fast heating rate for the solution treatment can reduce the potential of grain growth. For this purpose, the fluidized bed was used. With the fluidized bed, the time required to heat up the specimen was reduced. The heating rate was 5 °C/s in the conventional box furnace, whereas it was 45 °C/s the fluidized bed, increased by an order of magnitude. Fig. 13 shows two micrographs taken from the A206 specimen that was solutionized with the fluidized bed. The grain size was less than 50 μm (see Fig. 13a). Fig. 13b is a collage of 24 micrographs that shows the grain size distribution in the whole FSP region. Larger grains were observed in the surface layer of the work piece; however, grains in the middle part of the FSP region were small. The localized grain coarsening was due to the relatively larger residual strain providing a higher driving force for grain growth during subsequent heat treatment. Tensile properties were affected. This was especially seen in the ductility of the specimen that had been solution-treated in the fluidized bed; the ductility was higher than that of the specimen that had been solution- treated in the conventional furnace. Values of the properties are shown in Table 1 in which FB refers to the fluidized bed. The solution stages of the post-FSP T6 and post-FSP T7 heat treatments discussed in the following paragraphs were all carried out in the fluidized bed.

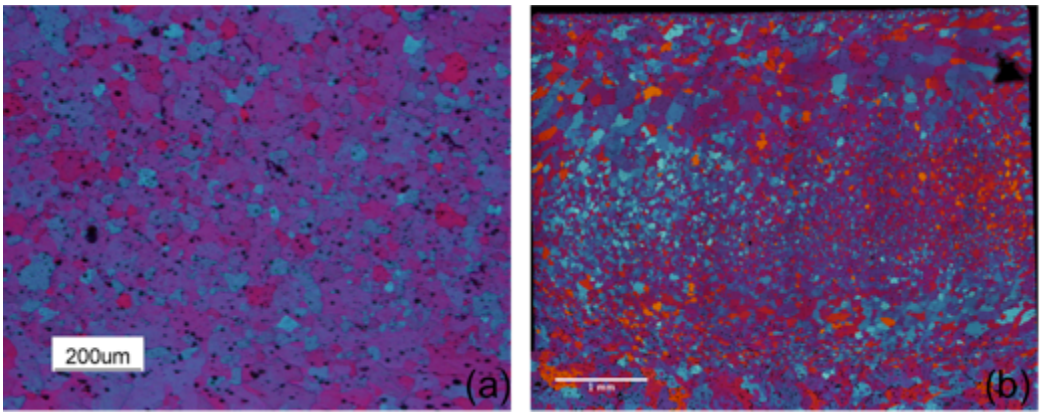

Figure 13: Microstructure of the FSPed A206 after fluidized bed solution treatment: (a) localized grain size; (b) grains in the whole FSPed region.

As shown in Table 1, both the post-FSP-T6 and post-FSP-T7 heat treatments resulted in the further improvement in tensile properties compared with the specimen that was processed only by FSP. This indicated that strengthening phases that went into the solution during FSP can re-precipitate in the subsequent thermal cycle. Characteristics of these precipitation phases in the stir zone after post-FSP heat treatment have been studied with TEM [28, 37, 38]. C.A.W. Olea et al [28] found that the stir zone after post-FSP heat treatment gave rise to equiaxed grains fully covered with very thin precipitates in the size range of 2-10 nm that were randomly distributed in the matrix. There was also precipitation along the subgrain boundaries inside the small-recrystallized grains. In addition, the precipitation occurred preferentially on the network of dislocations or subgrain boundaries.

Fig. 14 shows the aging curves of the FSPed A206. The specimen was aged at 155°C. The peak of the yield strength was 320 Mpa which it showed after aging for 36 hours. In contrast to the obvious increase in the yield strength with aging time, there was only a slight increase in the ultimate tensile strength from 2 hours to 36 hours. Elongation was decreased gradually from 23% to 10% between 4 hours to 50 hours, and it stayed around 8% for long-time aging (over 50 hours).

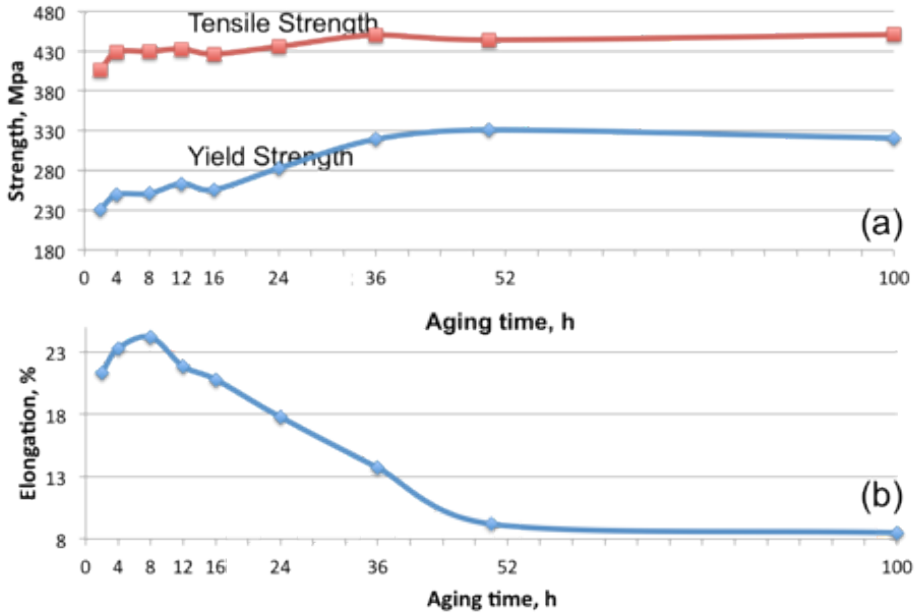

Figure 14: Aging curves of the FSPed A206 after T6 heat treatment: (a) variations in the YS as a function of time; (b) variations in the UTS as a function of time; (c) variations in the elongation as a function of time.

Fatigue Properties

Commonly, when the cyclic load is run to 10^8 or 10^9 cycles (in the ultrasonic fatigue mode), the S-N curve flattens out [39]. The value of the stress amplitude at 10^8 or 10^9 cycles is the fatigue strength of the material and this number is important in industrial applications. A crack can initiate in the specimen when the cyclic load is at or below this value; however, the crack cannot propagate to cause the final failure because the driving force for crack propagation is very low [39, 40]. So far, the value of the fatigue strength cannot be estimated accurately because of the existence of scatters on the S-N plot when the cyclic load is run to very high cycles. In this study, the staircase test methodology [41] was used to reduce the above concern and associated errors and to correctly determine the fatigue strength of the A206 aluminum alloy. The fatigue test was carried out in the ultrasonic fatigue test mode at a series of stress amplitudes within a pre-determined range.

It is important to understand how the staircase test method works. Specimens are tested sequentially. The first specimen is tested at a certain stress level. If the specimen fails at a number of cycles less than the pre-determined number (for example 10^8 cycles in this study), the next specimen is then tested at a stress level one step lower than the failed specimen. If the specimen survives at the level of the pre-determined cycles (termed as run-outs), the next specimen is tested at a stress level one step higher than the previous specimen. This methodology is repeated throughout the test program. The final outcome is expected to be that approximately half of the specimens fail and the other half do not, as the specimens are tested around the mean fatigue strength.

In this study the stress amplitude range for the as-cast specimen was between 86 Mpa and 95 Mpa, and the step space was 3 Mpa. The stress amplitude range for the FSPed specimen was between 160 Mpa and 190 Mpa, and the step space was 3 Mpa. The staircase data were analyzed following the Dixon-Mood method [41], which assumes that the fatigue strength is normally distributed. The fatigue strength was then expressed in terms of the mean value and standard deviation. Equations (7) ~ (11) were applied to calculate the mean fatigue strength value and standard deviation [42].

As denoted by $\mathbf{n_i}$, the number of the less frequent event at the stress level **i**, two quantities **A** and **B** are calculated:

$$A = \sum i \times n_i \tag{7}$$

$$B = \sum i^2 \times n_i \tag{8}$$

The estimate of the mean is then

$$\mu_{S,FL} = S_0 + S_d \times \left(\frac{A}{\sum n_{\square}} \pm \frac{1}{2} \right) \tag{9}$$

where the plus sign (+) is used if the more frequent event is survival and the minus sign (-) is used if the more frequent event is failure. The standard deviations are then estimated as

$$\sigma_{S,FL} = 1.62 \times S_d \times \left[\frac{B \sum n_i - A^2}{(\sum n_i)^2} + 0.029 \right] \tag{10}$$

$$\text{if } \frac{B \sum n_i - A^2}{(\sum n_i)^2} \geq 0.3$$

$$\text{or } \sigma_{S,FL} = 0.53 \times S_d \tag{11}$$

$$\text{if } \frac{B \sum n_i - A^2}{(\sum n_i)^2} \leq 0.3$$

Nomenclature

A	quantity used in the Dixon and Mood method
B	quantity used in the Dixon and Mood method
$\mathbf{S_0}$	lowest or initial stress level
$\mathbf{S_d}$	stress increment
i	stress level
$\mathbf{n_i}$	number of the less frequent event at the numbered stress level **i**
$\boldsymbol{\mu}_{S,FL}$	mean of a fatigue limit
$\boldsymbol{\sigma}_{S,FL}$	standard deviation of a fatigue limit

The experimental staircase test results are shown in Fig. 15. Assuming the fatigue strength follows a normal distribution, the mean value of the fatigue strength at 10^8 cycles and the population standard deviation for the as-cast A206 were 85.5 Mpa and 1.56 Mpa, respectively; for the FSPed A206 they were 165 Mpa and 1.56 Mpa, respectively. It can be noted that the fatigue strength of the FSPed A206 was twice the value compared with that of the as-cast A206. For the as-cast specimen, the ratio of the fatigue strength to the yield strength was ~45% (the yield strength was 190 Mpa, and the fatigue strength was 85 Mpa), whereas for the FSPed A206, the ratio increased to 75% (the yield strength was 225 Mpa, and the fatigue strength was 165 Mpa). These results indicated that the improved fatigue properties after FSP were due to the elimination of casting defects.

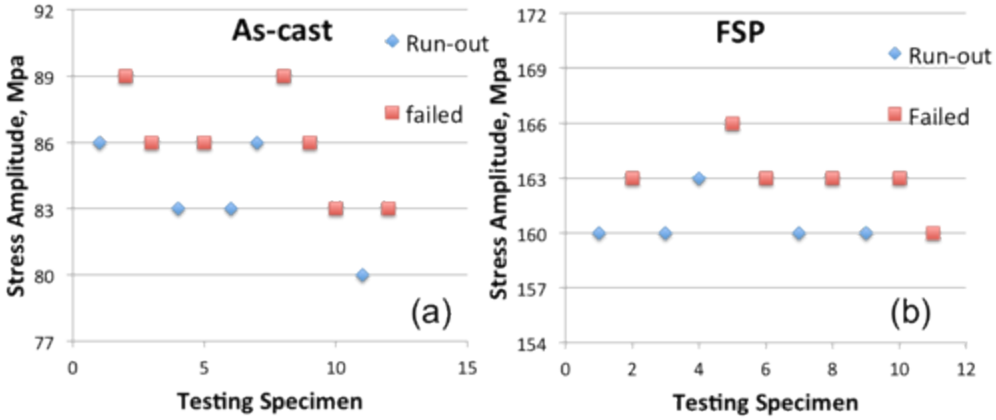

Figure 15: Experimental staircase test results at 10^8 cycles for (a) as-cast A206; (b) FSPed A206.

In addition to the staircase test, some complementary tests were carried out at higher stress amplitudes to fill in the high-stress-amplitude regions data and obtain the general trend of the S-N data. To generate the S-N trend curve, the general non-linear model [43] was applied to represent the data. The general non-linear model has the following form:

$$log\ N = A_0 + A_1 \times Log\ (S_{max} - S_0) \tag{12}$$

In this equation, A_0, A_1, and S_0 are constants that can be calculated from the measured (S, N) data by the iterative least square method. It can be seen from the equation that when $S_{max} \rightarrow S_0$, $N \rightarrow \infty$. This means that S_0 is the endurance limit, or fatigue life, of the alloy at the given test conditions. There are several methods of dealing with the run-outs [43]. In this study, a trial analysis was performed with all the run-outs excluded and a mean S/N curve was derived with the cycles close to 10^8. Two standard measures, (i) the standard error of estimate (*se*), and (ii) the correlation coefficient (*r*), were commonly used to show the effectiveness of the equation in representing the measured data [43].

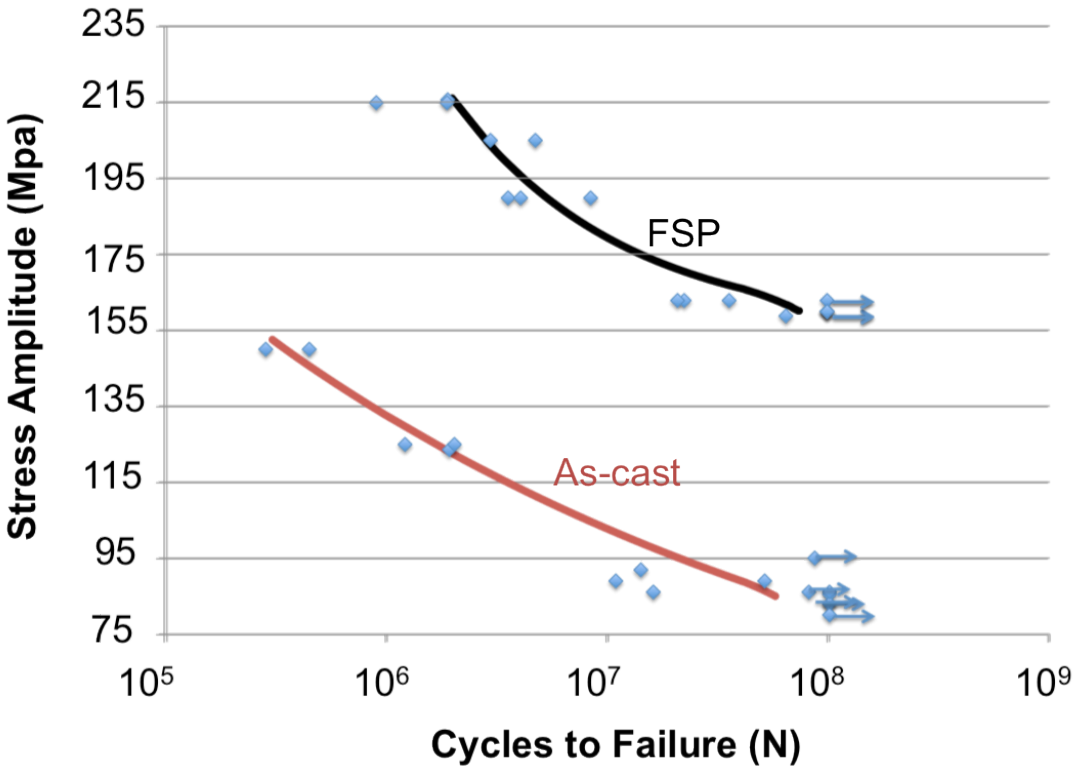

Figure 16: S-N curves of the as-cast A206 and FSPed A206.

Fig. 16 shows S-N plots of the as-cast A206 and FSPed A206. Specimens cycled to 10^8 cycles without failure were regarded as run-outs, and they are marked with arrows in the figure. The influence of FSP on the fatigue behavior of A206 was obvious. Compared with the S-N curve of the as-cast specimen, the S-N curve of the FSPed specimen was shifted to the regime where both the stress amplitude and life cycle were higher. FSP resulted in a larger fatigue resistance in the high stress amplitude regime. The fatigue life was still longer than 10^6 cycles even when the stress amplitude reached 215 Mpa. Moreover, the FSP S-N plot had a steep transition within the high stress amplitude range (> 160 Mpa). The number of cycles was only reduced by less than one order of magnitude when the stress amplitude increased from 175 Mpa to 215 Mpa. The total fatigue life consists of the number of cycles required for crack initiation and the number of cycles required for crack growth and propagation to the failure. For cast Al alloys at high stress amplitudes, the crack is readily initiated at casting defects, such as, large pores due to high stress concentration at these locations. In such cases, fatigue life is dominated by the crack growth and propagation stage from the initial crack to the final fatal crack length, because the crack initiation life is negligible [44, 45]. FSP significantly elongated the fatigue life under high stress amplitudes, which indicated that the number of cycles at the crack initiation stage also had an impact on the total fatigue life.

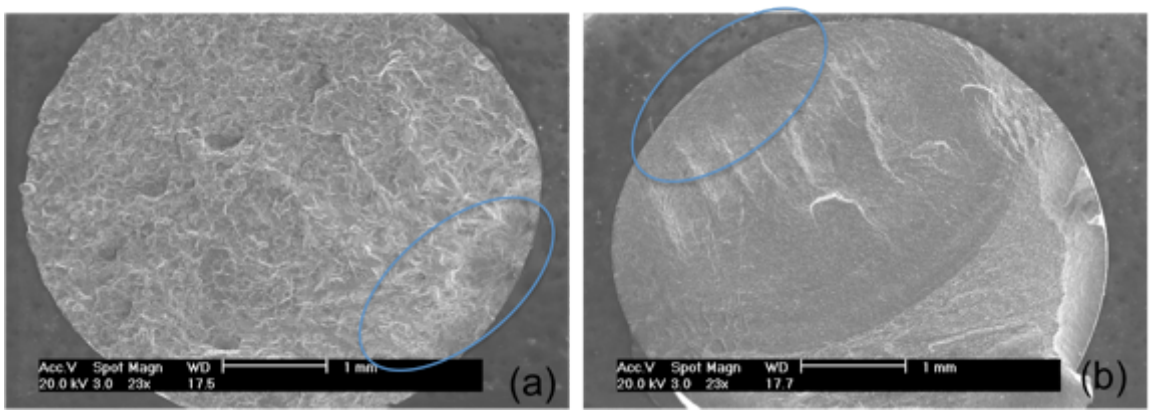

Figure 17: Fracture surfaces of (a) as-cast A206; (b) FSPed A206.

In general, the fracture surface consists of three distinct regions: the crack initiation region, the steady crack growth and propagation region, and the fast fracture region. These regions can be identified in the fracture surfaces shown in Fig. 17. The as-cast specimen had a porous fracture surface; large porosities whose diameters were up to 200 μm were observed in the SEM micrograph (Fig. 17a). The crack initiation region for the as-cast specimen (marked with the blue circle in Fig. 17a) was characterized by one/some microshrinkage porosities located near the edge of the specimen. In the crack growth region, there were a large number of transcrystalline cleavages radiating from the crack initiation region. FSP is an advanced tool that can be used to repair the porosity-type casting defect. In this study, 97% of porosities were eliminated after FSP, especially the relatively larger porosities. From Fig. 17b one can see there were no obvious casting defects in the fracture surface. The fatigue crack initiated from some weak points near the edge where the concentrated stress was high. In the crack propagation region, cracks grew perpendicularly to the load direction. River patterns that were parallel to the crack-advancing direction were clearly revealed. The final region contained the fast fracture that was caused by overloading

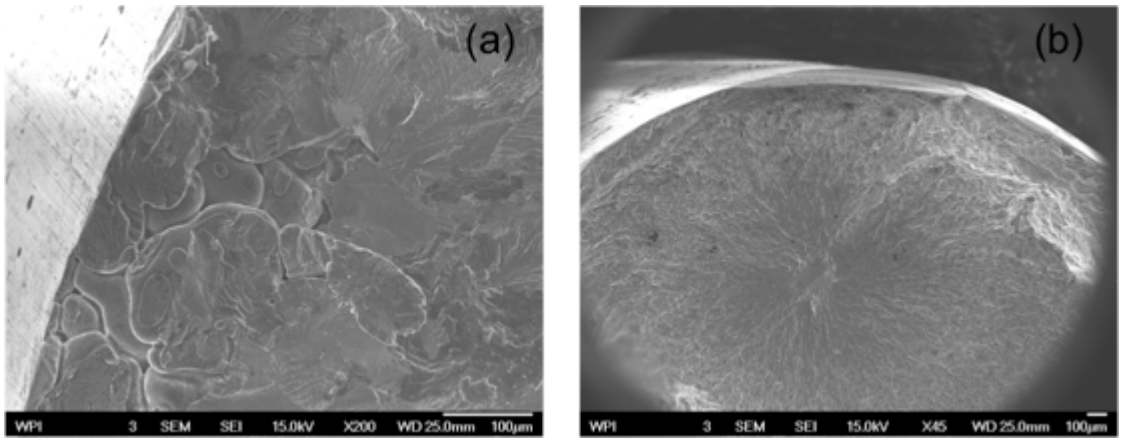

Figure 18: Fatigue crack initiators of (a) as-cast A206; (b) FSPed A206.

Fig. 18 shows two SEM micrographs depicting the different fatigue crack initiators of the as-cast and FSPed specimens. For the as-cast specimen, the fatigue crack originated from a pore near the edge (Fig. 18a). The irregular shape of the pore and the dendrite appearance indicated that the pore was a microshrinkage porosity. The ECD of the microshrinkage porosity was 109 μm. Fracture surfaces of 14 as-cast specimens were closely examined with SEM, and all cracks were caused by microshrinkage porosities located at or very close to the specimen surface. Statistical analysis results of these porosities, i.e., ECDs, the number of porosities, and the corresponding stress amplitudes are shown in Table 3. Approximately one-third, actually 36%, of the fatal cracks were initiated from multiple porosities that were in close proximity to each other (marked with M in Table 3). If a fracture surface contained multiple porosities, the ECD of the largest porosity located near the edge was listed in the Table. This study found that the crack always initiated from a large porosity, and there was no obvious correspondence between the ECD of the porosity and the applied stress amplitude. These large size porosities were totally eliminated via FSP, which improved the resistance to the crack initiation stage. For the FSPed specimen, although most coarse Al-Cu components were broken into uniformly dispersed fine Al-Cu particles, there were still some larger size Al-Cu compounds remaining in the matrix. Fatigue crack was readily initiated on the interface between the large and hard precipitates and the matrix (see Fig. 18b).

Table 3: Statistical analysis of the crack initiators

Sample No.	σ (Mpa)	ECD (um)	Single or Multiple
1	83	180	S
2	89	105	S
3	90	60	M
4	123.5	39	S
5	86	91	M
6	95	69	M
7	86	146	M
8	150	155	S
9	89	78	M
10	125	107	M
11	125	109	M
12	83	107	M
13	86	141	M
14	104.5	48	S

Fig. 19a is a composite micrograph showing the fatigue crack path in the as-cast specimen. The crack initiated from a pore at the edge (the right side end in Fig. 19a) and grew along a tortuous path through the specimen. The tortuous path was due to the roughness-induced closure [46, 47]. Grain boundary played an important role to increase roughness. The crack advancing along a straight direction coincided with a certain slip system until it met with the grain boundary that caused the crack to change the orientation. The average grain boundary spacing of the as-cast A206 was about 200 μm, and the crack growth path deflection was quite noticeable from the lateral side view.

Apart from grain boundaries, the morphology of the intermetallic phase also affected crack growth. Fig. 19b and Fig. 19c are optical micrographs taken from two locations under higher magnification showing the crack behavior towards different intermetallic phase morphologies. The crack changed its direction when it met the round particle (Figure 19b), which indicated that particles with low aspect ratio had high fatigue resistance. However, for the needle-like shape particles, the crack can easily break through them and advance directly (see Fig. 19c). Fig. 19d shows the crack path in the FSPed specimen. Although apparently the crack path was not as tortuous as that in the as-cast specimen, the fatigue propagation was retarded for several reasons: (i) a large amount of fine dispersed Al_2Cu particles whose aspect ratio was about 1; (ii) increased yield strength of the material which caused the plasticity-induced closure – the crack growth rate was decreased during crack propagation due to the reduction in the microcracks (damage) in the material [48]; and (iii) refined grains – the number of grain boundaries increased, which intensified grain boundary strengthening.

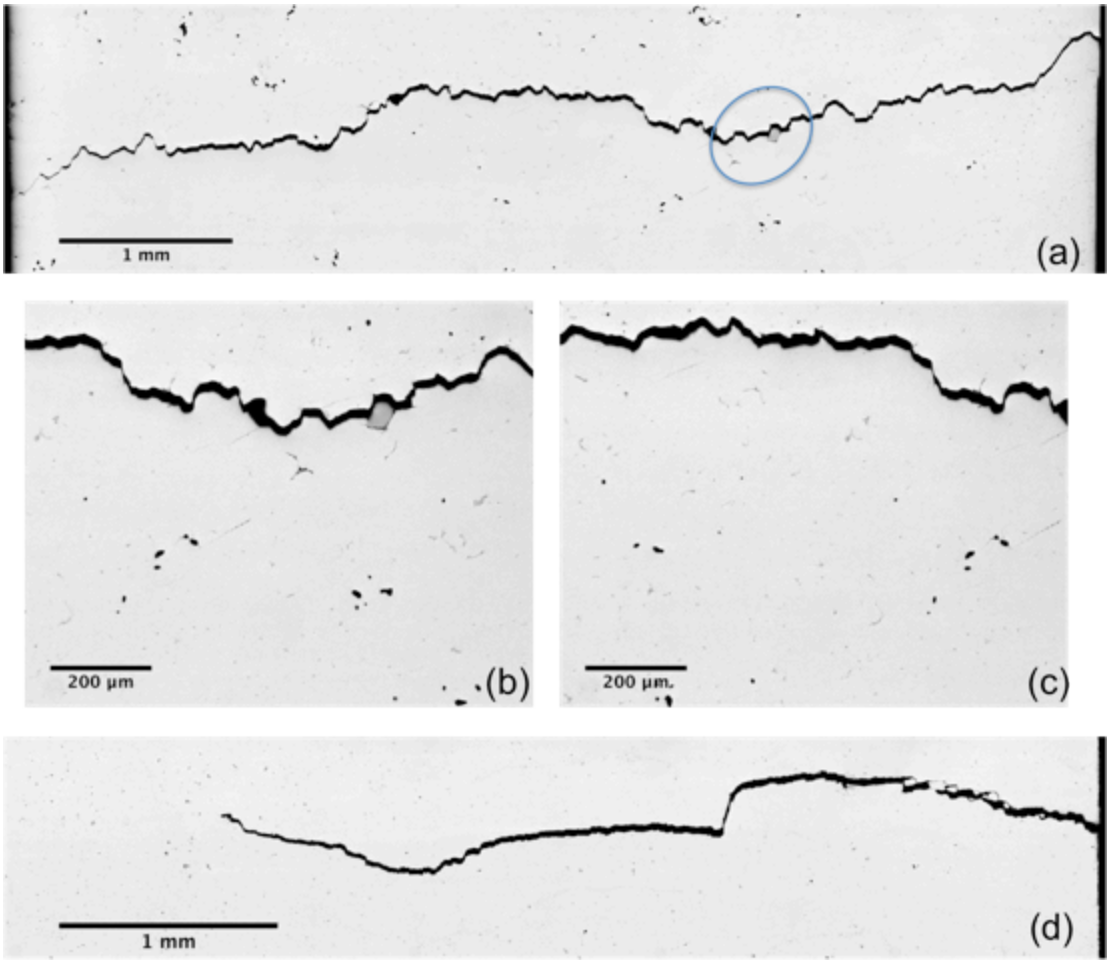

Figure 19: Fatigue crack morphology: (a) crack growth path through the as-cast specimen; (b) interaction of crack with a round second phase particle; (c) crack breaking through needle-like shaped second phase particles; (d) crack growth path through the FSPed specimen.

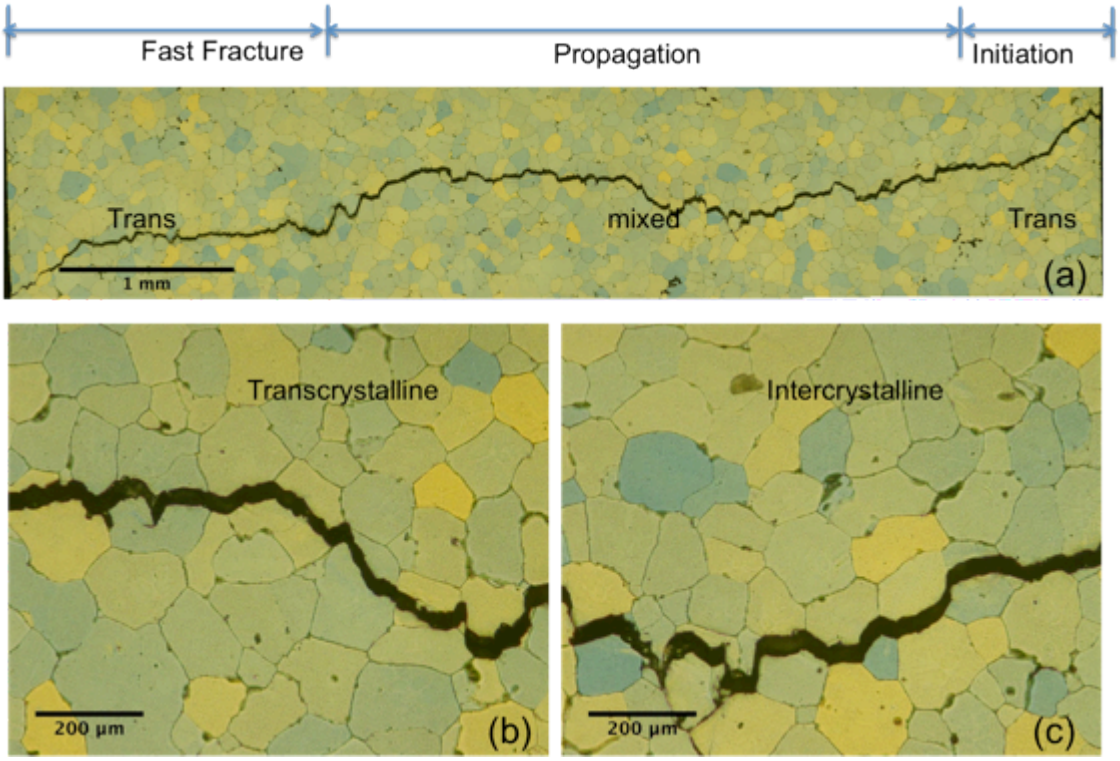

Figure 20: Crack profile in the as-cast A206: (a) both the transcrystalline and intercrystalline fractures are observed in the fracture surface; (b) a higher magnification optical micrograph showing the transcrystalline fracture mode; (c) a higher magnification optical micrograph showing the intercrystalline fracture mode.

Figure 20 shows some lightly-etched optical micrographs depicting the crack path interaction with grains in the as-cast specimen. The crack path followed a transcrystalline mode in both the initiation region and the fast fracture region. However, it transferred into a mix of the transcrystalline crack and intercrystalline crack in the crack growth and propagation region. The transcrystalline crack and intercrystalline crack in the propagation region were revealed under higher magnification in Fig. 20b and Fig. 20c respectively. Furthermore, the coexistence of these two types of cracks were evidenced in Fig. 21, which contained two SEM micrographs taken from the crack propagation region in a typical fracture surface of the as-cast specimen. The transcrystalline crack was characterized by some cleavages and ligaments that were parallel to the crack growth direction. The energy required for this kind of fracture was low [49] because there was no crystallographic lattice deformation – only the atomic bonds were broken [50]. At the early stage of crack growth, the driving force for the initial crack was too low to overcome the grain boundary barrier – the fracture tended toward the transcrystalline. In the crack propagation region, once the driving force for the crack growth exceeded the energy barrier caused by dislocations and interface cohesion forces on the grain boundaries, it was possible for the crack to follow the intercrystalline mode. Facets with different orientations observed in the crack propagation region (see Fig. 21b) indicated the intercrystalline fracture remained. At the final stage, a fast fracture was formed to

break the specimen. The crack growth rate was very high, and the crack followed the transcrystalline mode.

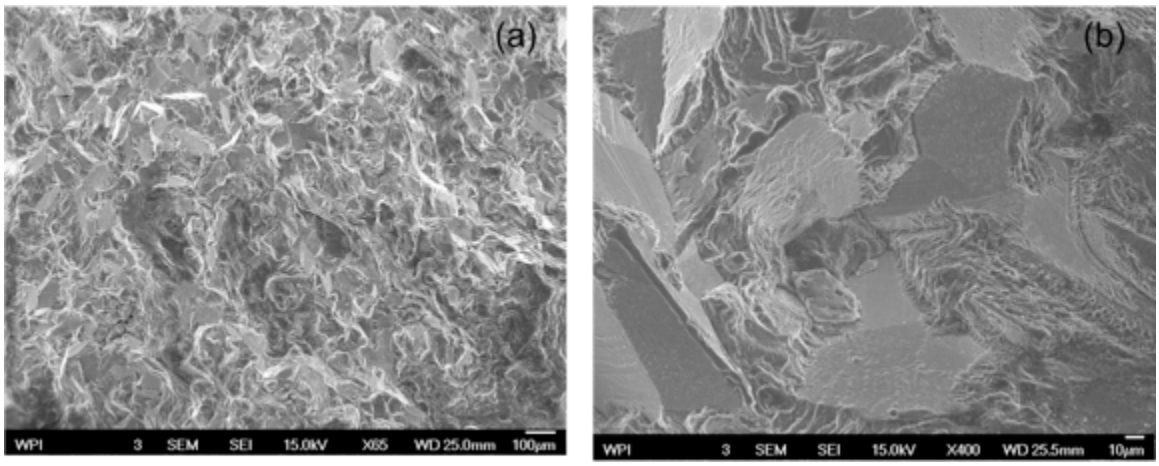

Figure 21: SEM micrographs showing typical fracture surfaces of as-cast A206: (a) both the transcrystalline and intercrystalline fractures are observed in the crack propagating region; (b) a higher magnification micrograph showing the coexisted transcrystalline and intercrystalline fractures.

Fig. 22 shows the typical fracture surface of the FSPed specimen. A large size hard and brittle Al_2Cu compound was observed in the crack initiation region (Fig. 22a). The microstructural discontinuity caused a localized stress concentration, and the fatigue crack was easily initiated. Chevrons pointing to the local crack initiation point (the center of the Al_2Cu) were observed when closely examining the torn Al_2Cu phase (Fig. 22b). In the crack propagation region, rivers formed by connected cleavage steps were clearly seen (Fig. 22c). These rivers were wiggly because high-angle grain boundaries and dispersed fine second phase particles acted as obstacles for crack propagation [50]. Moreover, the refined grain size also increased the slip resistance [51]. The crack had to deflect to find an easier slip orientation; this caused the formation of new river patterns. The fracture path followed the transcrystalline mode, which was in agreement with other studies [52, 53]. The interlinkage of voids formed dimples in the final fatal region (Fig. 22d), and this region had a typical ductile fracture surface. The presence of dimples indicated that plastic deformation took place.

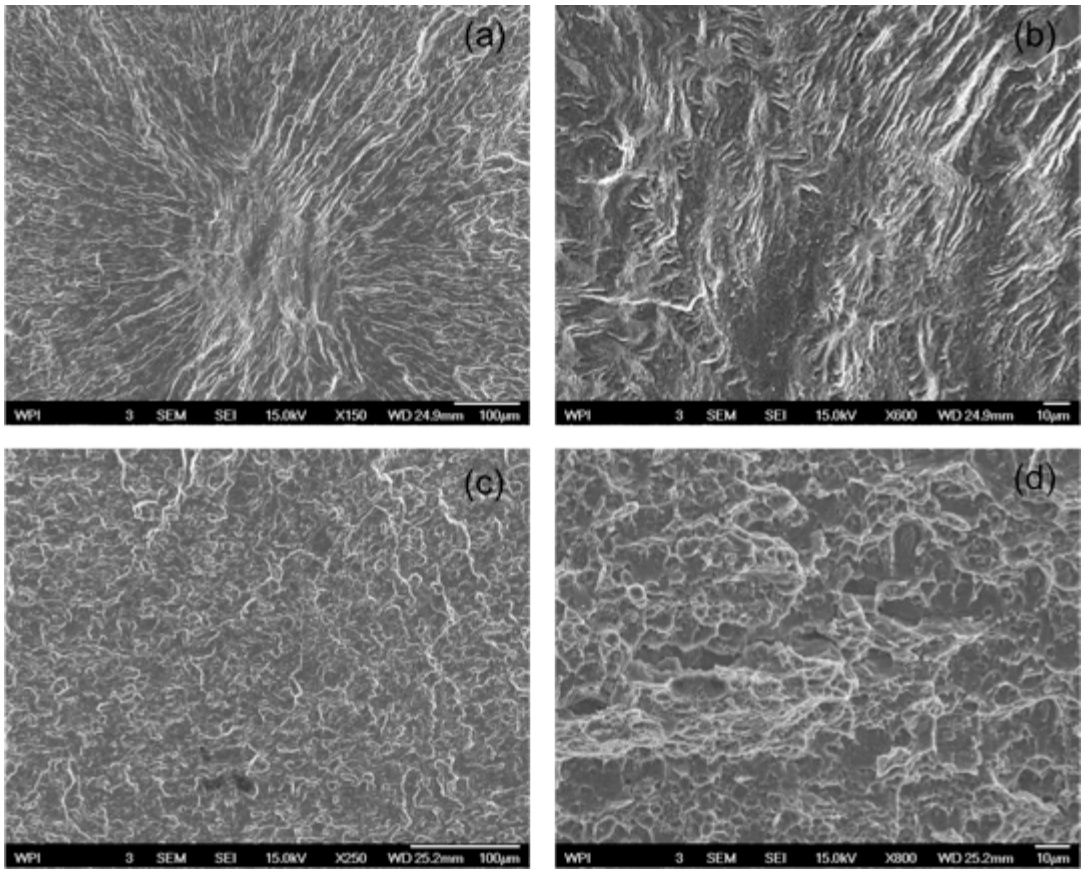

Figure 22: SEM micrographs showing typical fracture surfaces of FSPed A206: (a) the initiation of a crack; (b) higher magnification micrograph taken from the initiation showing chevrons; (c) crack propagation region; (d) failure region containing dimple coalescence.

Summary

FSP has been applied as an advanced post-processing tool to locally manipulate the A206 microstructure to refine and strengthen the material. Outcomes of this work are summarized as follows:

- FSP resulted in an increase in the average microhardness value and a reduction in the microhardness scatter. The improved microhardness property was attributed to grain refinement, precipitation hardening, cast defect alleviation, and uniform fine second phase particle dispersion.

- FSP resulted in the simultaneous improvement in the strength and ductility of the A206 alloy. The yield strength was increased due to dislocation pinning/grain boundary strengthening. The enhanced ductility was due to a higher work hardening rate. FSP was applied on T4 and T7 heat-treated A206 work pieces. Strengthening phases precipitated in pre-FSP heat treatments went into solution

during FSP and the thermal-cycle was inadequate for the strengthening phases to re-precipitate during/after FSP. Post-FSP heat treatments resulted in further improvement of tensile properties. Grain growth occurred when the solution treatment of the FSPed specimen was carried out in a conventional furnace. The abnormal grain growth can be prevented or alleviated in two ways: (i) using a higher heating rate for the solution treatment, or (ii) introducing more fine particles that had high thermal resistance to increase the pinning effect.

- Fatigue properties of the FSPed A206 and as-cast A206 were investigated by running ultrasonic fatigue tests. The S-N curve of the FSPed specimen was shifted to the region where both the stress amplitude and the fatigue life were higher. The fatigue strength of the material at 10^8 cycles was estimated via the staircase test method. The fatigue endurance limit was two times in value after FSP compared with the limit of the as-cast A206. The improved fatigue property was due to the increased fracture resistance in both the crack initiation stage and the crack growth and propagation stage.

References

[1] W.M. Thomas, E.D. Nicholas, J.C. Needham, M.G. Murch, P. Templesmith, C.J. Dawes, 1991, (G.B. Patent Application No. 9125978.8).

[2] Z.Y.Ma, 2008, "Friction Stir Processing Technology: A Review," The Minerals, Metals & Materials Society and ASM International 2008, Anonymous pp. 642.

[3] P. Cavaliere, and P.P. De Marco, "Friction stir processing of a Zr-modified 2014 alloy", Materials Science and Engineering A, Vol. 462, pp. 206-210. (2007)

[4] P. Cavaliere, and A. Squillace, "High temperature deformation of friction stir processed 7075 aluminium alloy", Materials Characterization, Vol. 55, pp. 136-142. (2005)

[5] P. Cavaliere, "Effects of friction stir processing on the fatigue properties of a Zr-modified 2014 alloy", Materials Characterization, Vol. 57, pp. 100-104. (2006)

[6] N. Sun, and D. Apelian, "Friction stir processing of Al cast alloys for high performance applications", Journal of Metals, Materials and Minerals, Vol. 63, pp. 44-50. (2011)

[7] R.Z. Valiev, A.V. Korznikov, and R.R. Mulyukov, "Structure and properties of ultrafine-grained materials produced by severe plastic deformation", Materials Science and Engineering A, Vol. 168, pp. 141-148. (1993)

[8] R.Kapoor, P.S. De, and R.S. Mishra, "An analysis of strength and ductility of ultrafine grained Al alloys", Materials Science Forum, Vol. 633-634, pp. 165-177. (2010)

[9] Friction stir welding and processing, edited by R. S. Mishra and M.W. Mahoney, ASM International, Materials Park, Ohio. (2007)

[10] Y.J. Kwon, N.Saito and I. Shigematsu, “Friction stir process as a new manufacturing technique of ultrafine grained aluminum alloy”, Journal of Materials Science Letters, Vol. 21, pp. 1473-1476. (2002)

[11] D.C. Hofmann and K.S. Vecchio, “Submerged friction stir processing (SFSP): An improved method for creating ultra-fine-grained bulk materials”, Materials Science and Engineering A, Vol. 234, pp. 234-241. (2005)

[12] Z.Y. Ma and R.S. Mishra, “Development of ultrafine-grained microstructure and low temperature (0.48 T_m) superplasiticity in friction stir processed Al-Mg-Zr”, Scripta Materialia, Vol. 53, pp. 75-80. (2005)

[13] I. Charit and R.S. Mishra, “High strain rate superplasticity in a commercial 2024 Al alloy via friction stir processing”, Materials Science and Engineering A, Vol. 359, pp. 290-296. (2003)

[14] I. Charit and R.S. Mishra, “Low temperature superplasticity in a friction-stir-processed ultrafine grained Al-Zn-Mg-Sc alloy”, Acta Materialia, Vol. 53, pp. 4211-4223. (2005)

[15] Z.Y. Ma, F.C. Liu and R.S. Mishra, “Superplastic deformation mechanism of an ultrafine-grained aluminum alloy produced by friction stir processing”, Acta Materialia, Vol 58, pp. 4693-4704. (2010)

[16] M. Mahoney, C. Fuller, M. Miles, and W. Bingel, “Thick plate bending of friction stir processed aluminum alloys”, Friction stir welding and processing III, K. Jata, M, Mahoney, R. Mishra, and T. lienert, Ed., TMS, 2005, pp 131-137.

[17] Z.Y. Ma, S.R. Sharma, and R.S. Mishra, "Microstructural modification of as-cast Al-Si-Mg alloy by friction stir processing," Metallurgical and Materials Transactions A, Vol. 37 pp. 3323-3336. (2006)

[18] Z.Y. Ma, S.R. Sharma, and R.S. Mishra, "Effect of friction stir processing on the microstructure of cast A356 aluminum," Material Science and Engineering A, Vol. 433 pp. 269-278. (2006)

[19] X. Zhu, “Ultrasonic fatigue test of E319 cast aluminium alloy in the long lifetime regime”, Dissertation for the degree of Doctor of Philosophy, University of Michigan, 2007

[20] H. Mayer, “Fatigue crack growth and the threshold measurements at very high frequencies”, International Materials Reviews, Vol. 44, pp. 1-34. (1999)

[21] R.Kapoor, N. Kumar, R.S. Mishra, C.S. Huskamp, and K.K. Sankaran, "Influence of fraction of high angle grain boundaries on the mechanical behavior of an ultrafine grained Al-Mg alloy", Materials Science and Engineering A, Vol. 527, pp. 5246-5254. (2010)

[22] S.Jacob, "Quality index in prediction of properties of aluminum castings – a review", AFS Transactions, Vol. 108, pp. 99-208. (2000)

[23] "Materials and processes in manufacturing", by E. Paul Degarmo, J T. Black, and Ronald A. Kohser, 9th edition, willey, pp. 60

[24] Y.H. Zhao, J.F. Bingert, Y.T. Zhu, X.Z. Liao, R.Z. Valiev, Z. Horita, T.G. Langdon, Y.Z. Zhou, E.J. Lavernia, "Tougher ultrafine grain Cu via high-angle grain boundaries and low dislocation density", Applied Physical Letters, Vol. 92, 081903. (2008)

[25] P.C. Hung, P.L. Sun, C.Y. Yu, P.W. Kao, and C.P. Chang, "Inhomogenous tensile deformation in ultrafine-grained aluminum", Scripta Materialia Vol. 53, pp. 647–652. (2005)

[26] "Phase Transformations in Metals and Alloys", D.A. Porter, K.E. Easterling, M.Y. Sherif, Third Edition, 277-279.

[27] ASM Handbook, Volume 4, Heat treating (1991)

[28] C.A.W. Olea, L. Roldo, J.F. dos Santos, and T.R. Strohaecker, "A sub-strctural analysis of friction stir welded joints in an AA6056 Al-alloy in T4 and T6 temper conditions", Materials Science and Engineering A, Vol. 454, pp. 52-62. (2007)

[29] F.J. Humphreys, and M. Hatherly, Recrystallization and Related Annealing Phenomena, second ed., Pergamon, 2002.

[30] I. Charit, R.S. Mishra and M.W. Mahoney, "Multi-sheet structures in 7475 aluminum by friction stir welding in concert with post-weld superplastic forming", Scripta Materialia, Vol. 47, pp. 631–636. (2002)

[31] Kh.A.A. Hassan, A.F. Norman, D.A. Price, and P.B. Prangnell, "Stability of nugget zone grain structures in high strength Al-alloy friction stir welds during solution treatment", Acta Materialia, Vol. 51, pp. 1923–1936. (2003)

[32] M.M. Attallah and H.G. Salem, "Friction stir welding parameters: a tool for controlling abnormal grain growth during subsequent heat treatment", Materials Science and Engineering A, Vol. 391, pp. 51–59. (2005)

[33] I. Charit and R.S. Mishra, "Abnormal grain growth in friction stir processed alloys", Scripta Materialia, Vol. 58, pp. 367–371. (2008)

[34] S. Jana, R.S. Mishra, J.A. Baumann and G. Grant, "Effect of process parameters on abnormal grain growth during friction stir processing of a cast Al alloy", Materials Science and Engineering A, Vol 528, pp. 189-199. (2010)

[35] F.J. Humphreys, "A unified theory of recovery, recrystallization and grain growth, based on the stability and growth of cellular microstructures—II. The effect of second-phase particles", Acta Materialia. Vol. 45, pp. 5031–5039. (1997)

[36] "Aluminum and Aluminum alloys", edited by J.R. Davis, ASM Special Handbook.

[37] J.-Q. Su, T.W. Nelson, R. Mishra and M. Mahoney, "Microstructural investigation of friction stir welded 7050-T651 aluminium", Acta Materialia, Vol. 51, pp. 713-729. (2003)

[38] A. Sullivan and J.D. Robson, "Microstructrual properties of friction stir welded and post-weld heat-treated 7449 aluminium alloy thick plate", Materials Science and Engineering A, Vol. 478, pp 351-360. (2008)

[39] M.J. Caton, J.W. Jones, H. Mayer, S.Stanzl-Tschegg and J.E. Allison, "Demonstration of an endurance limit in cast 319 aluminum", Metallurgical and Materials Transactions A, Vol. 34, pp 33-41. (2003)

[40] H. Mayer, M. Papakyriacou, B. Zettl and S.E. Stanzl-Tschegg, "Influence of porosity on the fatigue limit of die cast magnesium and aluminium alloys", International Journal of Fatigue, Vol. 25, pp.245-256. (2003)

[41] W.J. Dixon, and A.M. Mood, "A method for obtaining and analyzing sensitivity data", Journal of American Statistical Association, Vol. 43, pp 109-126. (1948)

[42] S. Lin, Y. Lee, and M. Lu, "Evaluation of the staircase and the accelerated tests for fatigue limit distributions", International Journal of Fatigue, Vol. 23, pp.75-83. (2005)

[43] J.B. Conway, and L.H. Sjodahl, "Analysis and representation of fatigue data", ASM International, Materials park, Ohio, 1991.

[44] Y.X. Gao, J.Z. Yi, P.D. Lee and T.C. Lindley, "A micro-cell model of the effect of microstructure and defects on fatigue resistance in cast aluminum alloys", Acta materialia, Vol. 52, pp 5435-5449. (2004)

[45] J.Z. Yi, "Microstructure-based fatigue life prediction for cast A356-T6 aluminum-silicon alloys", Metallurgical and Materials Transactions B, Vol. 37, pp 301-311. (2006)

[46] D.A. Lados, D. Apelian and J.K. Donald, "Fatigue crack growth mechanisms at the microstructure scale in Al-Si-Mg cast alloys: mechanisms in the near-threshold regime", Acta materialia, Vol. 54, pp. 1475-1486. (2006)

[47] D.A. Lados and D. Apelian, “Fatigue crack growth characteristics in cast Al-Si-Mg alloys: part I: effect of processing conditions and microstructure”, Material Science and Engineering A, Vol. 385, pp. 200-211. (2004)

[48] Q.G. Wang, D. Apelian and D.A. Lados, “Fatigue behavior of A356/357 aluminum cast alloys: part II: effect of microstructural constituents”, Journal of Light Metals, Vol.1, pp 85-97. (2001)

[49] Fractography and Atlas of Fractorgraphs. Vol. 9, 8th edition. Metals handbook, American Society for metals, 1974.

[50] Aluminium-Silicon Casting Alloys Atlas of Microfractographs. M. Warmuzek, 2004, ASM International.

[51] P.S. De, R.S. Mishra and C.B. Smith, “Effect of microstructure on fatigue life and fracture morphology on an aluminum alloy”, Scripta Materialia, Vol. 60 pp. 500–503. (2009)

[52] S. Jana, R.S. Mishra, J.B. Baumann and G. Grant, “Effect of friction stir processing on fatigue behavior of an investment cast Al-7Si-0.6Mg alloy”, Acta materialia, Vol. 58, pp. 989-1003. (2010)

[53] P.S. De and R.S. Mishra, “Microstructure evolution during fatigue of ultrafine grained aluminum alloy”, Materials Science and Engineering A, Vol. 527, pp. 7719-7730. (2010)

Chapter III: Composite Fabrication in Cast Al A206 via Friction Stir Processing

Abstract: Using FSP in forming localized or surface composites in castings can be very advantageous and has significant potential for many applications. Consequently, this study was initiated at ACRC to investigate the feasibility of fabricating composites in Al alloy castings via FSP. The study started with the Al A206 alloy matrix via an ex-situ technique, using a pre-machined groove with emplaced reinforcements. Three reinforcement materials (nano-sized tantalum powders, nano-sized SiC powders, and discontinuous reinforced aluminum) and several key processing parameters (number of FSP passes, the amount of the reinforced materials) were investigated and localized composites were produced successfully. This paper will present the experimental set-up, procedure, the microstructure and properties of the resulting composites, and a discussion of the formation mechanism of the composite and the influences of materials and process on the microstructure and properties.

Introduction

Particulate reinforced metal matrix composites (MMCs) have been developed for high performance applications in the aerospace and automobile industries because of several advantages, particularly high topological resistance and enhanced modulus and strength. The MMCs can be produced via several routes, i.e., the powder metallurgy route [1] or the molten metal route [2-4]. However, all these methods have drawbacks. For instance, the powder metallurgy route usually has high costs and limitations in the matrix and reinforcement compositions. Challenges of the molten metal route are casting defects, introducing the particulate reinforcement into the molten metal, and achieving uniform dispersion.

A recent outgrowth of the Friction Stir Welding (FSW) process [5], Friction Stir Processing (FSP) has shown the capability of eliminating casting defects and refining the microstructure at the processed area, resulting in improved mechanical properties. FSP has also proven to be an innovative and viable means of producing components with localized composite structures. FSP uses a high-speed rotating tool, which has a flat shoulder and probe; the probe is forced to penetrate into the fixed work piece, and once the head face of the tool shoulder fully contacts the work piece, the non-consumable tool is forced to traverse the work piece. The frictional heating between the tool and the work piece ensures the matrix has dramatic plastic deformation and property improvement around the moving tool. Making composites using FSP can be done by pre-emplacing the second phase within the work piece, which is transferred into the matrix by stirring and then dispersed in the FSP-processed zone. Producing metal matrix composites using FSP has several advantages compared to traditional methods: (i) the composite region is fabricated locally at pre-determined zones rather than throughout the whole bulk; (ii) the process can easily be incorporated in the post-casting operation in the manufacturing cycle; (iii) since FSP is performed in the solid state, hydrogen porosity, residual stress, as well as many unwanted interfacial reactions between the reinforcement and the matrix are mitigated; and (iv) FSP can be used to repair localized defects.

FSP has been applied successfully in producing Al MMCs through both in-situ and ex-situ syntheses. In 2003, Mishra et al. [6] reported the study of ex-situ fabrication of a SiCp-Al surface composite via FSP. Later FSP was used in producing nano-particle composites [7, 8]. In 2009, Lim et al [7] reported their study of using FSP in producing Al MMCs with reinforcement of multi-walled carbon nanotubes (CNT) of 30-50 nm. In 2010 Yang [8] reported the fabrication of the AA6061/Al_2O_3 nanoceramic particle-reinforced surface composite via FSP. By using FSP for fabricating localized or surface composites, the methodology of introducing the reinforcements into the substrate prior to friction stirring has attracted more and more attention. As an outcome of this research, two techniques were developed in introducing the reinforcement materials. One is forming a thin reinforcement coating on the surface of the matrix work piece prior to the stirring. For example, Zahmatkesh [9] produced an Al-Al_2O_3 surface nanocomposite on Al 2024 substrate by air plasma spraying of Al-10%Al_2O_3 powders to produce an Al-10%Al_2O_3 coating on the substrate. Another method involves placing reinforced particles into some pre-manufactured cavities in the work piece and then conducting friction stirring. The latter has obvious advantages over the former in scalability because it can produce a thicker composite region.
In the in-situ synthesis, FSP has been applied to produce an Al-Ni intermetallic composite [14], an Al-Al_2Cu composite from Al-Cu elemental powder mixtures [15], and an Al-Al_3Ti nanocomposite from Al-Ti elemental powder blends [16].

In fabricating Al MMCs using FSP, most studies have worked on the wrought Al alloys matrix. Because of the widespread applications of Al cast alloys and castings the possibility of using FSP in forming localized or surface composites in castings can be very advantageous and has significant potential for many applications. Consequently, this study was initiated at ACRC to investigate the feasibility of fabricating composites in Al alloy castings via FSP. The study started with an Al A206 alloy matrix via an ex-situ technique, using a pre-machined groove with emplaced reinforcements. Three reinforcement materials and several key processing parameters were investigated and localized composites were successfully produced. This paper will present the experimental set-up, procedure, the microstructure and properties of the resulting composites, and a discussion of the formation mechanism of the composites and the influences of materials and process on the microstructure and properties.

Experimentation

A commercially sand-cast A206 alloy was used as the matrix. The alloy composition was Al-4.33Cu-0.077Si-0.046Fe-0.256Mg-0.343Mn made at Eck Industries. The dimensions of the work piece were 15 x 7.6 x 0.6 cm. FSP was carried out on a HAAS M3 CNC machine at the WPI workshop. The tool shoulder diameter is 16 mm with a screwed taper probe at its end. The length of the probe is 3.2mm. A three-degree tilt angle was applied during processing to generate a forging action at the trailing edge of the tool. Prior to stirring, a slot of 50 (L) x 2 (W) x 4 mm (H) (volume of 400 mm^3) was machined in the work piece; the reinforcement particles were emplaced in the slot fully or partially, and the upper section of the slot was covered and sealed by a pre-friction stirring using a probe of only one millimetre before the final composite fabrication. The slot was

positioned in such a way that the centerline of the tool traversing was offset 1 mm from the centerline of the slot to make sure the advancing side of the tool was in full contact with the reinforced material (see Fig. 1). This project aimed to fabricate composites with different reinforcements. The reinforcements used were (i) 20 nm Ta powders, (ii) 100 nm SiC powders, and (iii) discontinuously reinforced aluminium (DRA, which was already a solid composite containing 50wt% SiC and Si in the 6061 Al matrix).

FSP was carried out at the tool rotating speed of 1000 RPM and traversing speed of 50 mm/min. Effects of the number of FSP passes and the amount of the reinforcement additions were investigated. Analyses were conducted on the samples sectioned perpendicular to the FSP traverse direction. The samples were all ground, polished, and analysed at both as-polished and electrical-chemical etched conditions. Barker's agent was used for etching to reveal the grain size inside the composite layer. An optical microscope, SEM, and EDS were used in studying the microstructures and identifying the grain size, distribution of the reinforcement material, and the ingredients of phases and particles of interest. Microhardness was recorded across the FSP region using a Buehler OmniMet MHT automatic microhardness test system with an applied load of 500 gf.

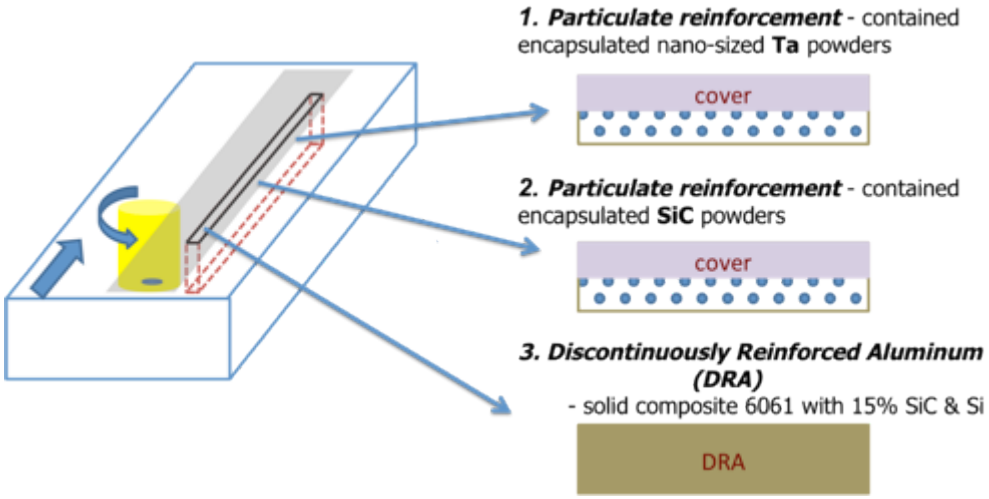

Figure 1: Schematic diagrams of fabricating the composites with different reinforcements in cast A206 matrix.

Results and Analyses

I: Fabrication using nano-sized tantalum powders

The feasibility of composite fabrication via FSP was first demonstrated by mixing in nano-sized Ta powders in alloy A206 matrix. The composite layer was fabricated by 100%-cavity-filling (400 mm^3) of nano-sized Ta powders (the diameter of the Ta powder was about 20 nm). Fig. 2 shows the microstructure of this region under SEM (Fig. 2a) for

the sample fabricated by one pass of FSP. The EDS spectrum, Fig. 2b, confirms that the particles viewed as the bright spots in the marked rectangular area in Fig. 2a, are Ta powders. In the SEM images, the areas in grey are the aluminum and the larger lighter particles (~2 um) are broken Al-Cu precipitates produced by the FSP. In addition to having a smaller size than the precipitate, the Ta powder also differs from the broken Al-Cu particles in shape. Ta powders are round, whereas the Al-Cu intermetallic particles have irregular shapes with sharp edges and corners.

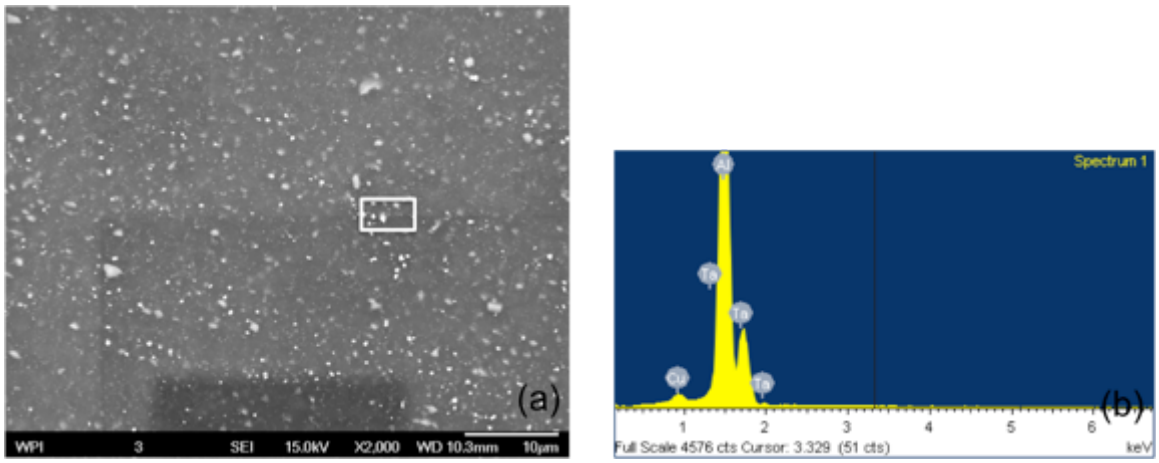

Figure 2： SEM/EDS analysis of the Ta-Al composite layer: (a) SEM image; (b) EDS spectrum showing elements of the detected area.

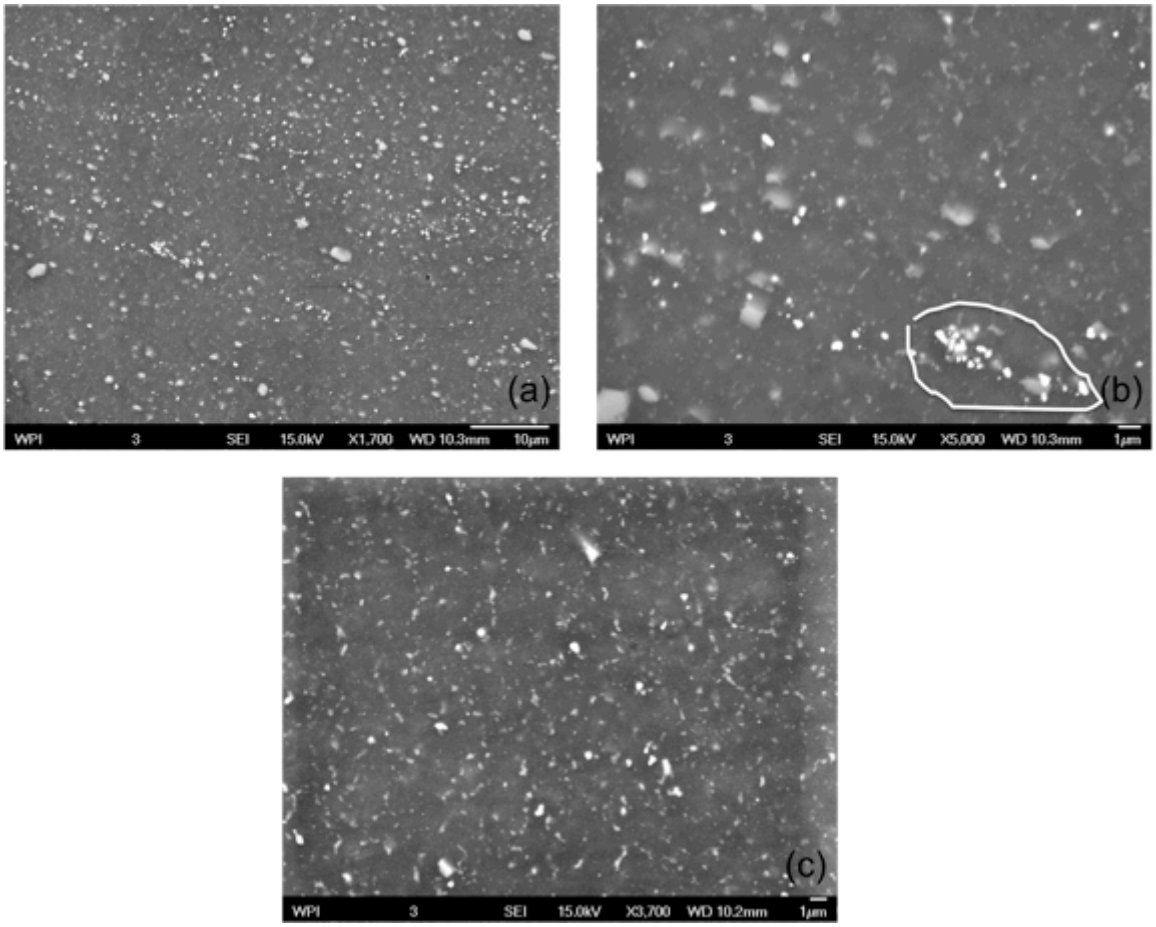

Figure 3: SEM images of the Ta-Al composite layer: (a) overall distribution of Ta powders inside the composite layer after one-pass FSP; (b) Ta powders agglomeration; (c) improved distribution of Ta powders inside the composite layer after two-pass FSP under higher magnification.

Figs. 3a and 3b are images showing distributions of Ta powders in the FSP region after one-pass FSP. Overall, the powders were stirred into the matrix with a good distribution. However, the agglomeration of some powders was observed under higher magnification (Fig. 3b white circle). The distribution of Ta powders was improved after two-pass FSP, as shown in Fig. 3c. Two-pass FSP is simply the process of applying a second FSP pass, which is the same as the first pass, working on the same area, in the same direction, and with the same parameters after the work piece is cooled down from the previous FSP pass. After the second pass the number of the agglomerates was reduced and the Ta powders were dispersed more uniformly.

The successful fabrication of the composite by mixing in nano-sized Ta powders in the cast Al alloy A206 demonstrated that FSP was a viable means to synthesize the composite in the cast Al matrix. The uniform distribution of Ta powders is attributed to the following mechanisms. First, FSP creates sufficient material flow, which is the pre-requisite for the ex-situ synthesis of the composite. In FSP the friction between the tool surface and the substrate generates a large amount of heat and raises the material around

the tool tip to high temperatures; for example, the measured value near the tool tip was around 480 °C. At high temperatures the matrix material was softened and driven to move with the tool. In FSP the interface between the tool and the materials undergoes different modes during the process, which are stick interface, slide interface, and a mixture of both [17]. At the beginning of the process the interface is in stick mode and at this stage the friction between the tool and material generates a large amount of heat, which raises the temperature in the area near the tool tip and thus lowers the stress needed for friction shearing. Once the accumulated heat makes the friction shear stress lower than the internal matrix shear stress generated by the friction stirring, the interface will change from stick to slide mode. At slide mode the friction between the tool and the material decreases, and the heat is generated by the plastic dissipation. This transition can be observed by the decrease in power or torque of the FSP machine. In the sliding condition, the FSP process is just like the extrusion followed by forging [18, 19]. Based on the Arbegast metalworking model [20], during each rotation of the tool, the material in the tool advancing side was first picked up and rotated in front of the tool, and then extruded around the tool to the retreating side. The material in the retreating side rotated around the tool and was extruded into the exiting cavity being vacated by the tool probe as it moved forward. In the vertical direction, the hot metal was forced to move upward by the shear lateral surface and threads of the probe, and then forged downward and consolidated by the bottom surface of the tool shoulder. As a result, this movement creates an adequate material flow, by which the reinforced particles are wrapped and redistributed inside the processed region. Second, in the sealing operation prior to the full friction stirring, the Ta particles are encapsulated inside the Al substrate, which ensures the powders that are confined in the cavity are dispersed by the movement of the matrix material during FSP. The third mechanism is the complete contact between the reinforcement particles and the tool. The FSP tool is made up of two parts: a flat shoulder and a screwed probe at the end of the shoulder. Although the shoulder is the main heating source [21], it can only act on the surface layer of the substrate. Instead, the probe contributes a lot to the material movement in a deeper region – it softens the metal and moves it from its advancing side to the retreating side in the range of the probe diameter [10]. In this study, the tool-traversing route was offset 1 mm from the centerline of the slot and thus produced sufficient contact between the advancing side of the probe and the reinforcing material, which ensured the tool to be able to touch most of the particles and move and disperse them in the matrix.

II: Fabrication using nano-sized SiC powders

SiC/Al composites have high strength as well as good corrosion resistance. These composites have been produced by casting and are probably the most commonly used composites. Most of the SiC/Al composites are fabricated with large size SiC particles (μm scale), and few can be produced with nano-sized SiC reinforced particles. The aim of this study is to locally fabricate the SiC/Al composites in areas or surfaces of the casting using smaller particle sizes (nano scale). Following the success of the synthesis of the localized Ta/Al composite, FSP was successfully applied in fabricating the SiC particle-reinforced cast alloy A206 matrix composite using the same setup and procedure as was used in making the Ta/Al composite. The results showed that the distribution of nano-

sized SiC powders in the matrix was quite similar to that of Ta powders (see Fig. 4). The spectrum in Fig. 4b shows that the particles within the white rectangular frame in Fig. 4a are SiC, and the large particle on the left corner of Fig. 4a is a broken Al-Cu particle. The average size of the initial SiC particles was about 100 nm but some large SiC particles of up to 0.5 μm can be observed in the composite layer. These large and irregular SiC particles are formed by sintering of some small SiC particles at high temperature.

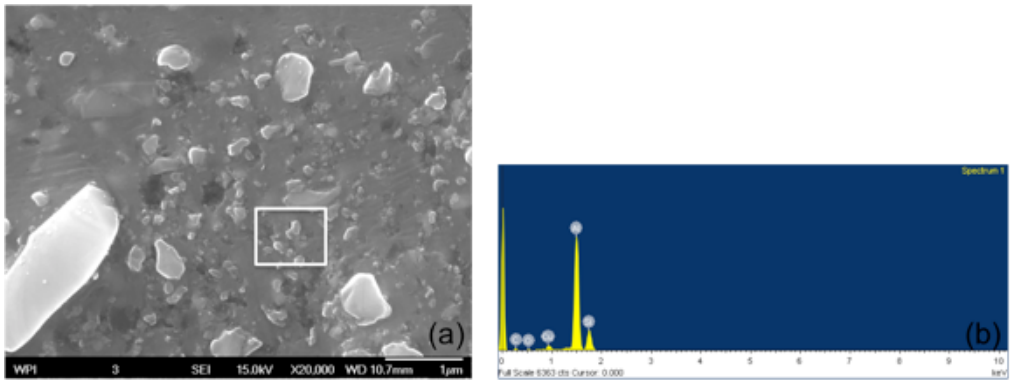

Figure 4:(a) SEM image of the SiC-Al composite; (b) EDS spectrum showing the ingredients of the square-marked area in (a).

Effects of the amounts of particle addition on the particle distribution and composite quality were studied. Tests were conducted on two levels of particle addition: one was 200 mm^3, which filled half of the slot whose volume was 400 mm^3; another was 400 mm^3 which fully filled the slot. The macrographs of the transverse section of the FSP region are shown in Fig. 5; (a) for the half-filled slot and (b) for the fully filled slot. There pictures are composite pictures, which represent a large area, and cover the entire FSP region and vicinity. Fig. 5a shows that when the particles filled half of the slot, or the smaller amount of particles was added, the particles were prone to move towards the bottom of the FSP region on the retreating side; few SiC particles can be observed in the top of the FSP region and not many in the middle of the FSP area. When more SiC particles were added, the distribution was improved, as Fig. 5b illustrates showing that the particles were dispersed more uniformly than in Fig. 5a. Changing process parameters seemed not to change much of this trend in the tested ranges.

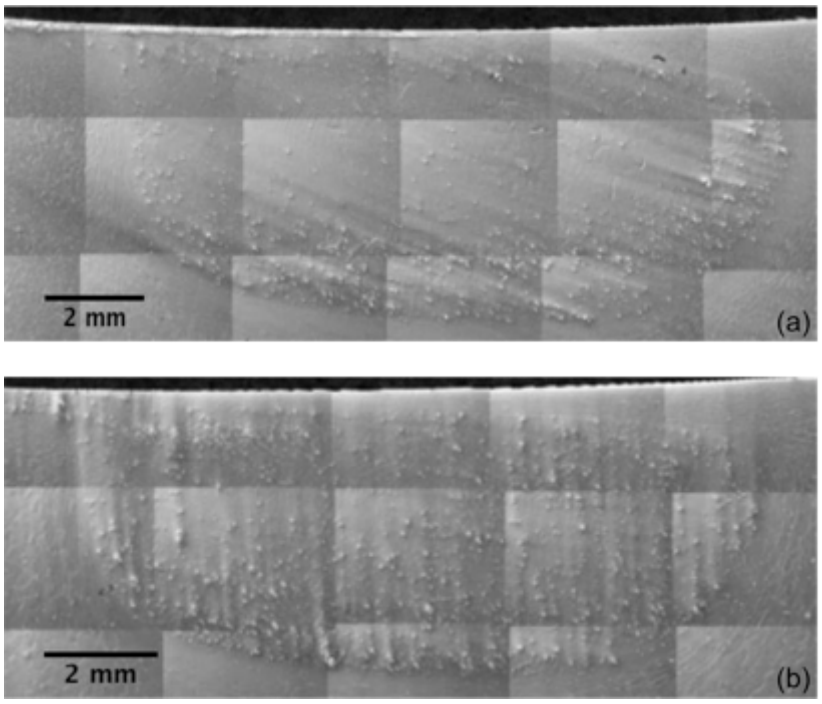

Figure 5: Patterns of SiC particle dispersion in the FSP region – effects of the amount of the SiC particles: (a) 50% cavity filling; (b) 100% cavity filling.

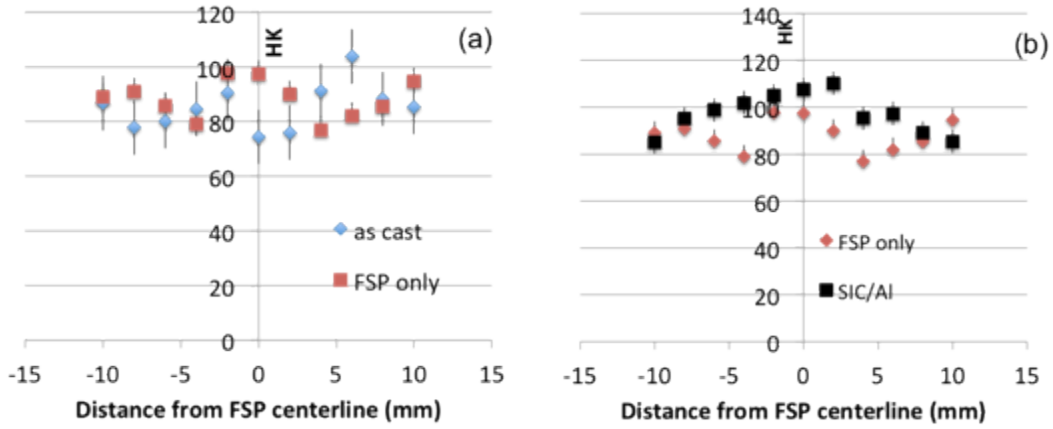

Figure 6: Microhardness profiles of (a) as-cast A206 vs FSPed A206; (b) FSPed A206 vs the SiC/A206 composite.

Fig. 6 shows the Knoop hardness (HK) profiles of the A206 alloy, which experienced different processes, i.e., as-cast, FSP-processed, and nano-SiC particles reinforced and FSP-processed. Data were taken on the transverse cross section of the work piece across the FSP region on a line perpendicular to the centerline of the FSP tool traversing direction. The origin of the x-axis (ordinate) denotes the centerline of the FSP region; negative marks the retreating side, and positive is the advancing side. Each datum point is the average of measurements from several different samples. The data show that the

hardness of as-cast A206 has significant variations at different points. As shown in Fig. 6a, it varies in the range of 75 HK and 105 HK in the measured area and the error bars indicate that even for the same spot the hardness is also very different in different samples. The large harness variation in as-cast A206 can be attributed to its large grain size, coarse Al-Cu precipitations, and casting defects, i.e., porosities. After FSP, the hardness profile becomes a "W" shape across the FSP region and the overall hardness is increased in the FSP nugget. The increase is mainly in the area of about 3 mm each side of the centerline. The improvement of hardness in the FSP nugget can be attributed to the following: (i) grain refinement; (ii) precipitation hardening; (iii) break-up of Al-Cu intermetallic compounds, and (iv) porosity elimination. There was a decrease in hardness at about 4-5 mm each side of the centerline, and this region is considered to be the thermal-mechanical affected zone (TMAZ). Hardness reached a minimum value in the TMAZ, because the microstructure in this region consists of highly elongated and deformed grains, and TMAZ is a precipitate-free zone formed during the FSP thermal cycle. The hardness in the SiC/A206 composite was further improved. The average hardness was 110 HK inside the nugget without the sharp decrease within the HAZ. The increase in the hardness is due to the homogeneous dispersion of the SiC particles.

III: Fabrication using discontinuously reinforced aluminum (DRA)

The purpose of the fabrication was to place discontinuously reinforced aluminum (DRA) into the slot in the A206 alloy substrate. Discontinuously reinforced aluminum is a premade solid composite with a high fraction of reinforcement particles. DRA has a continuous metallic phase, into which a second phase is artificially introduced. The matrix of the DRA applied in this study was aluminum alloy 6061, containing about 50 wt% of Si and SiC particles. Compared to the composite fabricated by mixing in SiC powders, this process has more practical significances in that it is more commonly used and produces better properties.

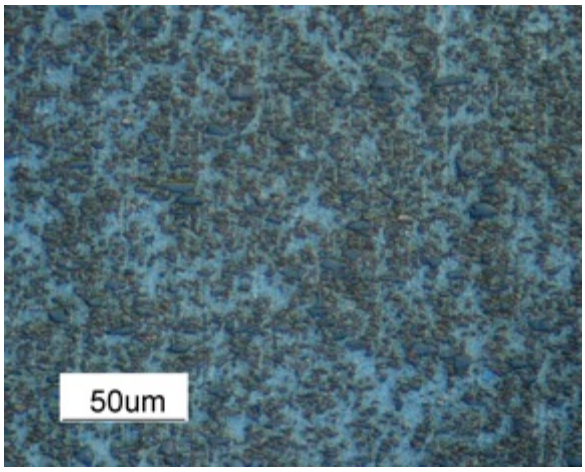

Figure 7: Microstructure of the discontinuously reinforced aluminum (DRA).

Fig. 7 shows the microstructure of the DRA. The size of the Si particle was about 5 μm, the SiC particle was less than 1 μm, and both were distributed in the matrix uniformly. In

fabricating this composite, the DRA material was machined into a rectangular bar (preform) with dimensions of 50 x 1.8 x 3.8 mm. The bar was placed snugly into the slot with dimensions of 50 x 2 x 4 mm, and it left a 0.2 mm gap between the top of the bar and the work piece surface, which ensured the DRA bar was sealed properly by the light pre-friction stirring. The process was successful. Fig. 8 shows the microstructures of the composite at different perspectives and magnifications. Fig. 8a illustrates the interface zone between the composite region and the matrix. It shows that the composite layer and the matrix are well bonded and there are no porosities in this area. Fig. 8b reveals the microstructure inside the composite layer at a higher magnification showing that the particles are uniformly distributed without severe agglomeration. Fig. 8c is a picture that is stitched from several micrographs taken from the longitudinal cross section of the work piece along the centerline of the friction tool forward moving direction. In Fig. 8c one can see that although there is a thin layer where very few particles can be observed in the work piece surface above the composite region, the composite layer and the matrix are well bonded along the length of the DRA bar (5 cm).

The reason for having a particle-depleted surface layer could be that the DRA preform was solid, in which the particles were well bonded with the Al alloy matrix and more difficult to be moved by friction stirring than the SiC powders. Thus, most of the particles tended to be moved around the tool and there was no sufficient movement in the vertical direction. A test verified this hypothesis. In the test the slot had only its bottom half filled with a DRA preform with a height of 2 mm. The microstructure of the composite produced in this test is shown in Fig. 9. It shows that the reinforcement was merely dispersed in the lower part of the FSP region.

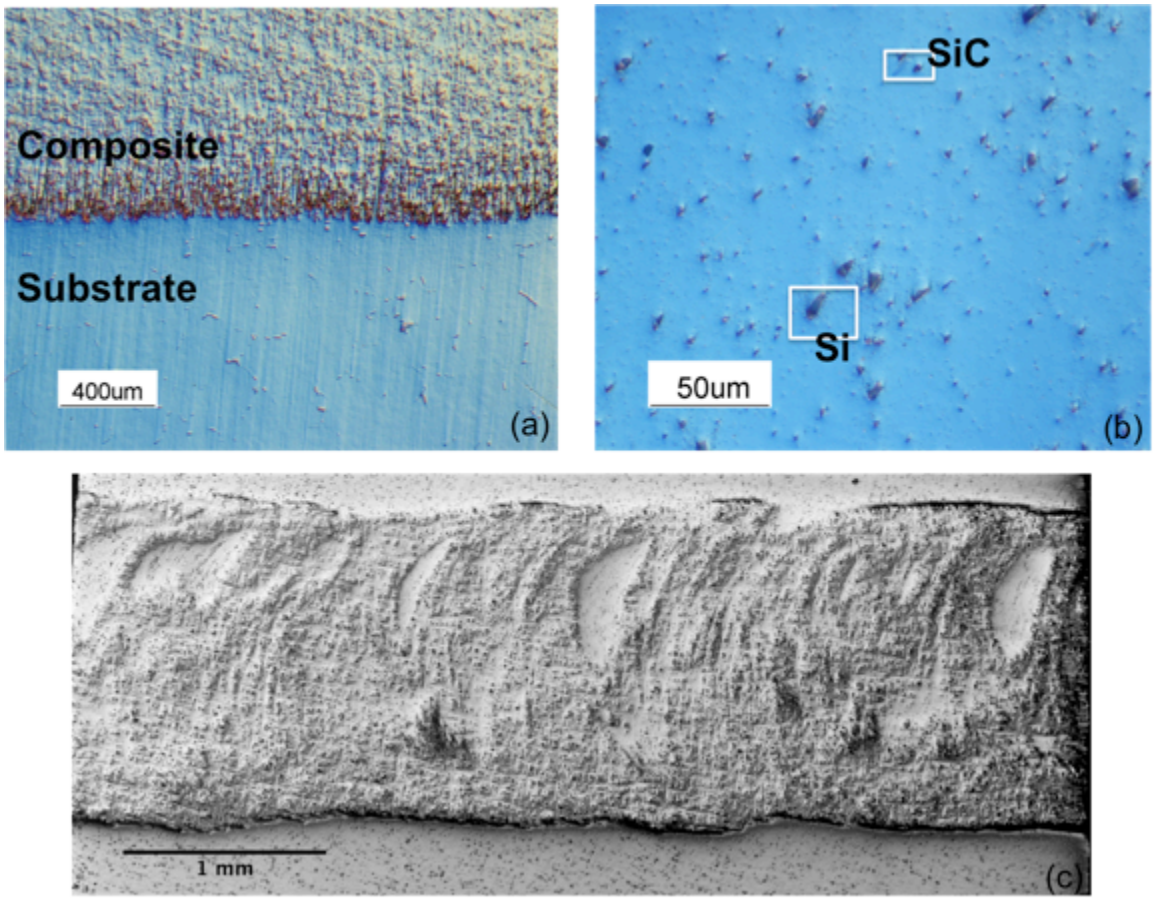

Figure 8: Micrographs of DRA/Al composite: (a) interface area between composite region and the cast A206 matrix; (b) Si and SiC particles inside the composite layer; (c) the lateral view of the whole composite layer.

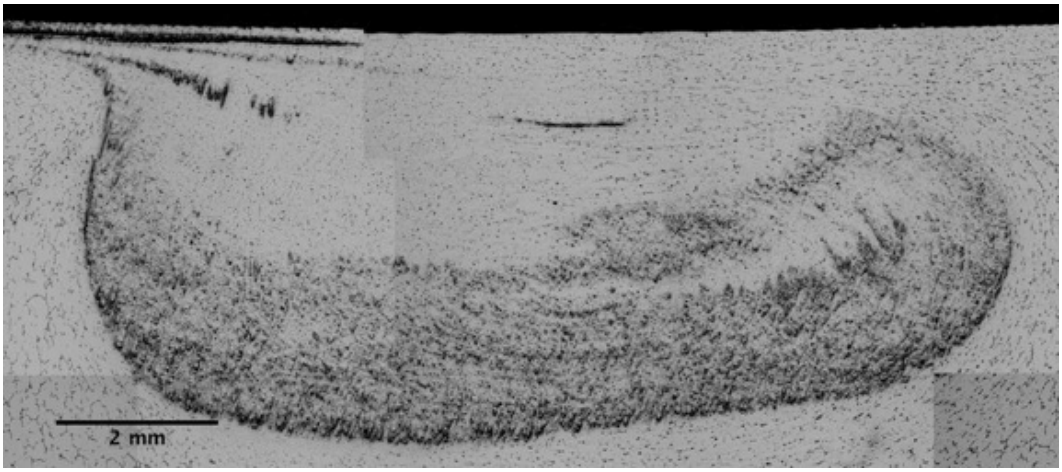

Figure 9: Overview of the composite region fabricated with half-filled slots with a 2 mm high DRA preform.

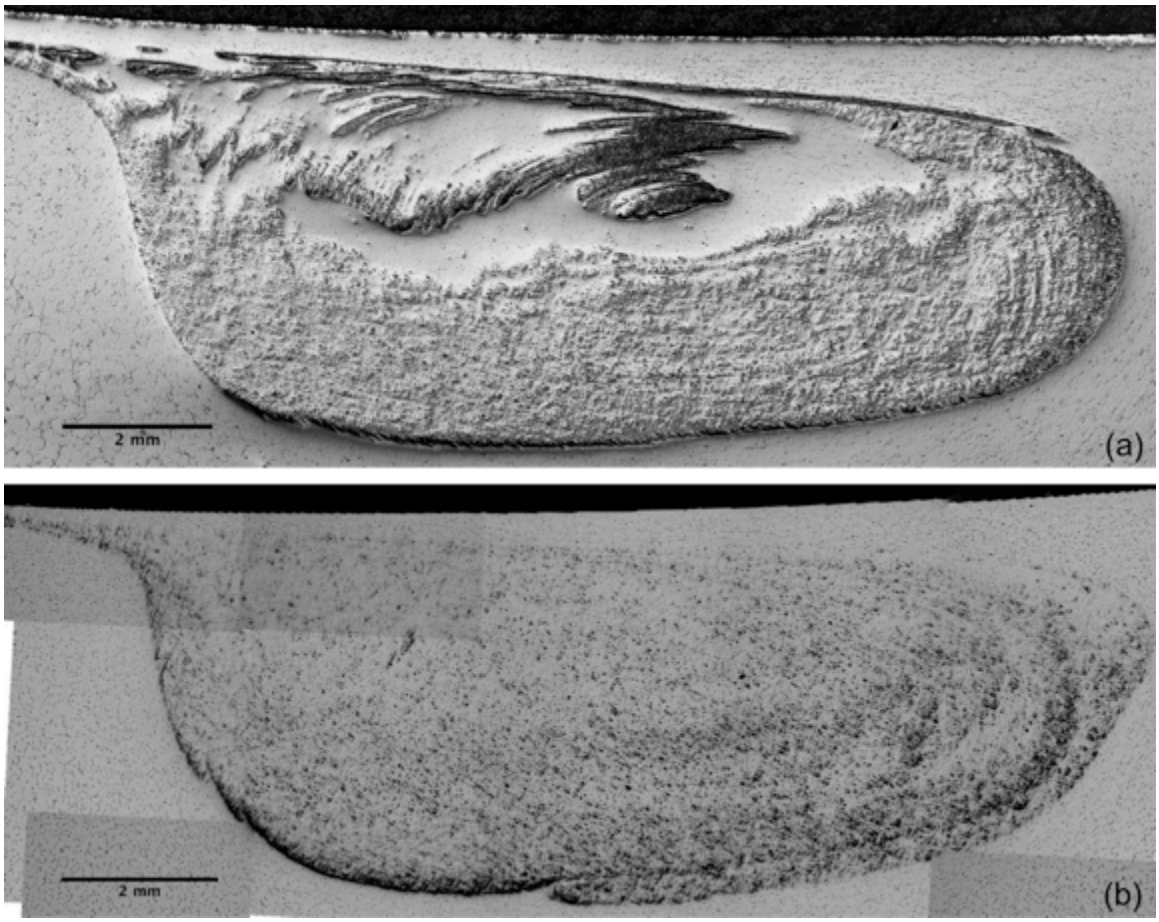

Figure 10: The reinforcement dispersion in the FSP region of the composites fabricated with a different number of stirring passes: (a) one pass; (b) two passes.

The reinforcement dispersion in the composite can be enhanced by increasing the stirring passes. Fig. 10 shows the distributions of the particles in the composites fabricated with a different number of passes. It is evident that the particles were dispersed more homogeneously after a 2-pass than a 1-pass FSP and after two passes the particle agglomerations disappeared in the middle of the FSP region.

The hardness tests showed that the composite fabricated with DRA was much harder than the work piece that was only processed by FSP (see Fig. 11). The composite fabricated with DRA had an average hardness of 125 KH in its composite region, which was higher than that of the composite made with the SiC powder. The higher hardness was due to the fact that using DRA can incorporate more reinforcement particles in the Al alloy matrix than using other methods. In addition, the particles were dispersed more uniformly in the DRA composite as shown in Fig. 10b, in which the reinforcement was distributed almost evenly in both the retreating and the advancing sides, and so the DRA composite had no lower hardness zone as in the TMAZ in the composite fabricated using FSP only.

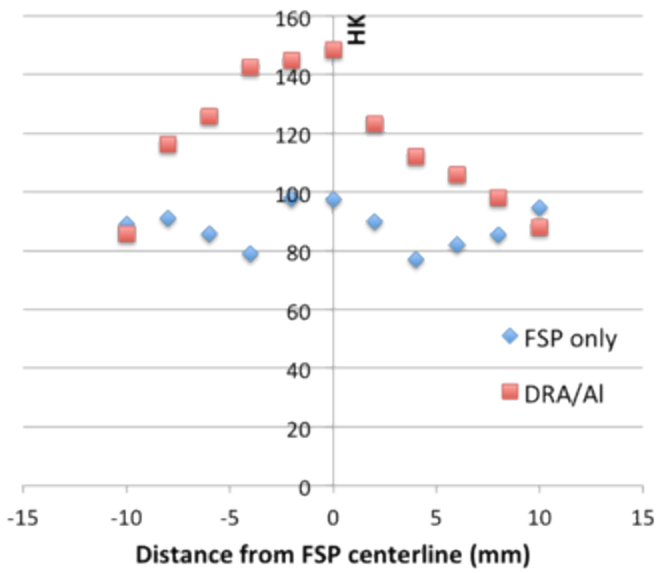

Figure 11: Microhardness of the composite layer made with DRA and the microhardness of the FSP region in the work piece processed by FSP only without reinforcement.

FSP is also an effective way to achieve grain refinement [22]. The study's tests show that, when FSP is used for fabricating particulate reinforced composites, grain refinement becomes more effective. Fig. 12 shows two micrographs of the DRA/A206 composite taken at the same location. Fig. 12a is an unetched microstructure; it shows the distributions of the reinforcement particles in the matrix and that the particles dispersed in the matrix are the micro-sized Si and submicro-sized SiC. Fig. 12b is the etched microstructure showing the grain structure. The grain size was about 3 μm, which was much smaller than those in the FSPed A206 without adding DRA and any other particles. Generally, the grain size of FSPed A206 is in the range of 6-7 μm. The strengthened capability of FSP for grain refinement in making composites is attributed to the pinning effect of particles. The mechanism of grain refinement by FSP is dynamic recrystallization. With uniformly dispersed reinforcement, especially the nano-sized SiC particles, much smaller-sized grains can be achieved because the particles act as barriers, which slow down or block the atomic movement and limit the grain growth in the recrystallization.

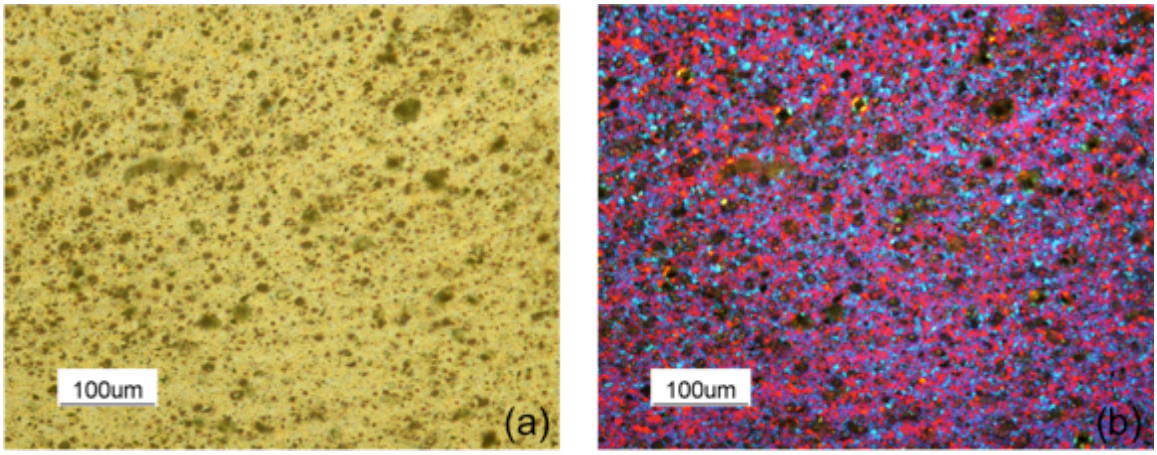

Figure 12: Microstructure of the Al-DRA composite at the same location: (a) unetched showing reinforcement particles in the Al matrix; (b) etched showing grain structure.

Summary

FSP has emerged as an advanced post-processing technique to produce surface or localized composites and synthesize the second phases into the Al matrix in the solid state. The feasibility of applying this technique in fabricating localized composites was investigated in this study. It used different kinds and conditions of reinforcement particulates, which were nano-sized Ta powders, nano-sized SiC powders, and discontinuously SiC reinforced aluminum in the cast aluminum A206 matrix. The composites produced at all tested conditions were characterized and evaluated. The results demonstrate the successes of this technique.

In the composite fabricated using nano Ta particles the particles were distributed uniformly. The uniform distribution is attributed to the following: (i) sufficient material movement, (ii) encapsulation of reinforcement, and (iii) sufficient contact between the reinforcement and the tool. The study also showed that dispersion of the powders could be further improved by multi-pass FSP.

In fabricating composites with SiC powder via FSP, the effects of the amount of powder addition on the particle distribution and property (hardness) were studied. In the fabrication, the SiC powder was packed in a machined slot; the composite produced with the slot fully filled with SiC powder had a much better particle dispersion than that made with the slot half filled. The former was also harder than the latter. The composites produced with the slot either fully or half filled were harder than the alloy that was only FSPed and had no hardness decrease zone. The alloy that was FSPed only had a TMAZ of lower hardness.

Fabricating composites using DRA indicated that the particle dispersion was affected by the location of the DRA preform and number of the stirring passes. The DRA preform was solid, in which the particles were well bonded with the Al alloy matrix and more difficult to be moved by friction stirring than the SiC powders. Thus, most of the particles

tended to be moved around the tool, and there was insufficient movement in the vertical direction. So, when the slot was only partially filled, the particles were also dispersed in part of the FSP region. Therefore, in order to make a good composite region with DRA, the location where the DRA preform is embedded is critical. The particle dispersion can also be improved by multi-pass friction stirring. For example, two passes of stirring can make the particle distribution much more uniform than one pass. The composite made with DRA was harder than that made with the SiC powder. This is due to the fact that using DRA can incorporate more particles in the Al alloy matrix than using other methods. In addition, reasons for the increasing hardness could also be the more uniformly distributed reinforcement particles and the much finer grain size. The fine grains are attributed to the pinning effect of the particles. The uniformly dispersed particles can act as barriers, which slow down or block the atomic movement and limit the grain growth in the recrystallization, promoting the evolution of the microstructure.

References

[1] S. Scudino, G. Liu, M. Sakaliyska, K.B. Surreddi, and J. Eckert, "Powdermetallurgy of Al-based metal matrix composites reinforced with β-Al_3Mg_2 intermetallic particles: Analysis and modeling of mechanical properties", Acta Materialia, Vol. 57, pp 4529-4538. (2009)

[2] R.A. Saravanan and M.K. Surappa, "Fabrication and characterization of pure magnesium-30 vol.% SiC_P particle composite", Materials Science and Engineering A, vol. 276, pp. 108–116. (2000)

[3] L. Hu and E. Wang, "Fabrication and mechanical properties of SiCw/ZK51A magnesium matrix composite by two-step squeeze casting", Materials Science and Engineering A, vol. 278, pp. 267–271. (2000)

[4] X. Li, Y. Yang and X. Cheng, "Ultrasonic-assisted fabrication of metal matrix nanocomposites", Journal of Materials Science, vol. 39, No. 9, pp. 3211-3212. (2004)

[5] W.M. Thomas, E.D. Nicholas, J.C. Needham, M.G. Murch, P. Templesmith, C.J. Dawes, GB Patent Application No. 9125978.8, December 1991.

[6] R.S. Mishra, Z.Y. Ma and I. Charit, "Friction stir processing: a novel technique for fabrication of surface composite", Materials Science and Engineering A, vol. 341, pp. 307-310. (2003)

[7] D.K. Lim, T. Shibayanagi and A.P. Gerlicha, "Synthesis of multiwalled CNT reinforced aluminum alloy composite via friction stir processing", Materials Science and Engineering A, vol. 507, pp. 194–199. (2009)

[8] M. Yang, C. Xu, C. Wu, K. Lin, Y. Chao and L. An, "Fabrication of AA6061/Al_2O_3 nano ceramic particle reinforced composite coating by using friction stir processing", Journal of Materials Science, vol. 45, No.16, pp. 4431–4438. (2010)

[9] B. Zahmatkesh and M.H. Enayati, “A novel approach for development of surface nanocomposite by friction stir processing”, Materials Science and Engineering A, vol. 527, pp. 6734-6740. (2010)

[10] W. Wang, Q. Shi, P. Liu, H. Li and T. Li, “A novel way to produce bulk SiCp reinforced aluminum metal matrix composites by friction stir processing”, Joural of Materials Processing Technology, vol. 209, pp. 2099–2103. (2009)

[11] M. Dixit, W.J. Newkirk and R.S. Mishra, “Properties of friction stir-processed Al 1100–NiTi composite”, Scripta Materialia, vol. 56, pp. 541–544. (2007)

[12] C.J. Lee, J.C. Huang and P.J. Hsieh, “Mg based nano-composites fabricated by friction stir processing”, Scripta Materialia, vol. 54, pp. 1415-1420. (2006)

[13] L.B. Johannes, L.L. Yowell, E. Sosa, S. Arepalli and R.S. Mishra, “Survivability of single-walled carbon nanotubes during friction stir processing”, Nanotechnology, vol. 17 pp. 3081-3084. (2006)

[14] L, Ke, C. Huang, L. Xing and K. Huang, “Al–Ni intermetallic composites produced in situ by friction stir processing”, Journal of Alloys and Compounds, vol. 503, pp. 494–499. (2010)

[15] C.J. Hsu, P.W. Kao and N.J. Ho, “Ultrafine-grained Al–Al2Cu composite produced in situ by friction stir processing”, Scripta materialia, vol. 53, pp. 341–345. (2005)

[16] C.J. Hsu, C.Y. Chang, P.W. Kao, N.J. Ho and C.P. Chang, “Al–Al_3Ti nanocomposites produced in situ by friction stir processing”, Acta Materialia, vol. 54, pp. 5241–5249. (2006)

[17] H. Schmidt, J. Hattel, and J. Wert, “An analytical model for the heat generation in friction stir welding”, Modelling and simulation in Materials Science and Engineering, vol. 12, pp. 143-157. (2004)

[18] A.P. Reynolds, “Visualization of material flow in autogenous friction stir welds”, Science and Technology of Welding and Joining, vol. 5, pp. 120-124. (2000)

[19] T.U. Seidel, and A.P. Reynolds, “Visualization of the material flow in AA2195 friction stir welds using a marker insert technique”, Metallurgical and Materials Transactions A, col. 32, pp. 2879-2884. (2001)

[20] W.J. Arbegast, “Modeling friction stir joining as a metal working process”, Hot Deformation of aluminum alloys, Z.Jin, Edited, TMS. (2003)

[21] W. Tang, X.Guo, J.C. McClure, L.E. Murr, and A. Nunes, “Heat input and temperature distribution in friction stir welding”, Journal of Materials Processing and Manufacturing Science, vol. 7, pp. 163-172. (1998)

[22] T.R. McNelley, S. Swaminathan and J.Q. Su., “Recrystallization mechanisms during friction stir welding/processing of aluminum alloys” , Scripta Materialia, vol. 58, pp. 349–354. (2008)

Appendix A: High Tech Die Casting, Vicenza, Italy,
Accepted by La Metallurgia Italiana

Localized Microstructure Enhancement via Friction Stir Processing for Die Cast Components

N. Sun and D. Apelian
Advanced Casting Research Center
Metal Processing Institute
WPI, Worcester, MA 01609 USA

ABSTRACT

Friction stir processing (FSP) is an outgrowth of Friction stir welding (FSW) that locally manipulates the microstructure by imparting a high level of energy in the solid state resulting in improved mechanical properties. This study has shown that FSP can be implemented as a post-casting method to locally eliminate casting defects, such as porosity, which is generated by gas evolution during casting. Coarse second phases are broken into fine nearly equiaxed particles and uniformly distributed in the matrix. Moreover, grain refinement is obtained by dynamic recrystallization during FSP. This results in improved microhardness, tensile properties and fatigue properties of the cast FSP processed A206 alloy. In addition, FSP is a viable means to produce localized composite structures in cast Al components. Such improvements have important implications for manufactured components for a variety of automotive and other industrial applications. The convenience of FSP as a post-processing step that can easily be adapted during machining operation makes it very attractive to adopt. These results will be reviewed and discussed.

KEYWORDS

FSP, Microstructural Manipulation, Microhardness, Tensile Properties, Fatigue properties, Composite Fabrication

INTRODUCTION

Complexities of casting, which involve heat, fluid and mass transport processes, give rise to heterogeneities of the microstructure, formation of porosity, and defects. These flaws deteriorate materials properties and limit casting applications. In a sense, it can be considered that high-quality castings are made not only by controlling the microstructure, but also more importantly through control (or management) of defects. In this vein, a processing method, Friction Stir Processing (FSP), has been pursued to locally control or affect the microstructure, and to reduce porosities and defects to improve cast properties. FSP was developed based on the principle of Friction Stir Welding (FSW) [1]. In FSP a

high-speed rotating tool (rod) with a flat shoulder and probe penetrates into and traverses across the work piece, while the head face of the tool shoulder fully contacts the work piece. Frictional heat (between the tool and the work piece) can be high enough to produce plastic deformation of the matrix around the moving tool; this alters and refines the local microstructure, reduces porosity and defects, which results in local property improvement.

FSP has emerged as an important post-processing technique and has drawn much attention. It was first used in highly alloyed wrought Al alloys such as the 2XXX and 7XXX series for aerospace applications; superplasticity, high strength, and fracture resistance of the alloy were attained via FSP [2-4]. A unique characteristic of FSP is the resultant ultrafine grain structure and simultaneous improvements in the strength and ductility of the processed alloy [5]. This phenomenon is contrary to the Hall-Patch Law, wherein fine grains result in grain boundary strengthening [6] at the expense of ductility [7]. This implies that FSP has a different strengthening mechanism. Several factors can account for the property improvements we see in the FSPed region, such as grain size and grain morphology, distribution and density of dislocations, and grain boundary morphology. Friction stir processed microstructures have the following features [8]: (i) equiaxed, fine grains – even ultra-fine grains (nano-sized scale) [9-11], (ii) very fine second phases and (iii) large fraction of high-angle grain boundaries. These microstructural features enable superplastic deformation at high strain rates and/or low temperatures [12-14] as well as improved room-temperature formability [15].

Another attractive feature of FSP is that it can be incorporated in the overall manufacturing cycle as a post-processing step during the machining operation to achieve a localized composite structure in the cast component. Secondly, porosity that is generated by gas evolution, as well as undesirable interfacial reactions between the reinforcement phase and the matrix are mitigated via FSP[16]. Third, FSP can be used as a tool for the repair of localized defects.

In this study FSP was performed on cast A206 aluminum alloy. A206 is an important and widely used Al casting alloy because of its high strength and good machinability. FSP parameters were optimized for this alloy to locally manipulate the cast microstructure - porosity alleviation, grain refinement, and second phase homogenization. This study also evaluated the resultant mechanical properties, both static and dynamic. For composite fabrication via FSP, the reinforcements were emplaced in the pre-machined cavity in the Al A206 work piece. Three reinforcement materials and several key processing parameters were investigated. The motive behind this study was to confirm and demonstrate FSP as an enabling technology for post-processing of cast A206 components. By doing so, the cast structure can be locally manipulated to attain wrought material attributes; this opens up the design space of cast Al alloys towards that for wrought Al alloys.

DESIGN OF EXPERIMENTS

The main platform for FSP was a HAAS CNC milling machine. A specifically designed

FSP tool head made from H13 tool steel was used. The diameter of the tool shoulder is 16 mm, and at the end of the shoulder a tapered probe whose length is 3.2 mm is manufactured. A tilt angle (angle between machine spindle and work piece normal) of three degrees is used to induce the forging action at the trailing edge of the shoulder. This is achieved by inserting a back plate whose surface is machined into a slant surface. Proper tool penetration depth is very important in generating enough friction heat between the tool and the work piece and producing good FSP finish on the work piece. The minimum tool penetration depth requires the shoulder of the tool to have enough contact with the work piece, and this number is calculated based on the real contact condition between the tool and the material. The local temperature of the work piece was measured by K-type thermocouples and the data was recorded by the FLIR S40 system. Four equi-distant holes were drilled along the FSP traverse direction to accommodate four thermocouples, and the distance between each thermocouple was 2.54 cm. These thermocouples were inserted into the work piece at 2 mm below the top surface, and the tip of each thermocouple was near the centerline of the FSP nugget.

Table 1. Composition of the Commercial A206 Alloy

Si	**Fe**	**Cu**	**Mn**	**Mg**	**Zn**	**Ti**	**Ni**
0.077	0.046	4.33	0.343	0.256	0.019	0.243	<0.002

Eck Industries provided 6.25mm thick commercial A206 plates. The composition of the alloy is shown in Table 1. Dimensions of the work piece are 150 mm X 75 mm X 6.25 mm. FSP was directly applied on the casting surface, and the processing parameters were as follows: tool rotation speed –1000 RPM, tool traverse speed – 50.8 mm/min.

Samples for metallographic analysis were sectioned perpendicular to the FSP traverse direction and prepared for the microstructure analysis following the routine procedure. Barker's etchant and the polarized light were used to clearly reveal the grain size and morphology. Thin films for the TEM analysis was prepared via the focus ion beam (FIB) technique at particular locations in the processed region. TEM work was carried out with a JOEL 2000 microscope operated at 200 kV. Specimen preparation for the EBSD analysis was carefully performed in order to properly image the structure and obtain high-quality diffraction patterns. A Carl Zeiss SUPRA-55 SEM equipped with the EBSD detector was used for EBSD data acquisition. The step size chosen for the FSPed specimen was 0.5 μm, and for the as-cast specimen was 5 μm.
The Knoop hardness (HK) test was conducted using the Buehler OmniMet MHT automatic microhardness test system with a load of 500 gf. As shown in Fig. 1, the test specimens were sectioned perpendicular to the FSP traverse direction to reveal the transverse cross-section. Measurements were taken on the transverse cross-section along two lines. The first line is ~ 300 μm below the top surface of the FSP region, and the second line is the middle line of the FSP region. They are named as location 1 (L1) and location 2 (L2) respectively in the results and discussion section.

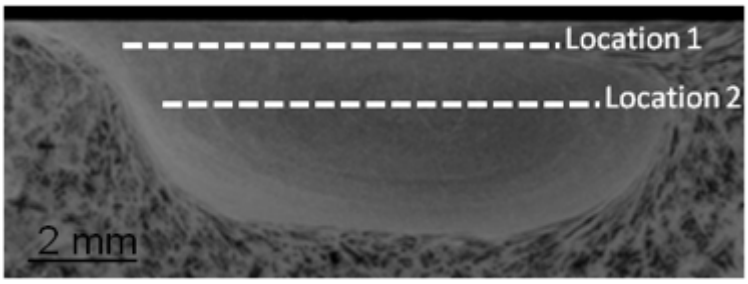

Fig. 1: A macrograph of the FSPed region showing two locations where the microhardness data were collected.

The tensile test specimen was taken from the FSP nugget (the homogenous microstructure region) along the FSP traversing centerline as shown in Fig. 2. The specimen had a 25 mm gauge length with a cross section of 12.5 x 6.3 mm. It is a standard specimen in accordance to ASTM B8. The test was conducted in the Instron machine 5500 at room temperature. The ramp rate was set at 1 mm/min (strain rate of 4%) and the strain was measured using an extensometer of 25 mm gauge length.

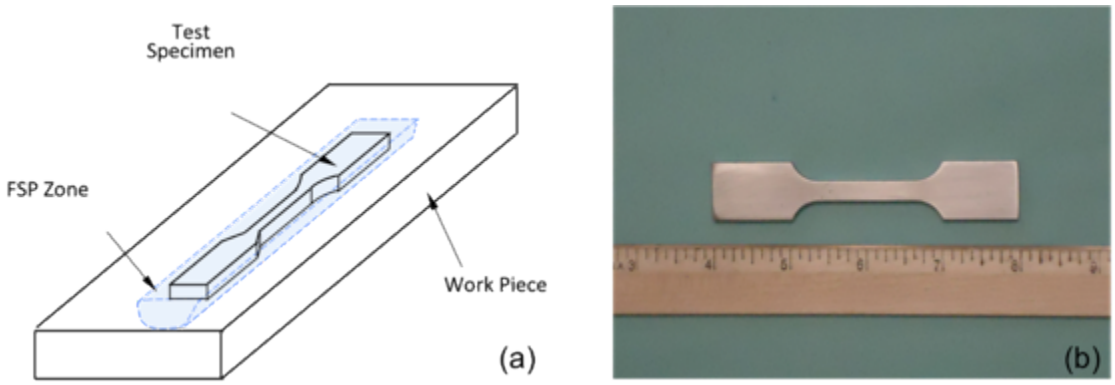

Fig.2: Specimen for the tensile test: (a) schematic diagram of the tensile bar; (b) image of the tensile bar.

The ultrasonic fatigue tests were conducted at room temperature in the ambient air over a range of stresses using fully reversed load (R= -1). Figure 3 shows the ultrasonic fatigue test apparatus and the geometry of the ultrasonic fatigue test specimen. The specimen had cylindrical gauge sections, and it was turned from a rectangular bar; dimensions of the bar were 15 (L) x 1.4 (W) x 1.4 (H) cm. For the FSPed specimen, the gauge section was manufactured from the FSP nugget to ensure the homogeneity of the microstructure in this region. To ensure a consistent surface finish with low residual stress, samples were polished along the longitudinal direction to reach a Ra 8 value; these were done at Westmoreland Materials Testing.

The following three reinforcement materials to fabricate the composite layers were used: (i) 20 nm Ta powders; (ii) 100 nm SiC powders; and (iii) discontinuously reinforced

aluminium (DRA). The reinforcements were emplaced into a slot that was manufactured in the surface of the work piece. The dimensions of the cavity were 50 (L) X 2 (W) X 4 (T) mm. Prior to FSP, the top of the slot was covered and sealed by the pre-friction-stirring action using a probe of only one millimetre in length to ensure the reinforcements (powders) were well encapsulated. The centerline of the slot was 1 mm offset from the centerline of the tool-traversing route to make sure that the advancing side of the tool fully contacted the reinforced materials. FSP was carried out at a tool rotating speed 1000 RPM and traversing speed 50 mm/min. Effects of multi-pass-FSP (up to two passes) and the amount of the reinforcement material were investigated. Samples were sectioned perpendicular to the FSP traverse direction; SEM and EDS were applied to reveal distributions of the reinforcement materials.

RESULTS AND DISCUSSIONS

Microstructure Evolution

Fig. 3a is a composite image showing the morphology and distribution of microshrinkage porosities inside the as-cast A206 specimen. To quantitatively analyze the 2-D porosity population distribution, a large area (7 mm x 5 mm) metallographic cross-section was examined to ensure a sufficient number of pores were in the analysis space. Sizes and distributions of all porosities were statistically analyzed with an image processing software. The size of the porosity was characterized with the equivalent circular diameter (ECD), which is defined as

$$D = 2 \times \sqrt{\frac{A}{\pi}} \tag{1}$$

where A is the 2-D projected area of the porosity.

For the as-cast A206, the average porosity ECD was 37 μm, and the total area fraction of the microshrinkage porosity was 0.65%. Fig. 3b is the ECD frequency distribution histogram. More than 80% of ECDs were between 20 μm and 50 μm. After FSP, more than 97% of the pores were closed down due to plastic deformation of the material under the high downward force and shear forces. This indicates that FSP is a viable method to significantly reduce porosity in the component.

Fig. 4 shows optical micrographs of A206 pre-and post-FSP. Grain boundaries and grain size are clearly depicted in Fig. 4a and Fig. 4b. Dendritic structures and large grains more than 400 μm in diameter are observed in the as-cast A206 microstructure. However, after FSP, equiaxed and fine grains in the size of less than 10 μm were observed, almost a reduction of one magnitude order. In addition, there was second phase compound refinement. The microstructure of the as-cast A206 contained second phases that were mainly coarse needle-like $CuAl_2$-CuAl compounds (Fig. 4c). In contrast, in the FSP region fine second phase particles uniformly distributed were observed (Fig. 4d). These small particles were $CuAl_2$-CuAl compounds broken by the stirring action of the probe, and the aspect ratio of the refined particle was near one.

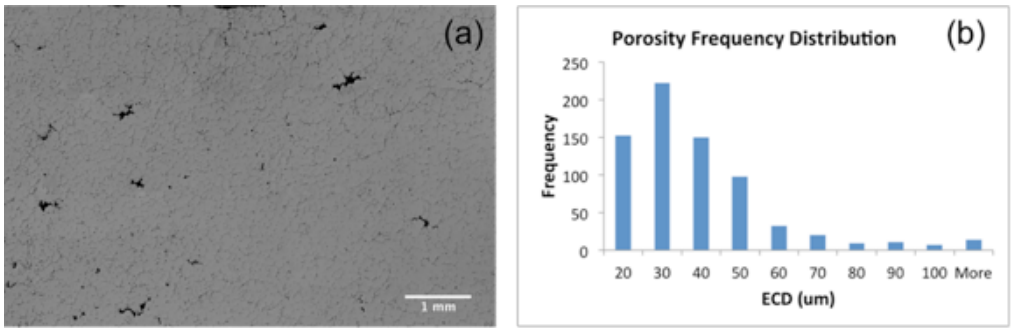

Fig. 3: Casting defect analysis: (a) the distribution of porosity inside a large area of the as-cast A206; (b) a plot showing the frequency distribution of the porosities equivalent circular diameters.

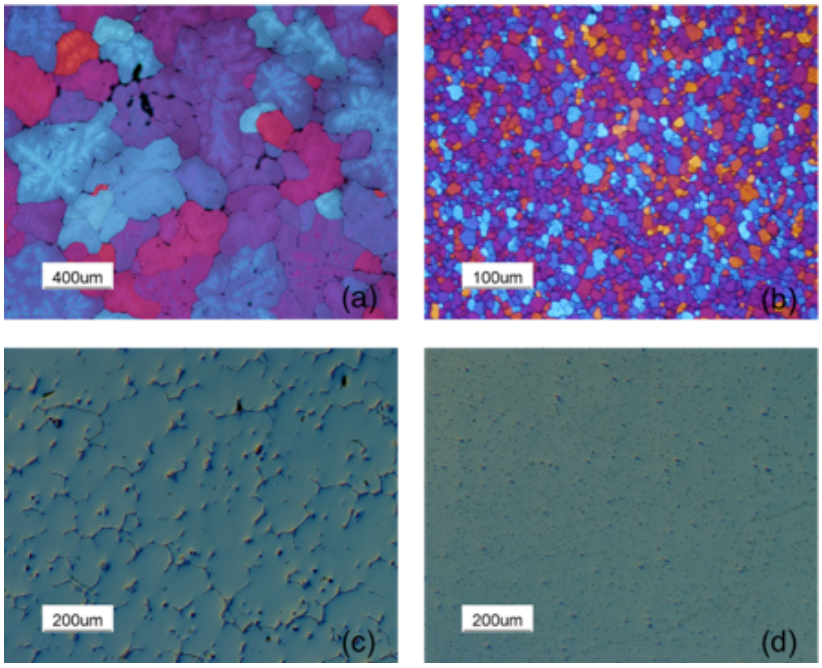

Fig. 4: Micrographs of as-cast A206 and FSP A206 (a) grain morphology of as-cast A206; (b) grain morphology of FSP A206; (c) second phase distribution of as-cast A206; (d) second phase distribution of FSP A206.

Grain boundary characteristics were analyzed via EBSD. Fig. 5a and Fig. 5c are image quality (IQ) maps taken from the as-cast A206 and FSPed A206 samples. The IQ map is overlaid with grain boundary angles. The “high angle” boundaries are defined as boundaries with misorientations exceeding 15 degrees, whereas the “low angle” boundaries are defined as boundaries with misorientations between 1 degree and 15 degrees. High-angle grain boundaries are marked in blue color. When quantitatively analyzing the grain boundary characteristics, for instance, calculating the fraction of high-angle boundaries, the minimum boundary misorientation should be defined. In this case, the minimum boundary misorientation was set to 1. Fig. 7b and Fig. 7d are

histograms showing the frequency distribution of grain boundary misorientation angles in the as-cast and FSPed specimen. The fraction of high angle grain boundaries increased from 26.6 % to 76.7% after FSP.

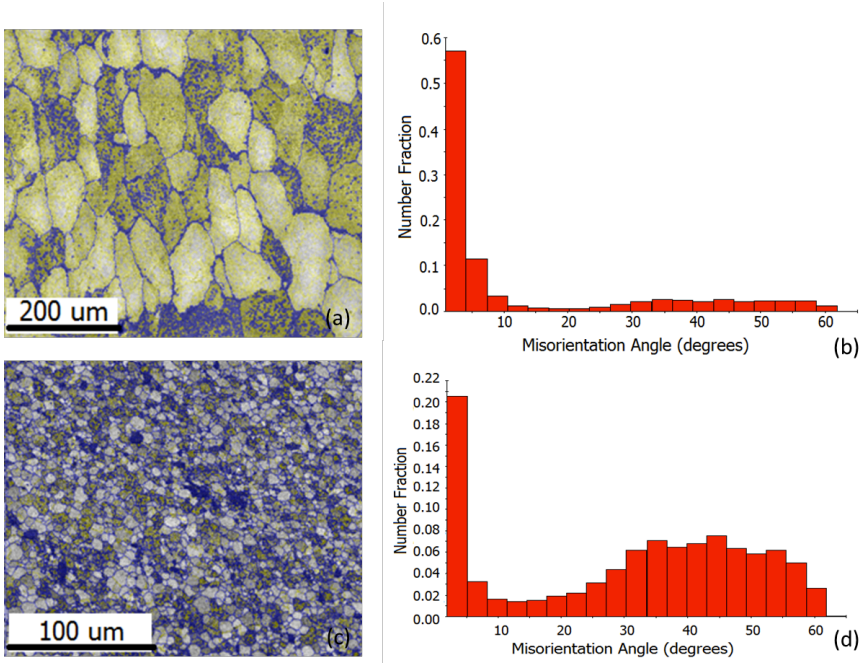

Fig. 5: Image quality maps overlaid with low angle and high angle boundaries and misorientation angle distribution histogram plots of the as-cast A206 (a) (b) and FSPed A206 (c) (d).

FSP introduces a large amount of dislocations in the work piece. The rearrangement or elimination of these dislocations reduces the internal energy of the system; this is the thermodynamic driving force for dynamic recovery. During dynamic recovery, subgrains or cell structures are formed by dislocation rearrangement and accumulation, and these substructures can only be revealed under TEM because they do not have typical grain boundaries that can be clearly demarked with optical microscopy. Moreover, because there is no migration of high angle boundaries, most subgrains are formed with low angle boundaries. Contrary to dynamic recovery, there is large scale high-angle grain boundary migration during dynamic recrystallization, and if grain refinement is caused via dynamic recrystallization, boundaries of the refined grains can be clearly delineated by both optical microscopy and TEM. This study found that the grain refinement via FSP was mainly due to dynamic recrystallization, as we have observed clear grain boundaries (Fig. 4b and Fig. 6a) as well as a high fraction of high angle boundaries. However, as shown in Fig. 6b, some dislocation tangles and cell structures remain inside the refined grain, which indicates that dynamic recovery did take place during FSP. Due to the high stacking fault energy of the aluminum, dislocations can interact with each other easily during the recovery stage, which led to dislocations annihilation. Especially for low-angle grain boundaries, they are sinks of dislocations and they can promote the recovery and reduce the dislocation density [17]. FSP produced a large fraction of high-angle

boundaries and the remained dislocation density was higher in the FSPed work piece compared with in the as-cast work piece.

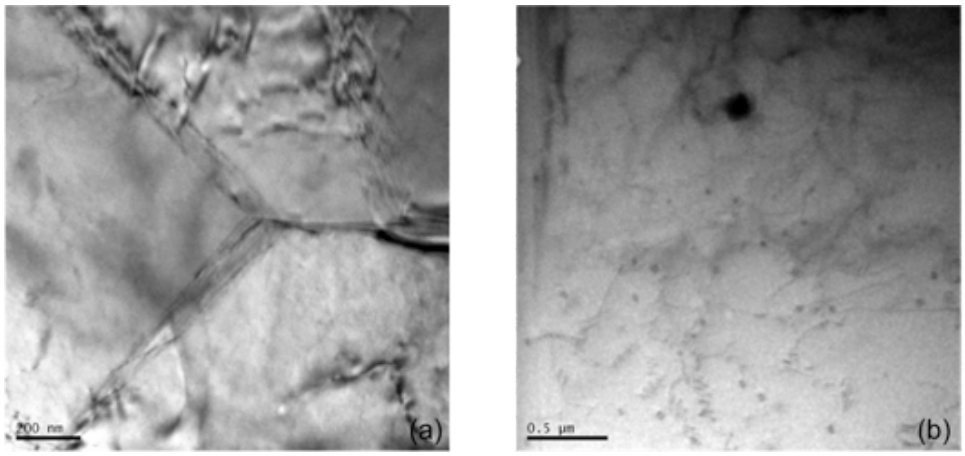

Fig. 6: TEM micrographs showing (a) grain morphology showing clear boundaries; (b) dislocations inside a grain.

Mechanical Properties Enhancement

Fig. 7 shows the average Knoop hardness (HK) profiles for the as-cast and FSPed A206 specimens. The average microhardness of the as-cast A206 was 85 HK, and one can note the variation in values (see the error bar of the as-cast data in Fig. 8 b). The existence of casting defects, i.e. porosities and inclusions, deteriorated the hardness of the material. The microhardness profiles of the FSP processed specimen were selected from two locations in the FSP region, as described in the previous paragraph. The material between the surface of the work piece and location 1 had sufficient contact with the tool shoulder, and this region is referred to as the shoulder-affected zone. During FSP, the material in the shoulder-affected zone experienced a huge downward force as well as a shear force from the tool shoulder. The strain/strain rate in this region was higher than in other parts of the FSP region. As a result, the stirring action of the tool broke those coarse Al-Cu intermetallic compounds and produced fine Al-Cu particles whose sizes were smaller in the shoulder-affected zone than in other regions. These finer Al-Cu particles generated a stronger pinning effect to prevent the coarsening of the recrystallized grains. From Fig. 8a one can see that the grain size at location 1 was smaller than that in the middle of the FSP region. Location 2 was in the middle of the FSP nugget, and the material in this region represented the typical microstructure of the FSPed A206. Microhardness profiles in the shoulder-affected zone (location 1) as well as in the middle of the FSP zone (location 2) were higher in values than the microhardness profile in the parent material. Moreover, the material in the shoulder-affected zone became even harder. The improvement in microhardness is contributed to the following: (1) grain refinement – dynamic recrystallization occurred during FSP, which resulted in an obvious grain size decrease (from ~300 μm to 5 μm at location one, and down to 10 μm at location two); based on the Hall – Petch principle, material strengthening can be achieved via grain refinement, and this was the reason that location has a higher hardness value than

location two; (2) casting defect alleviation – FSP eliminated almost all porosity; (3) second phases break-up during FSP; fine and homogenously dispersed second phase particles result in a uniform hardness distribution in the FSP region.

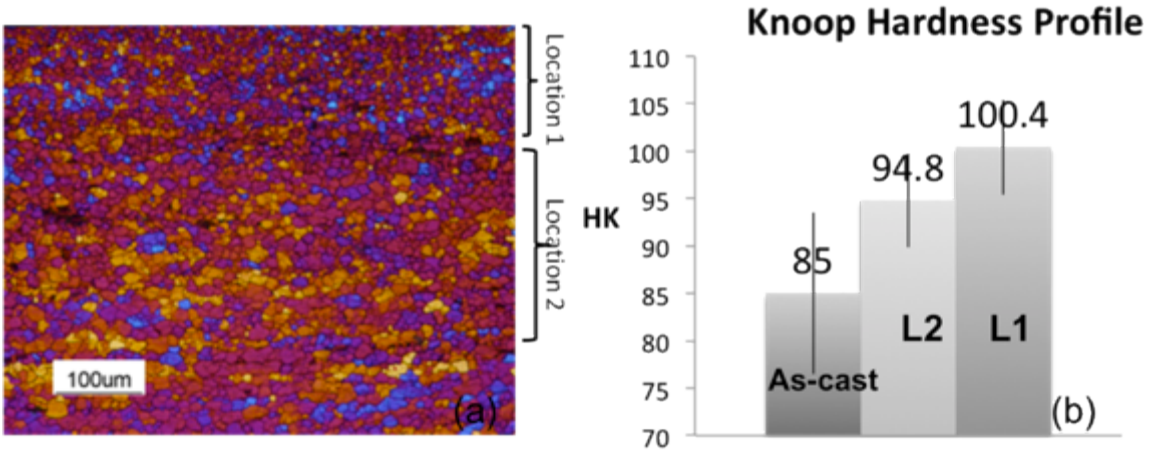

Fig. 7: Microhardness profile of the as-cast A206 and FSP A206: (a) grain size difference in the FSP region; (b) microhardness values.

Fig. 8 shows typical stress-strain curves of as-cast A206 and FSPed A206. The yield stress of the as-received A206 was 190 MPa; the UTS was 262 MPa, and the elongation was 5.6%. FSP resulted in a simultaneous increase in the strength and ductility. The elongation increased to 14.4%. Both the yield stress and the UTS increased after FSP: the yield stress increased from 190 MPa to 230 MPa, and the UTS increased from 262 MPa to 348 MPa. In this case, a numerical index that only depends on the metallurgical qualities of the alloys [18] was introduced to express the quality of a casting. A higher index number stands for the better quality of a casting or the better tensile property of a specimen. The quality index (QI) can be calculated based on the following equations [18]

$$QI = UTS + k \times \log E \tag{2}$$

where UTS is the ultimate tensile strength in MPa; k is a constant whose value is 150 for the aluminum alloy; E is the elongation. Because the yield strength (YS) is less influenced by casting defects, we used the yield strength to calculate the QI instead of UTS. The YS is given by

$$YS = UTS - 60 \times logE - 13 \tag{3}$$

Accordingly, the quality index can be expressed as

$$QI = YS + 210 \times logE + 13 \tag{4}$$

The FSPed specimen showed better tensile properties with the QI increasing from 360 to 486. The enhanced yield stress was attributed to the dislocation pinning effect. FSP introduced a large number of dislocations in the work piece. Although the dislocation density was lowered by dislocation annihilation during the recovery stage, there were still

many dislocations preserved within the refined grains or at grain boundaries. At grain boundaries, the dislocations accumulated and interacted with one another, which served as pinning points or obstacles that significantly impeded their motion under loading as exhibited in the tensile test. Moreover, those fine and uniformly dispersed second phase particles interacted with the tangled dislocations, which further prohibited dislocation movement and strengthened the material during low strain deformation. This resulted in the observed higher yield strength. The increased UTS was due to porosity elimination as well as refinement of grains and second phases. Ductility improved after FSP – the elongation was increased by more than 150%. The significant ductility enhancement is due to the higher work hardening rate of the FSPed A206 compared to the as-cast A206.

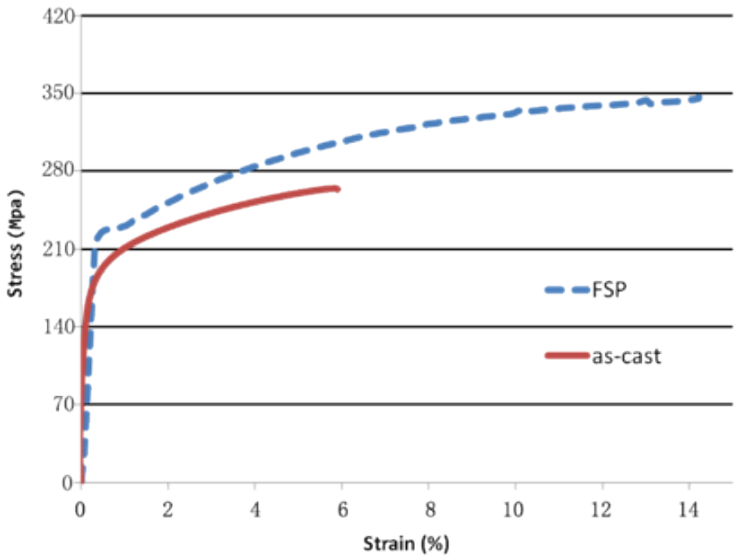

Fig. 8: Typical stress-strain curves for as-cast and FSP A206.

Commonly, when the cyclic load is run to 10^8 or 10^9 cycles (in the ultrasonic fatigue mode), the S-N curve flattens out [19]. The value of the stress amplitude at 10^8 or 10^9 cycles is the fatigue strength of the material and this number is important in industrial applications. A crack can initiate in the specimen when the cyclic load is at or below this value; however, the crack cannot propagate to cause the final failure because the driving force for crack propagation is very low [19, 20]. So far, the value of the fatigue strength cannot be estimated accurately because of the existence of scatters on the S-N plot when the cyclic load is run to very high cycles. In this study, the staircase test methodology was used [21] to reduce the above issue and associated errors, and to correctly determine the fatigue strength of the A206 aluminum alloy. The fatigue test was carried out in the ultrasonic fatigue test mode at a series of stress amplitudes within a pre-determined range.

Fig. 9 shows experimental staircase test results for the as-cast A206 and FSPed A206. Assuming the fatigue strength follows a normal distribution, the mean fatigue strength of the as-cast A206 at 10^8 cycles and the population standard deviation were estimated to be 85.5 Mpa and 1.56 Mpa, respectively. For the FSPed A206, these properties were 165 Mpa and 1.56 Mpa, respectively. It is noted that the fatigue strength of the FSPed A206

was almost two times higher than the as-cast A206. Moreover, the ratio of this fatigue strength to the yield strength was increased for the FSPed A206 compared with the as-cast A206. For the as-cast A206, the yield strength is 190 Mpa, and the fatigue strength endurance is 85 Mpa, which is ~45% of the Y.S; whereas for the FSPed A206, the yield strength is increased to 225 Mpa, and the fatigue strength endurance is raised to more than 75% of the Y.S. The increase in both the yield strength and the ratio indicated that the improved fatigue behavior after FSP was due to the elimination of casting defects, which was microshrinkage porosity in this material.

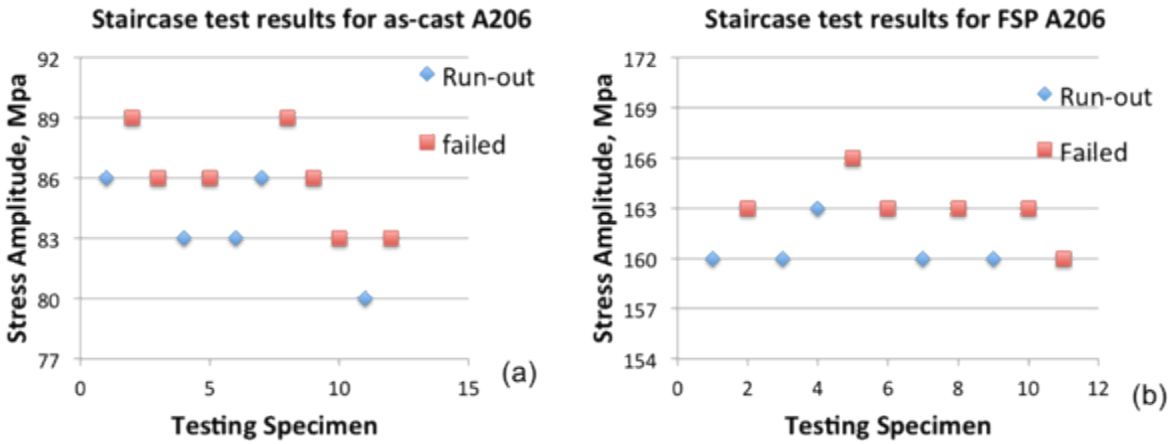

Fig. 9: Experimental staircase test results for A206 at 10^8 cycles (a) as-cast A206; (b) FSPed A206.

In addition to the staircase test, some complementary tests were carried out at higher stress amplitudes to fill in the high-stress-amplitude region data and to obtain the general trend of the S-N curve. To generate the S-N trend curve, the general non-linear model [22] was applied to represent the data. Fig. 10 shows S-N plots of the as-cast A206 and FSPed A206. Specimens tested to 10^8 cycles without failure were regarded as run-outs, and they are marked with arrows in the figure. The influence of FSP on the fatigue behavior of A206 is clearly seen in Figure 10. Compared with the S-N curve of the as-cast specimen, the S-N curve of the FSPed specimen was shifted to the regime where both the stress amplitude and life cycle were higher. FSP resulted in a larger fatigue resistance in the high stress amplitude regime. Fatigue life is longer than 10^6 cycles even when the stress amplitude reached 215 Mpa. Moreover, the FSP S-N plot had a steep transition from 10^6 to 10^7. The number of cycles was only reduced by less than one order of magnitude when the stress amplitude increased from 175 Mpa to 215 Mpa. The total fatigue life consists of the number of cycles required for crack initiation and the number of cycles required for crack growth and propagation to the failure. For cast Al alloys, at high stress amplitudes, the crack is readily initiated at casting defects, such as large pores due to high stress concentration at these locations. In such cases, fatigue life is dominated by the crack growth and propagation stage from the initial crack to the final fatal crack length, because the crack initiation life is negligible [23, 24]. FSP significantly elongated the fatigue life under high stress amplitudes, which indicates that the number of cycles at the crack initiation stage also had impact on the total fatigue life.

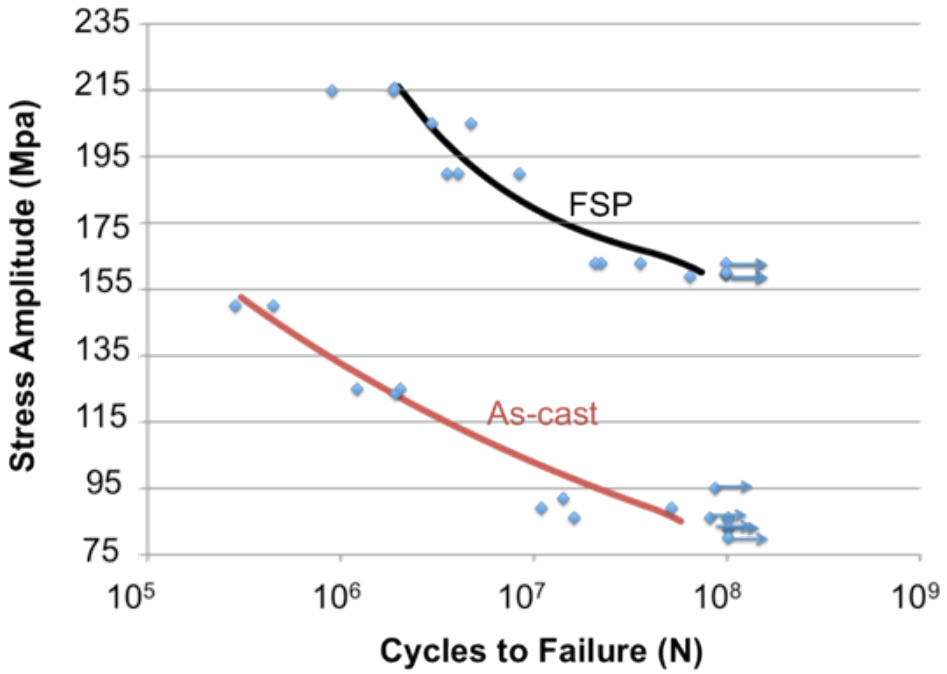

Fig. 10: S-N plots of the as-cast and FSPed A206.

In general, the fracture surface consists of three distinct regions: the crack initiation region, the steady crack growth and propagation region and the fast fracture region. These regions can be identified in the fracture surfaces shown in Fig. 11. The as-cast specimen had a porous fracture surface; large porosities whose diameters were up to 200 μm were observed in the SEM micrograph (Fig. 11a). The crack initiation region for the as-cast specimen (marked with the blue circle in Fig. 11a) was characterized by one/some microshrinkage porosities located near the edge of the specimen. In the crack growth region, there were a large number of transcrystalline cleavages radiating from the crack initiation region. FSP is an advanced tool to mitigate microstructural inhomogeneities. In this study, 97% of the total porosity was eliminated after FSP, especially noticeable is the elimination of the relatively large pores. From Fig. 11b we can see that there are no obvious casting defects in the fracture surface. The fatigue crack initiated from a weak point near the edge where the concentrated stress was high. In the crack propagation region, cracks grew perpendicular to the load direction. River patterns that were parallel to the crack advancing direction were clearly revealed. The final region contained the fast fracture that was caused by overloading.

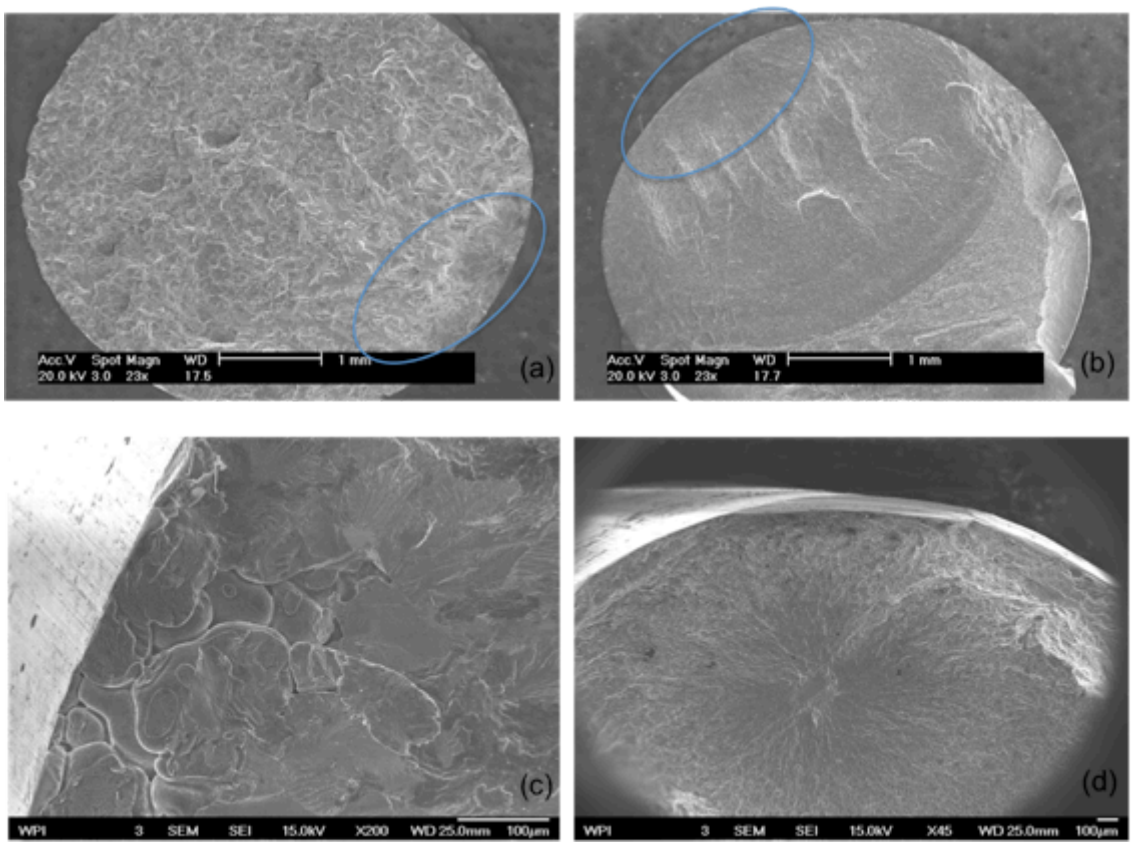

Fig. 11: SEM images showing (a) the fracture surface of the as-cast specimen; (b) the fracture of the FSPed specimen; (c) the fatigue crack initiator of the as-cast specimen; (d) the fatigue crack initiator of the FSPed specimen.

Fig. 11c and Fig. 11d show two SEM micrographs depicting the different fatigue crack initiators of the as-cast and FSPed specimens. For the as-cast specimen, the fatigue crack originated from a pore near the edge (Fig. 11c). The irregular shape of the pore and the dendritic appearance indicates that it was due to microshrinkage porosity. The ECD of the microshrinkage porosity was ~109 μm. Fracture surfaces of 14 as-cast specimens were closely examined with SEM, and all cracks were caused by microshrinkage porosities located at or very close to the specimen surface. The statistical analysis results of these porosities, i.e. ECDs, the number of porosities, and the corresponding stress amplitudes are shown in Table 3. 36% of the fatal cracks were initiated from multiple porosities that were in close proximity to each other (marked with M in Table 2). If a fracture surface contained multiple porosities, the ECD of the largest porosity located near the edge is listed in the Table. It has been found that the crack was always initiated from large porosities, and there was no obvious correspondence between the ECD of the porosity and the applied stress amplitude. These large size porosities were totally eliminated via FSP, which improved the resistance to the crack initiation stage. For the FSPed specimen, although most coarse Al-Cu components were broken into uniform dispersed fine Al-Cu particles, there were still some larger size Al_2Cu compounds remaining in the matrix. Fatigue crack was readily initiated on the interface between the large and hard precipitates and the matrix (see Fig. 11d).

Table 2: Statistical analysis of the crack initiators

Sample No.	σ (Mpa)	ECD (um)	Single or Multiple
1	83	180	S
2	89	105	S
3	90	60	M
4	123.5	39	S
5	86	91	M
6	95	69	M
7	86	146	M
8	150	155	S
9	89	78	M
10	125	107	M
11	125	109	M
12	83	107	M
13	86	141	M
14	104.5	48	S

Composite Fabrication

The feasibility of composite fabrication via FSP was first demonstrated by mixing-in nano-sized Ta powders in the A206 matrix. The composite region was fabricated by filling a cavity of ~400 mm^3 . Fig. 12a shows the microstructure of the composite region which is revealed by SEM, and Fig.12b is the spectrum confirming that the particles viewed as bright spots in the white rectangular shape are Ta powders. In the SEM image, the grey background is the aluminum matrix and the larger and lighter particles (~2 μm) are the Al-Cu precipitates broken by the stirring action of the tool during FSP. In addition to the sizes, the Ta powder has a different morphology compared with the Al-Cu particles. The Ta powders are round, whereas the Al-Cu intermetallic particles have irregular shapes with sharp edges and corners.

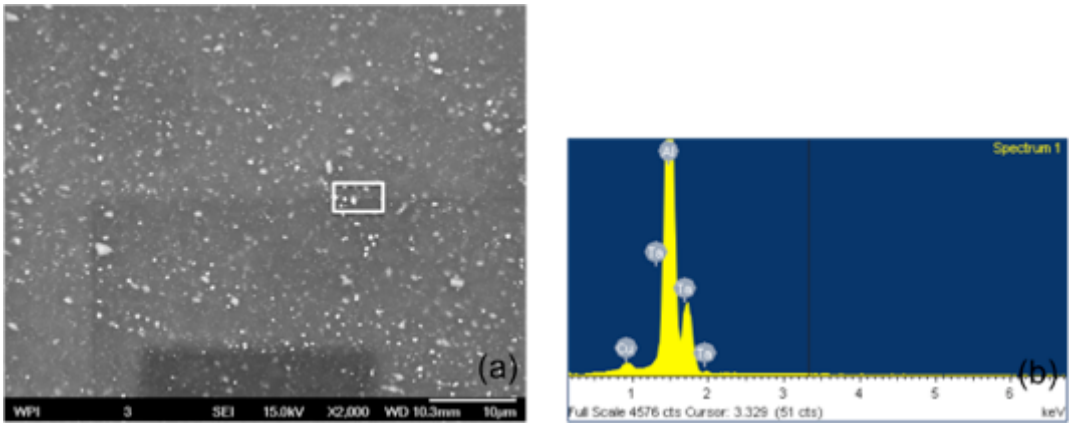

Figure 12： SEM/EDS analysis of the Ta-Al composite layer: (a) SEM image; (b) EDS spectrum showing elements of the detected area.

The following factors account for the homogenous distribution of Ta powders: (1) particle encapsulation – the top of the slot was closed by a cover prior to FSP, which ensured that the powders were well confined in the slot and driven by the movement of the matrix materials during FSP; (2) sufficient input heat - input heat was high enough to ensure adequate materials flow, by which the reinforced particles were easily wrapped and moved around the tool; (3) complete contact between particles and the tool – the FSP tool was made up of two parts: a flat shoulder and a screwed probe at the end of the shoulder. The shoulder was the main heat resource [25], however, the probe contributed a lot on the material movement – the soften metal moved from the advancing side to the retreating side, but only limited to the range of probe diameter [26]. This was the reason that the route along which the tool traversed ahead was offset 1mm from the centerline of the slot - to make sure the advancing side of the probe was fully contacted with the reinforced material.

Fig. 13 shows the effect of multi-pass FSP on the distributions of Ta powders in the composite region. After one pass these powders were stirred into the matrix and the distribution was good (Fig. 13a). However, some powders-agglomeration phenomenon was observed under higher magnification (Fig. 13b white circle). These powder agglomerations could be alleviated by two-pass FSP (Fig. 13c). The powders were dispersed more homogeneously after two-pass FSP compared with the dispersion produced by one-pass FSP.

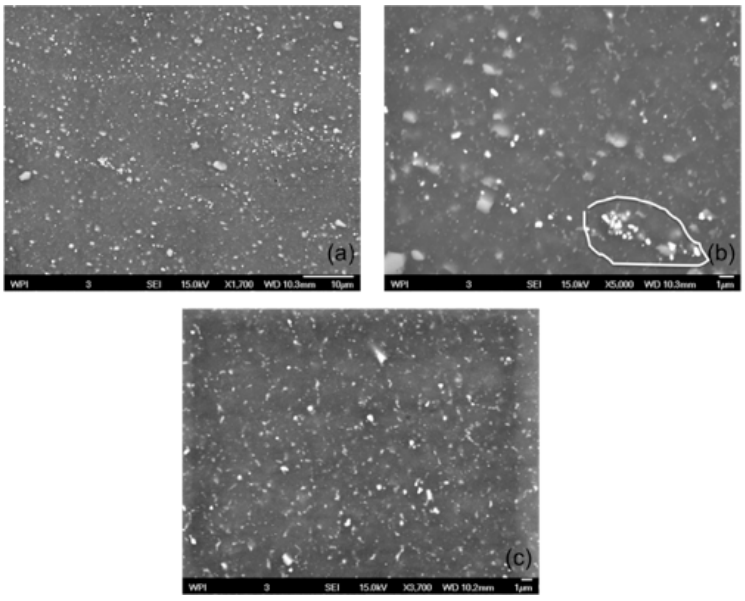

Figure 13: SEM images of the Ta-Al composite layer: (a) overall distribution of Ta powders inside the composite layer after one-pass FSP; (b) Ta powders agglomeration; (c) improved distribution of Ta powders inside the composite layer after two-pass FSP under higher magnification.

SiC/Al composites have high strength as well as good corrosion resistance, and they are the most commonly used composites. Most of SiC/Al composites are fabricated with

large size SiC particles (μm scale), and few can be produced with nano-sized SiC reinforced particles. The aim of this study is to locally fabricate the SiC/Al composites in the cast components by using smaller-size SiC particles (nano scale). Following the success in synthesis of the localized Ta/Al composite, FSP was applied to fabricate the SiC particle-reinforced cast alloy A206 matrix composite using the same setup and procedure as for making Ta/Al composite. The results showed that the distribution of nano-sized SiC powders in the matrix was good (see Fig. 14a). The spectrum in Fig. 14 b shows that the particles within the white rectangular frame in Fig. 14a are SiC particles, and the large particle on the left corner of Fig. 14a is a broken Al-Cu particle. The average size of the initial SiC particles was about 100 nm but some large SiC particles of up to 0.5 μm can be observed in the composite layer.

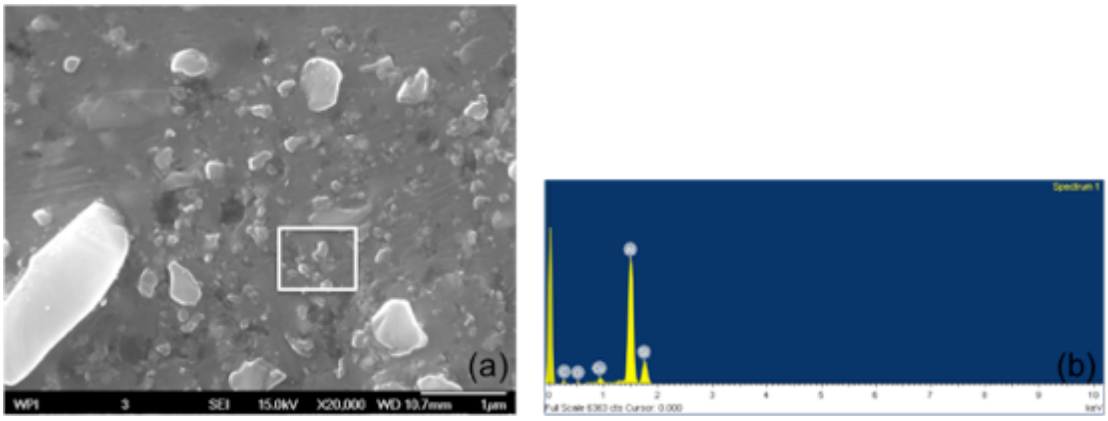

Figure 14： (a) SEM image of the SiC-Al composite: (b) EDS spectrum showing the ingredients of the square-marked area in (a).

The effects of the reinforcement amount on the particle distribution and the quality of the composite were investigated. Tests were conducted on two levels of cavity filling: one was 200 mm^3, which filled half of the slot whose volume was 400 mm^3; another was 400 mm^3 – fully filled the slot. Fig. 15 shows the macrographs of the transverse section of the composite regions fabricated with different amounts of SiC particles. These pictures are composite pictures, which represented a large area, and covers the entire FSP region and vicinity. It can be observed in Fig. 15 a that when the particles filled half of the slot, or the smaller amount of particles were added, the particles were prone to move towards the bottom of the FSP region on the retreating side; few SiC particles can be observed in the top or the middle of the FSP region. When more SiC particles were added, the distribution was improved, and this is shown in Fig. 15b.

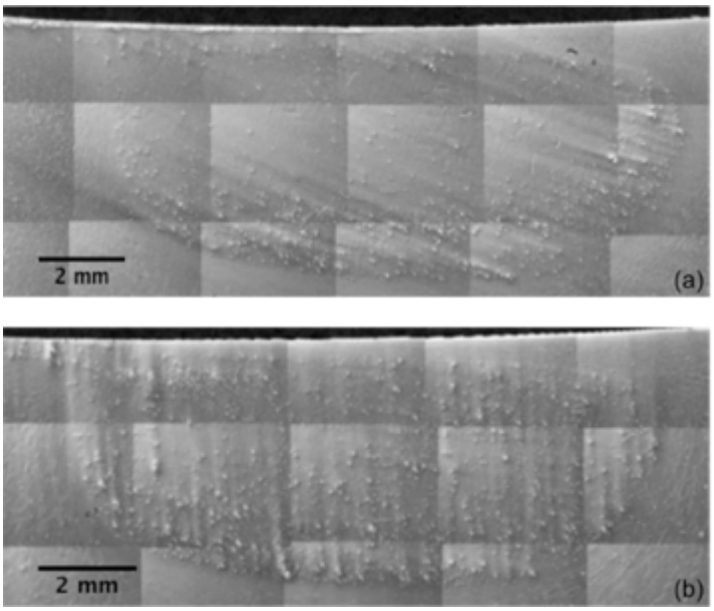

Figure 15: Patterns of SiC particle dispersion in the FSP region – effects of the amount of the SiC particles: (a) 50% cavity filling; (b) 100% cavity filling.

Fig. 16 contains two optical micrographs of the metal matrix composite, which was fabricated by emplacing DRA into the aluminum matrix. The discontinuously reinforced aluminum is a premade solid composite with a high fraction of reinforcement particles. DRA has a continuous metallic phase, into which a second phase is artificially introduced. The matrix of the DRA applied in this study is aluminum alloy 6061 containing about 50 wt% of Si and SiC particles. In Fig. 16 a, the interface zone between the composite region and the aluminum substrate can clearly be seen; the composite layer appears to be well bonded to the aluminum substrate, and the structural integrity is attained – no evidence of porosities or severe reinforcement agglomeration. Fig. 16 b shows the distribution of SiC inside the composite layer at a higher magnification. Apart from the improved distribution, the morphology of SiC was also changed subsequent to FSP – the size was decreased to less than 10 μm, and aspect ratio to 1. The rotating probe produced a breaking effect on the SiC particles, resulting in the cracking of some large particles and the knocking off of corners and sharpened edges from the large particles [26].

Fig. 17 shows the distributions of the DRA in the composites fabricated with different number of passes. It is evident that the particles were dispersed more homogenously after a two-pass than a one-pass FSP, and after 2 passes the particle agglomerations disappeared in the middle of the FSP region.

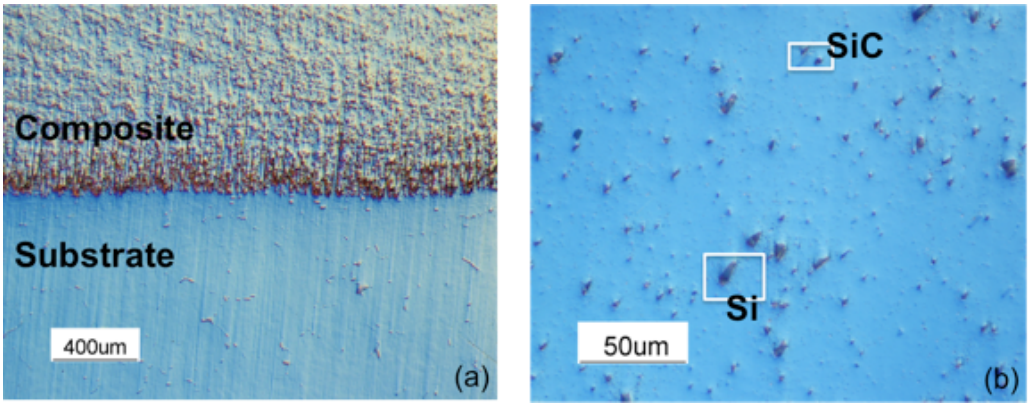

Figure 16: Optical micrographs of DRA/Al composite layer: (a) perfect bonding between surface composite and Al alloy substrate; (b) uniform distribution of DRA in Al alloy matrix.

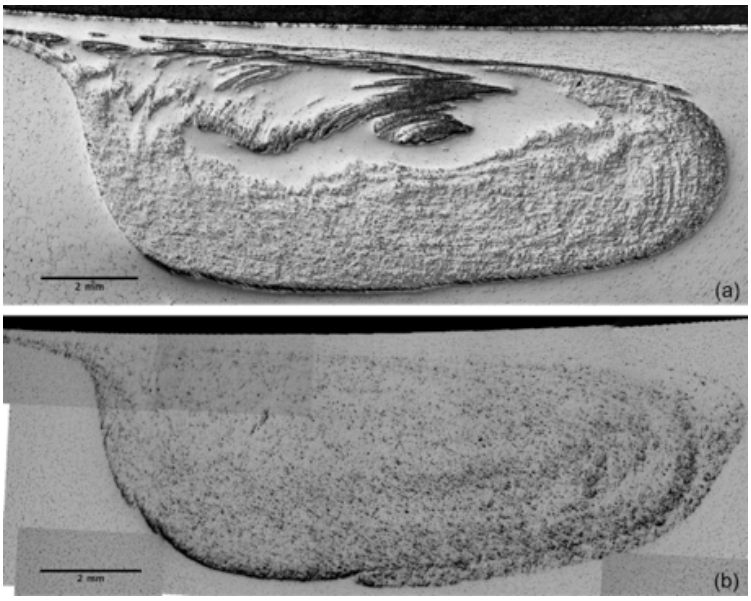

Figure 17: The reinforcement dispersion in the FSP region of the composites fabricated with different number of stirring passes: (a) 1 pass; (b) 2 passes.

CONCLUSIONS

FSP has been applied as an advanced post-processing tool to locally manipulate the microstructure of cast A206 aluminum alloy to refine and strengthen the material. Conclusions of this work are summarized as follows:

- FSP was applied to locally manipulate the A206 microstructure. The grains in the stirred zone of A206 were refined to micrometer levels, and the grain boundaries were clearly revealed. The fraction of high angle boundaries was increased. Second phase particles were distributed uniformly in the aluminum matrix after FSP, and the

size and aspect ratio of these particles decreased significantly. Porosity was nearly eliminated by FSP. The mechanism of the grain refinement was dynamic recrystallization.

- FSP strengthened A206 locally. Microhardness was increased in the FSP region. The shoulder-affected zone became harder than other locations in the FSP region. Strength (both the yield strength and the ultimate tensile strength) and ductility of the A206 improved via FSP. These enhanced mechanical properties resulted from elimination of porosity, breaking of coarse second phases and grain refinement. The fatigue strength at 10^8 for the FSPed A206 was almost twice in value compared with the as-cast A206. Crack initiated at pores near the surface of the as-cast specimens, whereas the crack initiated in the defect-free surface of the FSPed specimen from the interface between the large and brittle second phase particle and the aluminium matrix. The improved fatigue property was due to the increased fracture resistance in both the crack initiation stage.

- FSP is an advanced post-processing technique to produce localized composite structures in cast Al components. Nano-sized Ta powders, nano-sized SiC powders, and discontinuously reinforced aluminum, were synthesized in the cast aluminum A206 matrix. The composites produced for all tested conditions were characterized and evaluated. The feasibility of FSp to manufacture localized composite regions in cast components was validated.

ACKNOWLEDGEMENTS

The authors gratefully acknowledge the member companies of the Advanced Casting Research Center (ACRC) for their support of this work, and for their continued support of research focused on the science and technology of metal casting at Worcester Polytechnic Institute.

REFERENCES

[1] Thomas, W.M.， Nicholas, E.D., Needham, J.C., Murch, M.G., Templesmith, P., and Dawes, C.J., GB Patent Application No. 9125978.8, December 1991.

[2] Cavaliere, P., and De Marco, P.P., “Friction stir processing of a Zr-modified 2014 alloy”, Materials Science and Engineering: A, 462 (1-2) pp. 206-210, 2007.

[3] Cavaliere, P., and Squillace, A., “High temperature deformation of friction stir processed 7075 aluminium alloy”, Materials Characterization, 55 (2) pp. 136-142, 2005.

[4] Cavaliere, P., “Effects of friction stir processing on the fatigue properties of a Zr-modified 2014 alloy”, Materials Characterization, 57 (2) pp. 100-104, 2006.

[5] Sun, N., and Apelian, D., “Friction stir processing of Al cast alloys for high performance applications”, Journal of Metals, Materials and Minerals, 63 pp. 44-50, 2011

[6] Valiev, R.Z., Korznikov, A.V., and Mulyukov, R.R., "Structure and properties of ultrafine-grained materials produced by severe plastic deformation", Materials Science and Engineering: A, 168 (2) pp. 141-148, 1993.

[7] Kapoor, R., De, P.S., and Mishra, R.S., "An analysis of strength and ductility of ultrafine grained Al alloys", Materials Science Forum, 633-634 pp. 165-177, 2010.

[8] Friction stir welding and processing, edited by Mishra, R.S., and Mahoney, M.W., ASM International, Materials Park, Ohio, 2007.

[9] Kwon, Y.J., Saito, N., and Shigematsu, I., "Friction stir process as a new manufacturing technique of ultrafine grained aluminum alloy", Journal of Materials Science Letters, 21 (19) pp. 1473-1476, 2002.

[10] Hofmann, D.C., and Vecchio, K.S., "Submerged friction stir processing (SFSP): An improved method for creating ultra-fine-grained bulk materials", Materials Science and Engineering: A, 402 (1-2) pp. 234-241, 2005.

[11] Ma, Z.Y., and Mishra, R.S., "Development of ultrafine-grained microstructure and low temperature (0.48 T_m) superplasiticity in friction stir processed Al-Mg-Zr", Scripta Materialia, 53 (1) pp. 75-80, 2005.

[12] Charit, I., and Mishra, R.S., "High strain rate superplasticity in a commercial 2024 Al alloy via friction stir processing", Materials Science and Engineering: A, 359 (1-2) pp. 290-296, 2003.

[13] Charit, I., and Mishra, R.S., "Low temperature superplasticity in a friction-stir-processed ultrafine grained Al-Zn-Mg-Sc alloy", Acta Materialia, 53 (15) pp. 4211-4223, 2005.

[14] Ma, Z.Y., Liu, F.C., and Mishra, R.S., "Superplastic deformation mechanism of an ultrafine-grained aluminum alloy produced by friction stir processing", Acta Materialia, 58 (14) pp. 4693-4704, 2010.

[15] Mahoney, M., Fuller, C., Miles, M., and Bingel, W., "Thick plate bending of friction stir processed aluminum alloys", Friction stir welding and processing III, Edited by Jata, K., Mahoney, M., Mishra, R.S., and lienert, T., TMS, pp. 131-137, 2005.

[16] Wang, W., Shi, Q., Liu, P., Li, H., and Li, T., "A novel way to produce bulk SiCp reinforced aluminum metal matrix composites by friction stir processing", Journal of Materials Processing Technology, 209 (4) pp. 2099-2103, 2009.

[17] Zhao, Y.H., Bingert, J.F., Zhu, Y.T., Liao, X.Z., Valiev, R.Z., Horita, Z., Langdon, T.G., Zhou, Y.Z., and Lavernia, E.J., "Tougher ultrafine grain Cu via high-angle grain boundaries and low dislocation density", Applied Physical Letters, 92 (8) 081903, 2008.

[18] Jacob, S., "Quality index in prediction of properties of aluminum castings – a review", AFS Transactions, 108 pp. 99-208, 2000.

[19] Caton, M.J., Jones, J.W., Mayer, H., Stanzl-Tschegg, S., and Allison, J.E., "Demonstration of an endurance limit in cast 319 aluminum", Metallurgical and Materials Transactions A, 34 (1) pp. 33-41, 2003.

[20] Mayer, H., Papakyriacou, M., Zettl, B., and Stanzl-Tschegg, S.E., "Influence of porosity on the fatigue limit of die cast magnesium and aluminium alloys", International Journal of Fatigue, 25 (3) pp. 245-256, 2003.

[21] Dixon, W.J., and Mood, A.M., "A method for obtaining and analyzing sensitivity data", Journal of American Statistical Association, 43 pp. 109-126, 1948.

[22] Conway, J.B., and Sjodahl, L.H., "Analysis and representation of fatigue data", ASM International, Materials park, Ohio, 1991.

[23] Gao, Y.X., Yi, J.Z., Lee, P.D., and Lindley, T.C., "A micro-cell model of the effect of microstructure and defects on fatigue resistance in cast aluminum alloys", Acta materialia, 52 (19) pp. 5435-5449, 2004.

[24] Yi, J.Z., Gao, Y.X., Lee, P.D., and Lindley, T.C., "Microstructure-based fatigue life prediction for cast A356-T6 aluminum-silicon alloys", Metallurgical and Materials Transactions B, 37 (2) pp. 301-311, 2006.

[25] Hofmann, D.C., Vecchio, and D.S., "Thermal history analysis of friction stir processed and submerged friction stir processed aluminum", Materials Science and Engineering: A, 465 (1-2) pp.165-175, 2007.

[26] Feng, A.H., Xiao, B.L., and Ma, Z.Y., "Effect of microstructural evolution on mechanical properties of friction stir welded AA2009/SiCp composite", Composites Science and Technology, 68 (9) pp. 2141-2146, 2008.

Appendix B: *Journal Of Metal, Mineral and Materials, vol.60, No.11, p44-50, 2011*

Friction Stir Processing of Aluminum Cast Alloys for High Performance Applications

N. Sun and D. Apelian
Advanced Casting Research Center
Metal Processing Institute
WPI, Worcester, MA 01609 USA

Introduction

The casting process is a complex one in that three key transport processes take place simultaneously: heat flow, fluid flow and mass flow. This complexity gives rise to heterogeneities within the microstructure such as porosity and other defects. Ironically, successful castings are made not only by controlling of the microstructure, but also through controlling (or management) of defects. In this vein, we have pursued a processing method by which one can locally manipulate the structure, as well as to locally strengthen it. Friction Stir Processing (FSP) has been studied and applied to Al cast alloys for such applications. FSP is developed based on the principle of Friction Stir Welding (FSW) [1]. How does the process work? A high-speed rotating tool (rod) with a flat shoulder and probe penetrates into the pre-fixed work piece; once full contact has been made between the head face of the tool shoulder and the work piece, the non-consumable tool traverses across the work piece. Frictional heating (between the tool and the work piece) is high enough to ensure the needed plastic deformation of the matrix around the moving tool.

What is attractive about FSP is that it can be incorporated in the overall manufacturing cycle as a post-processing step during the machining operation. In this study, we have optimized FSP for processing of Al alloys to locally manipulate the cast microstructure, achieving grain refinement, and porosity elimination as well as second phase homogenization. We have established the mechanism of microstructure evolution and evaluated the resultant mechanical properties. We have also explored and evaluated FSP as a means to locally fabricate composite structures on the cast aluminum substrate. The metal matrix composites processed via FSP have advantages compared to other proceesing pathways. First, the composite layer is fabricated locally to strengthen the material, especially that it can be implemented as a post- casting method. Second, since FSP occurs in the solid state, porosity due to gas evolution, as well as many unwanted interfacial reactions between the reinforcement phase and the matrix are mitigated [2]; Third, FSP can be used as a tool to repair localized defects [3].

Though FSP is a relatively new processing technology, it has been widely applied to modify the microstructure of aerospace aluminum alloys (highly alloyed 2XXX and 7XXX series) to accomplish high-strength, fatigue and fracture resistant Al material [4-8]. Because of these various applications of Friction Stir Processing, this technology has important implications for manufactured components for a variety of automotive and other industrial applications.

In this work we applied FSP on cast A206 aluminum alloy; this alloy has high strength and good machinability, and it has been widely used for a variety of industrial applications. The motive behind this work was to ascertain whether FSP is an enabling technology to enhance the microstructure and to strengthen the material. In addition, we also wanted to investigate and optimize the friction stir process to produce localized particle reinforced zones in cast A206 aluminum components.

Experimental Set-up

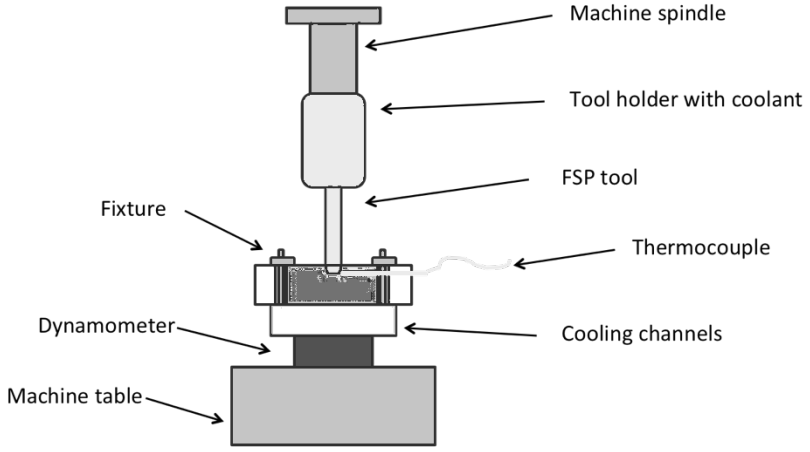

Figure 1: Schematic diagram of the FSP set-up

A schematic of the FSP apparatus is shown in Figure 1. The apparatus consists of the main FSP platform (machine table), the fixture, and instruments (thermocouple and dynamometer) used to detect and record temperature distribution and load profile during processing. The main platform for FSP was a HAAS CNC machine. A specifically designed tool has been applied: the diameter of the tool shoulder was 16 mm, and at the end of the shoulder a tapered probe whose length was 3.2 mm was machined. A tilt angle of three degrees (angle between machine spindle and work piece normal) has been applied to induce forging action at the trailing edge of the shoulder. This was achieved by inserting a back plate whose surface was machined into a slant surface (see Figure 2a). Proper tool penetration depth is very important in generating enough friction heat between the tool and the work piece and producing good FSP finish on the work piece. The minimum tool penetration depth requires the shoulder of the tool has enough contact

with the work piece and this number is calculated based on the real contact condition between the tool and the material (see Figure 2b).

Experimental Parameters

Eck Industries provided 6.25mm thick sand-cast commercial A206 plates. Friction stir processed, the work piece dimensions were: 150 mm X 75 mm X 6.25 mm). Processing parameters used were: tool rotation speed - 1000 RPM, tool traverse speed - 50.8 mm/min and tool penetration depth - 4mm. Samples for metallographic analysis were sectioned perpendicular to the FSP traverse direction. Barker's reagent was used as an etchant for microstructural analysis - both optical and scanning electron microscopy. Focus ion beam (FIB) technique was also used to section the material at particular locations in the processed region and prepare thin films for TEM analysis. TEM work was carried out with a JOEL 2000 microscope operated at 200 kV. Specimens for tensile testing were sectioned along the longitudinal direction of the FSP region. The gauge length of the specimen (25.4 mm) was machined from the center of the friction stirred zone to avoid the interference of the non-homogenous microstructure in the transition regions between the FSP nugget and the base material.

For composite fabrication via FSP, the reinforcement material was first deposited into a cavity machined in the A206 substrate. The reinforcement material can either be in the form of particulates, or consolidated particulates. Two methodologies to fabricate composite layers were investigated: (1) mixing-in 20nm loose Ta powders that were encapsulated, and (2) emplacing a slug of discontinuously reinforced aluminum (DRA, containing 15 wt% SiC in the 6061 Al matrix) into the cavity.

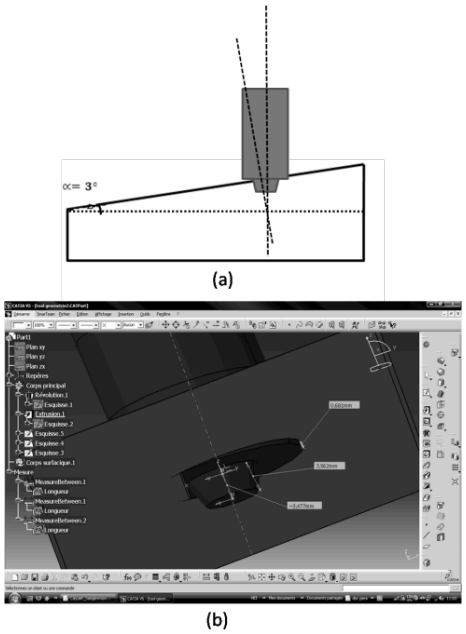

Figure 2: Images of the tilt angle (a) schematic diagram (b) computer modeling of the tool contacting the material

Results and Discussion

Microstructural Evolution

Figure 3 shows macrographs and micrographs taken from the FSPed region. In the schematic diagram of FSP (Figure 3a), "A" refers to the advancing side, on which the tool rotation direction is the same as the tool traverse direction; "R" refers to the retreating side of the work piece, on which the tool rotation direction and tool traverse direction are opposite to each other. Figure 3b shows the macrostructure of A206 processed by FSP. The FSP region has a basin-shaped nugget with a wide top; the left side of the FSP region is not symmetrical with the right side. The advancing side (A) is on the right side of the nugget, and it is characterized by a steep boundary, whereas the retreating side (R) has a curved boundary. The asymmetric boundaries are evidence of the asymmetric strain distribution experienced by the material during processing [9]. Figure 3c and Figure 3d show microstructures of the transition zones (advancing side and retreating side) between the FSP region and the matrix material. The boundary between the FSP region and the original starting dendritic structure is quite evident. In transition areas, grains are elongated and bent, and seem to deform along the shape of the nugget. Moreover, grains deformed more intensely and severely on the advancing side than on the retreating side.

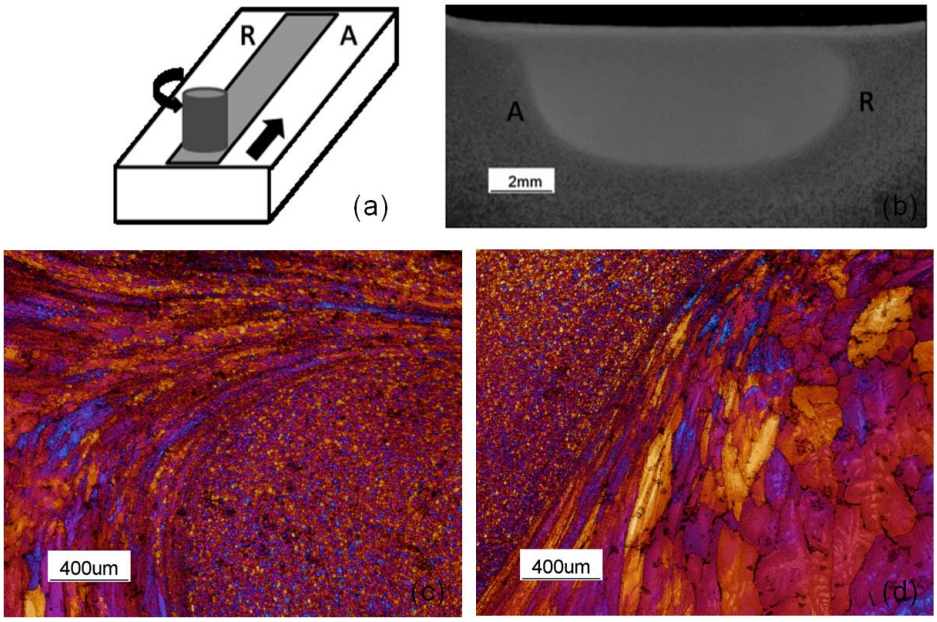

Figure 3: Macro and Micro images of FSP (a) FSP schematic diagram (b) macrograph of FSP region (c) micrograph of retreating side (d) micrograph of advancing side.

Figure 4 shows optical micrographs of A206 pre and post FSP. The microstructure of the as-cast A206 contained second phases that were mainly coarse needle-like $CuAl_2$-CuAl

compounds (Figure 4a). Severe porosity of up to 200-300 μm in length was observed in the aluminum matrix. Large amounts of fine second phase particles that resulted from the broken-up effect of the tool during FSP were uniformly distributed in the processed zone; moreover the porosity was almost eliminated (Figure 4b). Grain boundaries and grain size are clearly depicted in Figure 4c and Figure 4d. The original grain size ranged up to more than 100μm, however, after FSP, equiaxed and fine grains in the size range of 10-15 μm are observed; almost a reduction of one magnitude order.

Figure 5 shows representative TEM micrographs of as-cast A206 and FSP A206. The as-cast A206 is characterized by large grains, inside which coarse Al_2Cu phases are observed. Dislocation density of the as-cast A206 is low (Figure 5a). During FSP, the large downward force and the rapid tool rotation generates much frictional heat between the tool and the work piece, making the material soft enough for plastic deformation to occur. Although majority of the mechanical work was converted to heat, a fraction of the energy was retained as stored energy in the form of dislocations; accordingly, dislocation density increased after FSP. The tool probe broke most of the coarse second phases, and these fine and uniformly dispersed second phase particles have interacted with the tangled dislocations (Figure 5b); this prohibits dislocation movement and strengthens the material during low strain deformation [10]. It is discernible from Figure 5c that many dislocations accumulated at grain boundaries. This microstructure is indicative that dynamic recovery (DRV) occurred during FSP. At the recovery state, free dislocations readily rearranged themselves into subgrains surrounded by low-angle grain boundaries, which released the energy that stored by the material during FSP. The reduction of the stored energy was the driving force for the following recrystallization stage. However, the DRV may not have been completed thoroughly, leaving some cell structures behind (Figure 5d) [11]. These cell structures were lacking enough energy and size advantages [3], and they cannot develop into new grains.

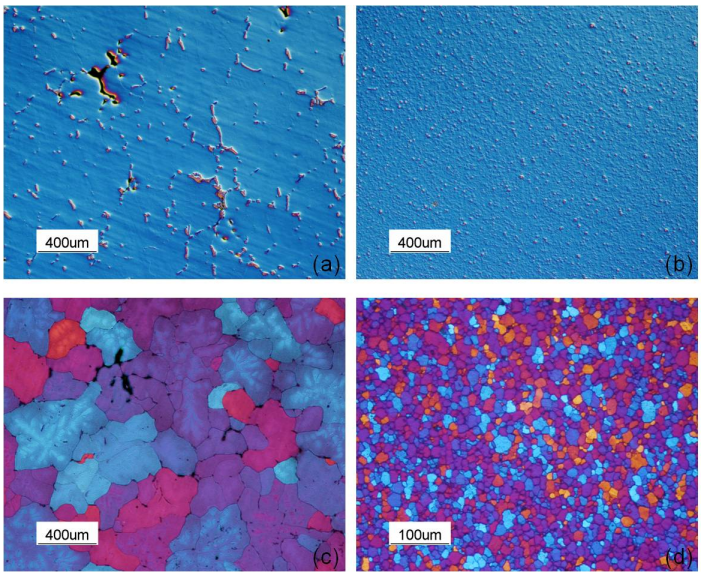

Figure 4: Micrographs of as-cast A206 and FSP A206 (a) second phase distribution of as-cast A206 (b) second phase distribution of FSP A206 (c) grain morphology of as-cast A206 (d) grain morphology of FSP A206.

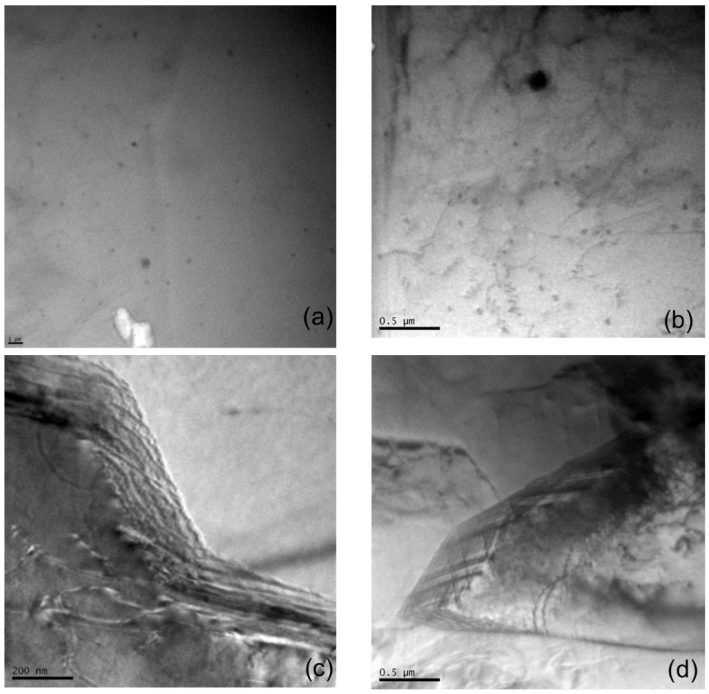

Figure 5: TEM micrographs showing (a) grain morphology and second phases inside a grain of as-cast A206 (b) interaction between fine second phase particles and dislocations inside a refined grain of FSP A206 (c) dislocations at grain boundaries of FSP A206 (d) cell structure inside a grain of FSP A206.

Mechanical Properties Enhancement

Figure 6 shows typical stress-strain curves of as-cast A206 and FSP A206. The yield stress of the as-received A206 was 27.5 Ksi; the UTS was 38.0 Ksi, and the elongation was 5.6%. FSP resulted in a significant increase in the ductility; the elongation increased to 14.2%. Both the yield stress and the UTS increased after FSP: the yield stress increased from 27.5 Ksi to 32.5 Ksi; the UTS of FSP A206 also increased from 38.0 Ksi to 49.5 Ksi. Tensile properties are given in Table 1.

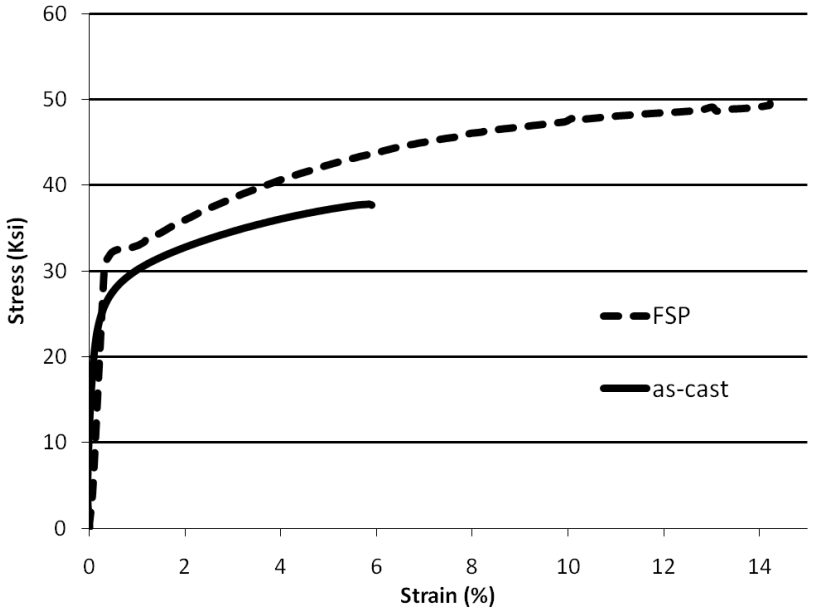

Figure 6: Typical stress-strain curves for as-cast and FSP A206.

FSP introduces a large amount of dislocations in the work piece. The rearrangement or elimination of these dislocations reduces the internal energy of the system; this is the thermodynamic driving force for recrystallization. Since aluminum has a high stacking fault energy, when the temperature is elevated (temperature measured at center of the FSP nugget was about 500°C), recovery occurs before recrystallization, and free dislocations rearrange themselves into subgrains surrounded by low-angle grain boundaries, however, there are still some dislocations remained in refined grains. The tool probe breaks most of the coarse second phases, and those fine and uniformly dispersed second phase particles have interacted with the tangled dislocations; this prohibits dislocation movement and strengthens the material during low strain deformation, which resulted in the increased yield stress. The increased ductility and strength observed is a result of decreasing porosity, refinement of second phases and the grain structure of the work piece.

In order to investigate the thermal response of FSP to post-FSP-heat treatment, commercial T4 and T7 heat treatments were carried out in a conventional furnace for FSP A206 specimens. Typical stress-strain curves of FSP processed, FSP + T4 and FSP + T7 for A206 specimens are shown in Figure 7. The high ductility achieved by FSP was maintained during heat treatment. Due to precipitation hardening we observe a slight increase in UTS values compared to the specimens that were only processed by FSP. However, post-FSP-heat treatment (both T4 and T7) resulted in an obvious decrease in yield stress; this was caused by grain growth, which occurred during post-FSP-heat treatment.

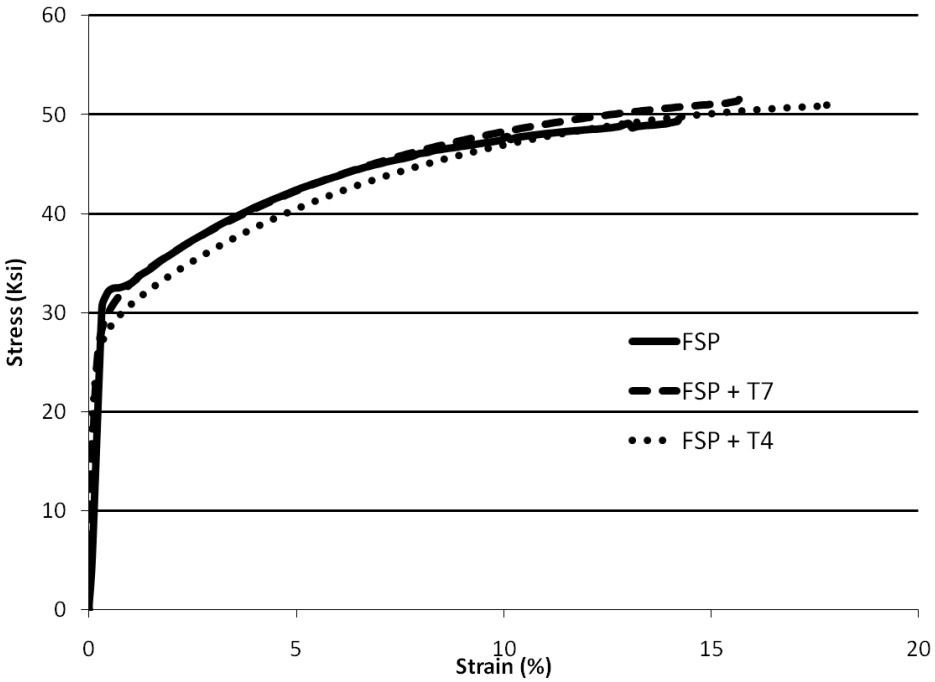

Figure 7: Tensile properties of FSP, FSP + T4 and FSP + T7 of A206.

Many common aluminum alloys experience grain growth during solution treatment; this phenomenon can occur during or after recrystallization especially if the work piece has been subjected a critical amount of prior cold work [12]. The mechanism for grain refinement during FSP is recrystallization and grain growth as discovered during the post-FSP heat treatment. Figure 8 shows microstructures of the as cast, FSP processed, FSP + T4 and FSP + T7 A206; note the grain growth that occurs subsequent to heat treatment. The original grain size of the as-cast A206 is ~ 50 μm (Figure 8a). FSP resulted in significant grain refinement; the grain size decreased to less than 10 μm (Figure 8b). However, after T4 and T7 heat treatment, grain size grew to more than 400 μm (Figure 8c and 8d). We can observe from typical stress – strain curves (shown in Figure 9) that the high ductility has not been sacrificed due to grain growth, which confirms that the observed grain growth is not the abnormal grain growth [13, 14] encountered previous studies. However, deterioration of the yield stress after heat treatment of the FSP specimen is a result of this coarse grain structure.

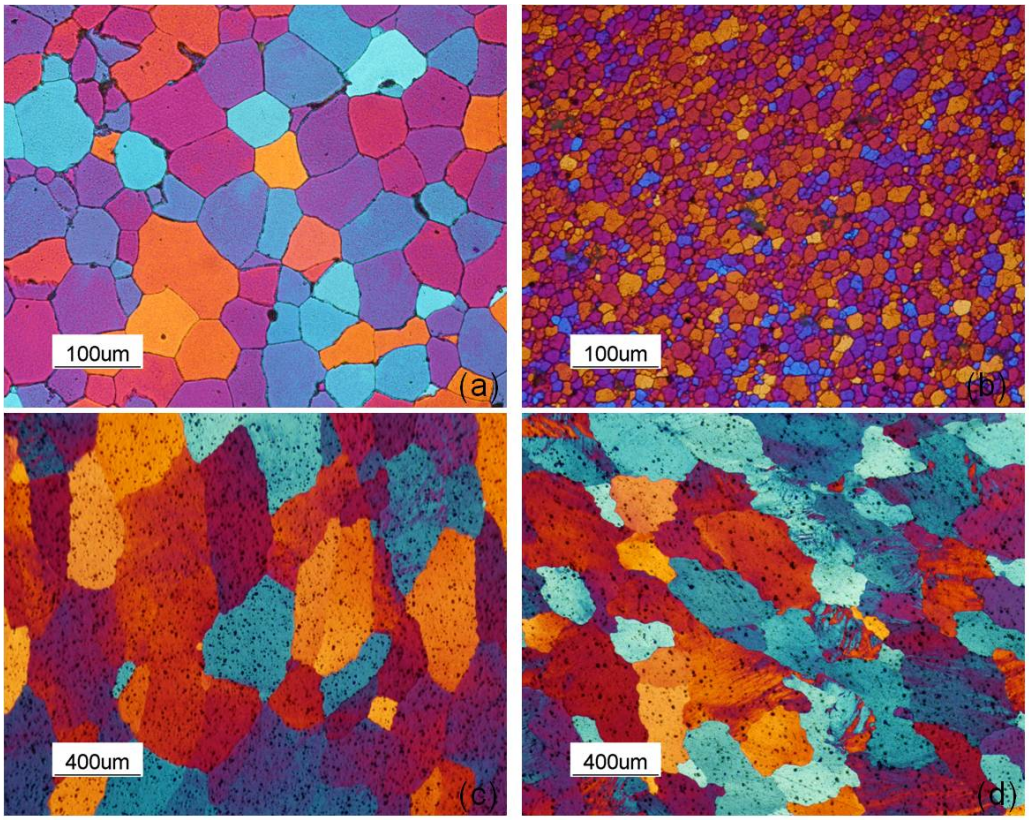

Figure 8: Microstructure showing grain size of A206 (a) As-cast (b) FSP (c) FSP + T4 (d) FSP + T7.

Grain growth that occurs during initial recrystallization is a function of composition, structure, degree of cold work and heating rate; temperatures in excess of 455 °C in common alloys can lead to secondary-recrystallization grain-growth problems [12]. The critical range of cold work is ordinarily about 5 to 15%. Once grain growth occurs, it is not reversible. However, there are ways to minimize the potential of grain growth. A very fast heating rate during solution treatment has been applied to ensure that solution treatment (at 400°C) occurs before grain growth commences. Accordingly, we carried out post-FSP heat treatment using a fluidized bed furnace, which dramatically increases the heat up rate by an order of magnitude.

Figure 9 shows typical stress-strain curves taken from specimens that have been heat-treated in fluidized bed furnace as well as conventional furnace. “FB” Refers to the solution treatment carried out in a fluidized bed furnace, whereas “CONV” refers to the solution treatment carried out in a conventional furnace. Both T4 (FB) and T7 (FB) resulted in increased yield strengths (Figure 9a and Figure 9b).

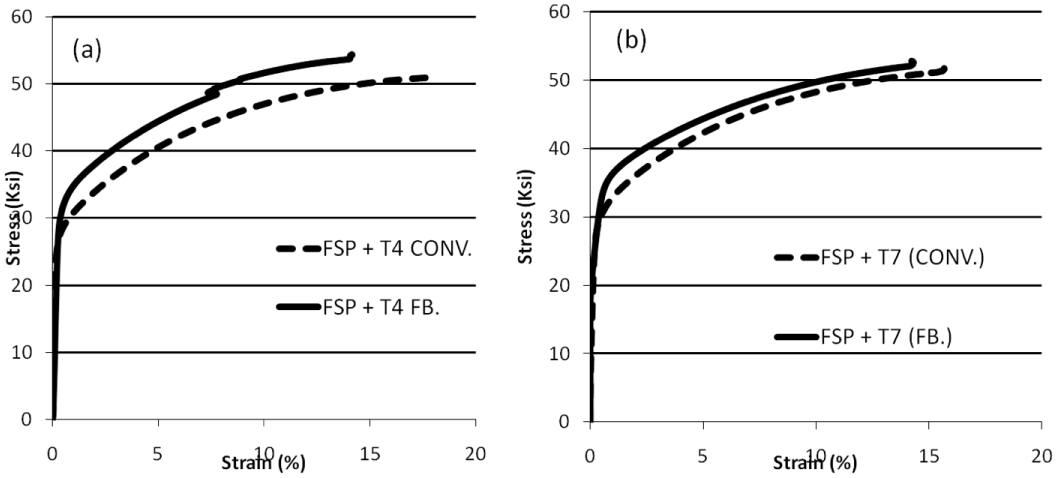

Figure 9 : Typical stress-strain curves (a) FSP + T4 (FB) vs FSP + T4 (CONV) (b) FSP + T4 (FB) vs FSP + T4 (CONV).

Table 1. Tensile Property Values

	Y.S (Ksi)	**UTS (Ksi)**	**EI. (%)**
FSP + T4 (CONV)	29	50.9	17.8
FSP + T4 (FB)	32.5	54.3	14.1
FSP + T7 (CONV)	31	51.7	15.7
FSP + T7 (FB)	36	52.6	14.4
FSP only	32.5	49.5	14.2
As Cast	27.5	38	5.6

Figure 10 depicts two micrographs showing grain size distributions in different specimens. Figure 10a is a collage of 36 micrographs taken in the FSP region, and these 36 micrographs were "stitched" or put together to reveal the grain size distribution in the entire FSP region. In Figure 10a, the specimen was T4 heat-treated with the fluidized bed furnace. Most grains were less than 20 μm; only a small portion of grains, especially in the top of the FSP region, were larger than 100 μm. Figure 10b shows the grain size distribution in the specimen that has only been FSP processed.

Figure 11 shows the difference in grain size of the specimen after solution heat treatment in the conventional and fluidized bed furnaces. Grain growth occurred when the specimen was solution heat treated in the conventional furnace, and coarse grains

reduced the yield strength of the material. When solution treatment was carried out in the fluidized bed furnace, the heating rate was high enough for the specimen to avoid the grain growth stage, and the final grain size was confined to <50 μm, which ensured good strength of the resultant material.

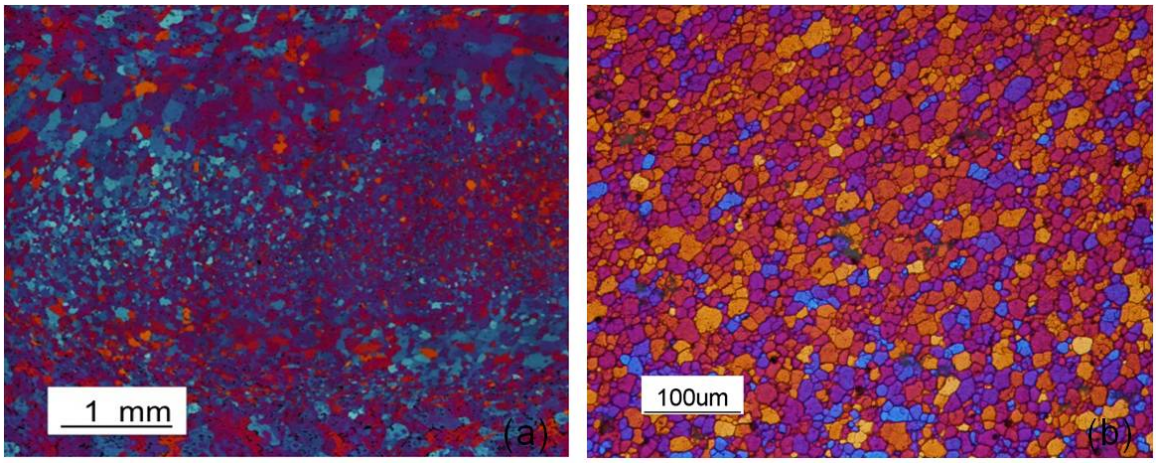

Figure 10: Grain size of A206 in the FSP region (a) grain size of FSP region followed by fluidized bed solution treatment (b) grain size of FSP processed A206

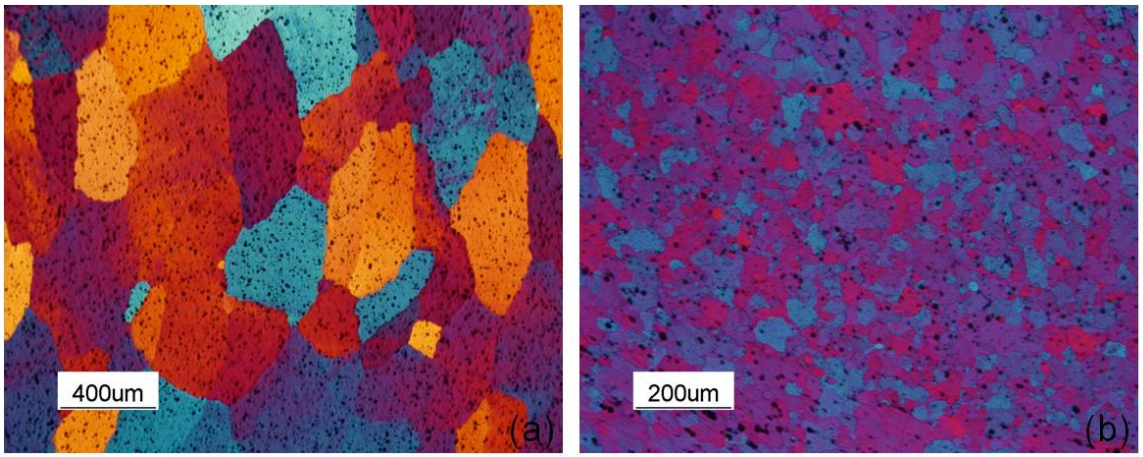

Figure 11: Grain size after solution heat treatment (a) conventional furnace (CONV) (b) fluidized bed furnace (FB).

Composite Fabrication

The feasibility of composite fabrication via FSP was first explored by mixing-in nano-sized Ta powders as reinforcement particles in the aluminum matrix. A 50.8 mm-long 4mm-deep slot was machined in the surface of the A206 substrate to accommodate the reinforcement. There was an offset of 1mm from the center of the FSP tool traverse route to the center of the slot. The composite layer was fabricated by 100%-cavity-filling of nano-sized Ta powders. A pre-processing was carried out with a FSP tool whose probe

was only 1mm long to close the cavity by the welding effect of the tool. This action ensured that nano-sized loose powders are encapsulated into the cavity. Figure 12 shows the microstructure of the composite region that was observed via SEM (Figure 12a). EDS was applied to detect the Ta particulates (Figure 12b). As shown in Figure 12a, the light dot, which is marked in the white rectangular shape, was verified as Ta. The grey color represents the aluminum base, and those larger lighter particles (~2 um) are Al-Cu compound precipitates that were broken up during FSP.

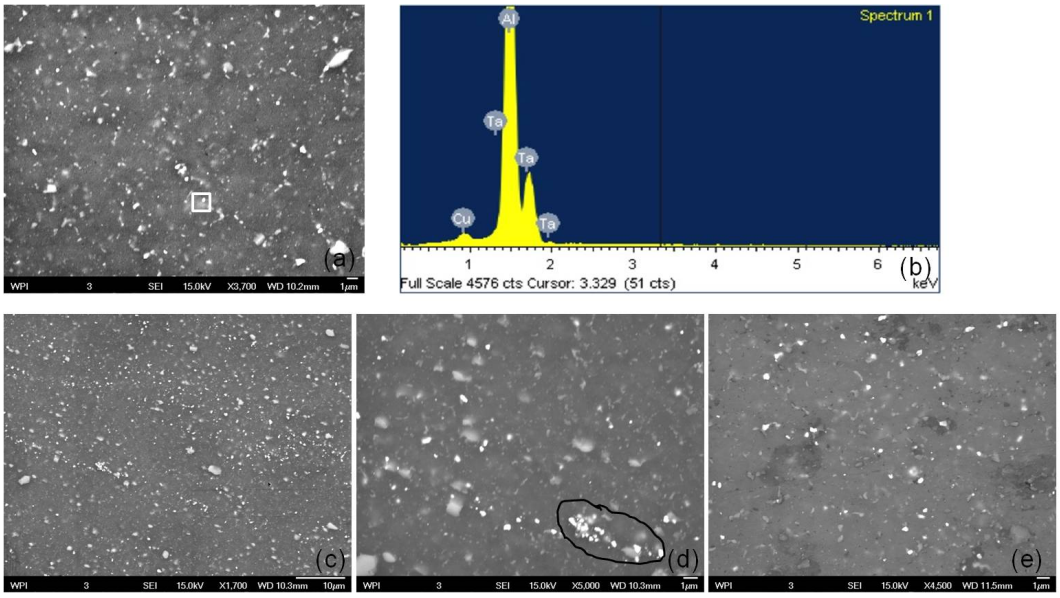

Figure 12: SEM/EDS analysis of the Ta-Al composite layer (a) micrograph showing Ta inside the composite layer (b) EDS analysis (c) Ta distribution in the composite layer after 1-pass FSP (d) agglomerations inside the composite layer after 1-pass FSP (e) homogenous Ta distribution in the composite layer after 2-pass FSP.

The homogenous distribution of Ta powders is attributed to: (1) particle encapsulation – the top of the slot was closed prior to composite fabrication via FSP, which ensured powders were well confined in the slot and driven by the movement of the matrix materials during FSP; (2) sufficient input heat - input heat was high enough to ensure adequate material flow, by which the reinforced particles were easily wrapped and moved around the tool; (3) complete contact between particles and the tool - the FSP tool was made up of two parts: a flat shoulder and a screwed probe at the end of the shoulder. The shoulder was the main heat resource [15], however, the probe contributed a lot on the material movement – the softened metal moved from the advancing side to the retreating side, but only limited to the range of the probe diameter [16]. This was the reason that the route along which the tool traversed ahead was offset 1mm from the centerline of the slot - to make sure the advancing side of the probe was fully contacted with the reinforced material.

Figure 12c and 12d are images showing distributions of Ta powders in the FSP region after one-pass FSP. Overall, powders were stirred into the matrix and the distribution was good (Figure 12c). However, some powder-agglomeration was observed at higher magnifications (Figure 12d black circle). A more homogenous powder distribution can be achieved by multi-pass FSP. Figure 12e shows the distribution of Ta powders in the FSP region after two passes.

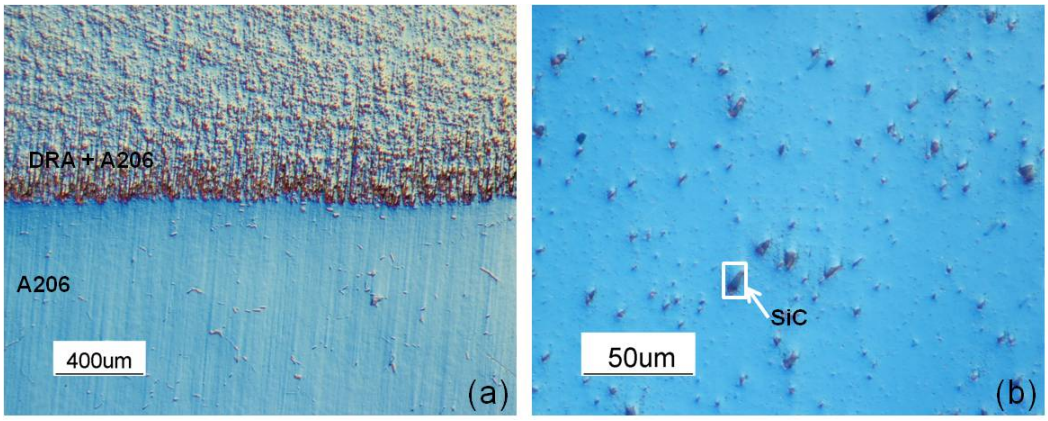

Figure 13: Optical micrographs of DRA/Al composite layer (a) perfect bonding between surface composite and Al alloy substrate (b) uniform distribution of DRA in Al alloy matrix.

Figure 13 contains two optical micrographs of the metal matrix composite, which was fabricated by emplacing Discontinuous Reinforced Aluminum composite (DRA) into the aluminum matrix. In Figure 13a, the interface zone between the surface composite layer and the aluminum substrate can clearly be seen; the composite layer appears to be well bonded to the aluminum substrate, and structural integrity is attained; there is no evidence of porosity or severe reinforcement agglomeration. Figure 13b shows the distribution of SiC inside the composite layer at a higher magnification. Apart from the improved distribution, the morphology of SiC was also changed subsequent to FSP – the size was decreased to less than 10 μm, and the aspect ratio decreased as well. The rotating probe produced a breaking effect on the SiC particles, resulting in the cracking of some large particles and the knocking off of corners and sharpened edges from the large particles.

Conclusions

FSP has been applied as an advanced post-processing tool to locally manipulate A206 microstructure to refine and strengthen the material. This technology has also emerged as a means to produce surface composites and synthesize second phase into the Al matrix in the solid state. Conclusions of this work are summarized as follows:

- FSP was applied to manipulate the A206 microstructure to refine or strengthen locally. The grains in the stirred zone of A206 were refined to micrometer levels, and the grain boundaries were clearly revealed. Second phase particles were distributed uniformly in the aluminum matrix after FSP, and the size and aspect ratio of these

particles decreased significantly. Porosity is nearly eliminated by FSP. Dynamic recovery occurred during FSP before recrystallization.

- FSP improved tensile properties of A206 alloy. Higher ductility and strength resulted from the elimination of porosity, breaking of coarse second phases and grain refinement. Dislocation pinning effect was observed in the specimen that has been FSP processed. Increasing heating rate during solution treatment, such as applying fluidized bed solution treatment mitigates/alleviates grain growth that occurs during conventional furnace T4 and T7 heat treatment; this resulted in increased yield strength.

- Composite fabrication via FSP can be realized by either mixing-in nano-sized particulates or embedding DRA in the cast Al matrix. Tantalum nano-sized powders were used to prove the concept and feasibility, and the method is applicable to a host of nano-sized powders. Powder distribution in the matrix is improved by multi-pass FSP.

Acknowledgments

The authors gratefully acknowledge the member companies of the Advanced Casting Research Center (ACRC) for their support of this work, and for their continued support of research focused on the science and technology of metal casting at Worcester Polytechnic Institute.

References

[1] W.M. Thomas, E.D. Nicholas, J.C. Needham, M.G. Murch, P. Templesmith, and C.J. Dawes, GB Patent Application No. 9125978.8, December 1991.

[2] W.Wang, Q.Shi, P.Liu, H.Li, and T. Li, “A novel way to produce bulk SiCp reinforced aluminum metal matrix composites by friction stir processing”, Journal of Materials Processing Technology 209 (2009), p. 2099.

[3] R.D. Doherty, D.A. Hughes, F.J. Humphreys, J.J. Jonas, D.J. Jensen, M.E. Kassner, W.E. King, T.R. McNelley, H.J. McQueen, and A.D. Rollett, “Current issues in recrystallization: a review”, Materials Science and Engineering A 238 (1997), p. 219.

[4] Z.Y.Ma, R.S.Mishra and M.W.Mahoney, “Superplastic deformation behaviour of friction stir processed 7075Al alloy”, Acta. Mater., 50 (2002), p. 4419.

[5] Y. Zhao, S. Lin, and L. Wu, "The influence of pin geometry on bonding and mechanical properties in friction stir weld 2014 Al alloy", Materials Letters, 59 (2005), p. 2948.

[6] I. Charit, and R.S. Mishra, "High strain rate superplasticity in a commercial 2024 Al alloy via friction stir processing", Materials Science and Engineering: A, 359 (2003), p. 290.

[7] I. Charit, R.S. Mishra and M.W. Mahoney, "Multi-sheet structures in 7475 aluminum by friction stir welding in concert with post-weld superplastic forming", Scripta Materialia, 47(2002), p. 631.

[8] P. Cavaliere, and P.P. DeMarco, "Friction stir processing of a Zr-modified 2014 aluminium alloy", Materials Science and Engineering: A, 462(2007), p. 206.

[9] A.P. Reynolds, “Flow visualization and simulation in FSW”, Scripta materialia 58 (2008), p. 338.

[10] Z.Y. Ma, S.R. Sharma and R.S. Mishra, “Microstructural modification of as-cast Al-Si-Mg alloy by friction stir processing”, Metallurgical and Materials Transactions: A, 37A (2006), p. 3323.

[11] J.Q. Su, T.W. Nelson, and C.J. Sterling, “Grain refinement of aluminum alloys by friction stir processing”, Philosophical Magazine, 86 (2006), p. 1.

[12] ASM Handbook, Volume 4, Heat treating.

[13] J. Dennis, P.S. Bate, and F.J Humphreys, “Abnormal grain growth in Al-3.5 Cu”, Acta materialia, 57 (2009), p. 4539.

[14] I. Charit and R.S. Mishra, “Abnormal grain growth in friction stir processed alloys”, Scripta Materialia 58 (2008), p. 367.

[15] D.C. Hofmann, and D.S. Vecchio, “Thermal history analysis of friction stir processed and submerged friction stir processed aluminum”, Materials Science and Engineering: A, 465 (2007), p.165.

[16] A.H. Feng, B.L. Xiao, and Z.Y. Ma, “Effect of microstructural evolution on mechanical properties of friction stir welded AA2009/SiCp composite”, Composites Science and Technology, 68 (2008), p. 2141.

APPENDIX C: AFS Annual Conference, Columbus, USA, 2012

Localized Strengthening of Cast Al Components via Friction Stir Processing

N. Sun and D. Apelian
Advanced Casting Research Center
Metal Processing Institute
WPI, Worcester, MA 01609 USA

ABSTRACT

Friction stir processing (FSP) is an outgrowth of Friction stir welding (FSW) that locally manipulates the microstructure by imparting a high level of energy in the solid state resulting in improved mechanical properties. Our work to date has shown that FSP can be implemented as a post-casting method to locally eliminate casting defects, such as porosity due to gas evolution during casting. Coarse second phase are broken into fine nearly equiaxed particles and distributed uniformly in the matrix; grain refinement is also attained by dynamic recrystallization during FSP. This results in improved tensile properties and microhardness of the cast Al A206 alloy. Such improvements have important implications for manufactured components for a variety of automotive and other industrial applications. The convenience of FSP as a post-processing step that can easily be carried out during machining operation makes it quite attractive for adoption. These results will be reviewed and discussed.

Keywords: FSP, Microstructural Manipulation, Microhardness, Tensile Properties,

INTRODUCTION

Complexities of casting, which involve heat, fluid and mass transport processes, gives rise to heterogeneities of the microstructure, formation of porosity, and defects. These flaws deteriorate materials properties and limit casting applications. In a sense, it can be considered that high-quality castings are made not only by controlling the microstructure, but more importantly through control (or management) of defects. In this vein, we have pursued a processing method, Friction Stir Processing (FSP), to locally control or affect microstructure, and reduce porosity and defects to improve cast properties. FSP was developed based on the principle of Friction Stir Welding (FSW) [1]. In FSP a high-speed rotating tool (rod) with a flat shoulder and probe penetrates into and traverses across the work piece, while the head face of the tool shoulder fully contacts the workpiece. Frictional heating (between the tool and the work piece) can be high enough to produce plastic deformation of the matrix around the moving tool; this alters and

refines the local microstructure, reduces porosity and defects, which results in local property improvement.

Another attractive feature of FSP is that it can be incorporated in the overall machining cycle as a post-processing option. As will be pointed out in some detail in this paper, the FSP process can be carried out using a CNC milling machine. Most castings are machined and subsequently assembled. Through FSP processing several objectives can be carried out: *(i)* defects can be repaired; *(ii)* porosity can be eliminated in certain specified regions; *(iii)* localized strengthening can be attained; and *(iv)* composite structure can be fabricated into the casting in designated locations to obtain additional property enhancements.

In the relatively short duration after its invention, FSP has been widely applied to create ultra-fine- grained materials [2-4]. One can also locally manipulate the microstructure as has been done in highly alloyed 2XXX and 7XXX series aerospace alloys [5-11] and Al-Si cast alloys [12-16]. Needles to say, such structural enhancements give rise to performance improvements; through FSP one can attain high-strengths as well as significant fatigue and fracture resistant material properties [6, 17-20]. Because of its unique characteristics, FSP has emerged to be a powerful tool for manufacturing components for a variety of automotive and industrial applications.

In this study we applied FSP to cast A206 aluminum alloy. A206 is an important, typical, and widely used Al casting alloy because of its high strength and good machinability. We optimized FSP parameters for Al alloys by locally manipulating and refining the casting microstructure, eliminating or minimizing porosity and refining and homogenizing second phases. We studied and established the mechanism of microstructure evolution in FSP and evaluated the resultant mechanical properties. The motive behind this study was to confirm and demonstrate FSP to be an enabling technology for post-processing of cast A206 components by altering microstructure and enhancing mechanical properties.

DESIGN OF EXPERIMENTS

A schematic of the FSP apparatus is shown in Figure 1. The apparatus was quite stiff to ensure robust processing. The main platform for FSP was a HAAS CNC milling machine. A specifically designed tool holder was used to clamp the FSP tool head (Figure 2a). The FSP tool head (See the red circle in Figure 2a) was made from H13 tool steel. Figure 2b through Figure 2f are schematic diagrams of various types of FSP tool heads. The tool head consisted of two parts: a flat shoulder and a tool probe. During FSP, the tool probe was fully penetrated into the work piece, and the tool shoulder was also contacted with the material to generate a large downward force. The tool probe was conical with threads on the lateral surface. The depth of the material that was treated by FSP relied mainly on the length of the tool probe. Figure 2b through Figure 2f display five FSP tool heads with different shapes and lengths, and these were applied to accommodate work pieces with various depths. The probe shown in Figure 2b was 12.7 mm in length, and it can be used to manipulate microstructure of the material up to 14

mm. Figure 2c and Figure 2d show two tool probes; the length of each probe was 3.2 mm. The bottom of the probe (Figure 2d) was manufactured into a concave surface to enlarge the contacting area between the tool and the workpiece. A shorter probe (1.6 mm) was used (see Figure 2e and Figure 2f) when the depth of the workpiece treated via FSP was small, around 2mm. Results shown in this paper were acquired by applying FSP with the tool probe displayed in Figure 2c. A three-degree tilt angle (angle between machine spindle and work piece normal) was used to induce forging action at the trailing edge of the shoulder. This was achieved by inserting a back plate whose surface was machined into a slant surface (see Figure 3a). Proper tool penetration depth is very important to develop frictional heat between the tool and the work piece and to produce a good FSP finish. The minimum tool penetration depth requires the shoulder of the tool has enough contact with the work piece; this is calculated by the real contact condition between the tool and the material (see Figure 3b). K-type thermocouples were inserted into the work piece at 0.5mm below the center of the FSP tool probe to detect and record the temperature distribution of the work piece. A Kistler dynamometer was used to measure the load profile during processing.

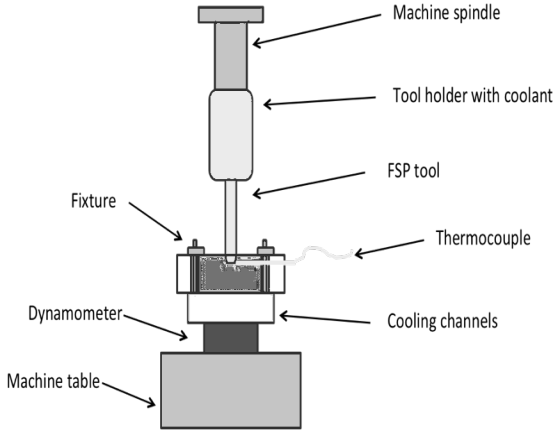

Figure 1: Schematic diagram of the FSP set-up.

Eck Industries provided 6.25mm thick sand-cast commercial A206 plates. The composition of the alloy is shown in Table 1. Friction stir processed workpiece dimensions are: 150 mm X 75 mm X 6.25 mm. FSP was directly applied on the casting surface, and processing parameters were: tool rotation speed - 1000 RPM, tool traverse speed - 50.8 mm/min and tool penetration depth – 3.2mm, 3.6mm, 4mm and 4.4mm, respectively. Samples for metallographic analysis were sectioned perpendicular to the FSP traverse direction. Barker's reagent was used as an etchant for microstructural analysis - both optical and scanning electron microscopy. Focus ion beam (FIB) technique (Zeiss NVision 40) was also used to section the material at particular locations in the processed region and prepare thin films for TEM analysis. TEM work was carried out with a JOEL 2000 microscope operated at 200 kV. Microhardness data were obtained by measuring across the FSP region at particular locations.

Specimens for tensile testing were sectioned along the longitudinal direction of the FSP region. The gauge length of the specimen (25.4 mm) was machined from the center of the

friction stirred zone to avoid the interference of the non-homogenous microstructure in the transition regions between the FSP nugget and the base material.

Table 1. Composition of Commercial A206 Alloy

Si	Fe	Cu	Mn	Mg	Zn	Ti	Ni
0.077	0.046	4.33	0.343	0.256	0.019	0.243	<0.002

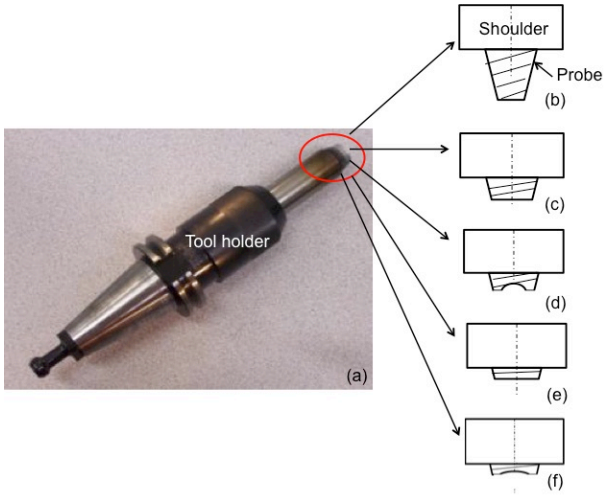

Figure 2: Morphology of the FSP tool (a) Image showing the FSP tool holder and tool head (b) ~ (f) schematic diagrams of the tool head showing various probe shapes and lengths.

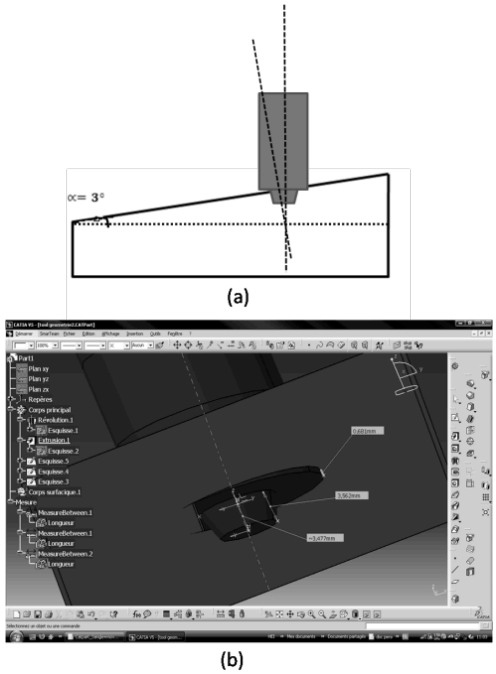

Figure 3: Images of the tilt angle (a) schematic diagram (b) computer modeling of the tool contacting the material.

RESULTS AND DISCUSSION

Friction stir processing is a complex process which involves plastic strain, heat flow and mass flow; these factors are controlled by the geometry of the tool and FSP working parameters [21-23], i.e. tool rotation speed, tool traverse speed and tool penetration depth. The tool geometry profile, as well as the tool rotation speed and the traverse speed can affect the microstructure and mechanical properties of the processed material [24-28]. Particularly, the shape and length of the tool probe determine the defects alleviation and microstructure manipulation depth. Another parameter, the tool penetration depth, directly determines the quality of the FSP finish. A sound FSP finish is a prerequisite to attain enhanced microstructures and properties. Figure 4 shows four work pieces that have been friction stir processed with various tool penetration depths. A smooth defect-free FSP surface finish was acquired when the penetration depth was 4 mm (see Figure 4c). By the use of the dynamometer, we measured the downward force to be ~ 14KN. There was sufficient contact between the tool shoulder and the work piece. Figures 4a and 4b show two typical defects observed when the tool penetration was not deep enough. In Figure 4a, the penetration depth was 3.2 mm; this number was just equal to the length of the tool probe. It is obvious that there was no pressure between the tool shoulder and the work piece, and a groove whose width was the same as the diameter of the tool probe was left behind when the tool probe moved forward. During FSP, the tool shoulder was the main heat source [29] to soften the material, and the tool probe contributed to the material movement. The softened metal moved from the advancing side to the retreating side, but the material movement was only limited to the range of the probe diameter [30]. When the penetration depth increased to 3.6 mm (Figure 4b), although the trailing edge of the tool shoulder was clearly viewed, the contact between the tool shoulder and the work piece was still insufficient; the downward force was around 12KN. In this condition, the material flow was not adequate due to lack of sufficient heat, leaving a cavity on the retreating side in one revolution. A tunnel was generated when the tool traversed ahead. Increasing the penetration depth can eliminate the groove-like defect. However, within the power limitation range of our FSP set-up, the penetration depth also had an upper restriction. When the penetration depth exceeded the upper limitation, although the tool shoulder had a forging action to confine the material, some material was squeezed out of the FSP region (See Figure 4d, where the penetration depth was 4.4 mm).

Figure 5 shows macrographs and micrographs taken from the FSP region. In the schematic diagram of FSP (Figure 5a), “A” refers to the advancing side of the work piece, and “R” refers to the retreating side of the work piece. Figure 5b shows the macrostructure of the FSPed A206. FSP working parameters were: tool rotation speed - 1000 RPM, tool traverse speed - 50.8 mm/min and tool penetration depth – 4 mm. The FSP region has a basin-shaped nugget with a wide top, and the left side of the FSP region is not symmetrical with the right side. The advancing side (A) is on the left side of the nugget, and it is characterized by a steep boundary, whereas the retreating side (R) has a curved boundary. The asymmetric boundary shape indicated that the material in the FSP region experienced the asymmetric strain across the whole FSP zone [31]. Figure 5c and Figure 5d show microstructures of the transition zones (retreating side and advancing

side) between the FSP region and the matrix material. In these transition areas, the material experienced shear forces from the lateral surface of the tool probe. Grains were elongated, bent and deformed along the shape of the nugget. Moreover, the deformation was more intense on the advancing side than on the retreating side.

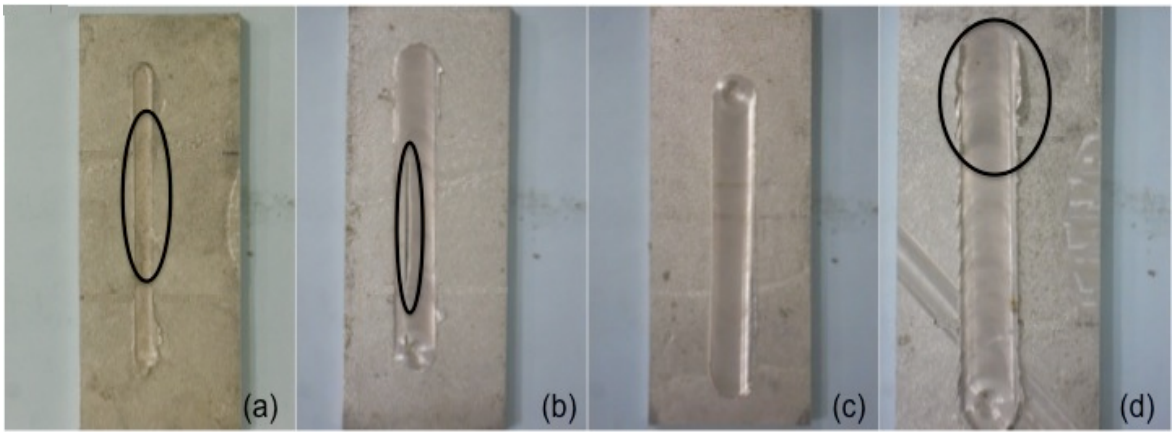

Figure 4: FSP finish: (a) penetration depth 3.2 mm, no tool shoulder mark (b) penetration depth 3.6 mm, groove-like defect (c) penetration depth 4 mm, smooth defect-free surface (d) penetration depth 4.4 mm, material being squeezed out.

Figure 6 shows optical micrographs of A206 pre and post FSP. Grain boundaries and grain size are clearly depicted in Figure 6a and Figure 6b. Dendritic structures and large grains more than 400 μm in diameter are observed in the as-cast A206 microstructure. However, after FSP, equiaxed and fine grains in the size of less than 10 μm were observed, almost a reduction of one magnitude order. In addition, we observe second phase compound refinement. The microstructure of the as-cast A206 contained second phases that were mainly coarse needle-like $CuAl_2$-CuAl compounds (Figure 6c). In contrast, in the FSP region we observe fine second phase particles uniformly distributed (Figure 6d). These small particles were $CuAl_2$-CuAl compounds broken by the stirring action of the probe, and the aspect ratio of the refined particle was near 1. FSP can also be applied as a means to locally alleviate casting defects such as porosity. Severe porosities of up to 200-300 μm in length were observed in the aluminum matrix. However, they were nearly eliminated by FSP (See Figure 6c and Figure 6d).

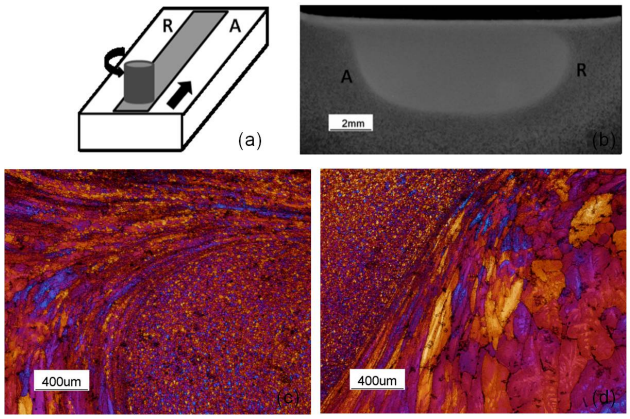

Figure 5: Macro and Micro images of FSP (a) FSP schematic diagram (b) macrograph of FSP region (c) micrograph of retreating side (d) micrograph of advancing side.

From previous friction stir processing studies, fine grains (2-5 μm) have been reported in the FSP nugget region of aluminum alloys [4, 31-33], and the grain refinement has been attributed to dynamic recrystallization (DRX) [31-33]. The recrystallization mechanism for grain refinement has been proposed by assessing the structure via optical microscopy. In this work, we utilized TEM to study the evolution of the refined microstructure, specifically observing the fine grains, subgrain structure and dislocation distribution and morphology. Figure 7 shows the microstructure in the FSP nugget revealed by TEM. The majority of grains observed in the FSP nugget were about 2-3 μm in diameter (Figure 7a), and these fine grains had sharp and regular boundaries. During FSP, the large downward force and the rapid tool rotation speed generated a high amount of frictional heat between the tool and the work piece, making the material soft enough for plastic deformation. Although the majority of the mechanical work was converted to heat and lost when the work piece was cooled down, a fraction of the energy remained in the matrix as stored energy in the form of dislocations; accordingly, dislocation density increased after FSP. From Figure 7b, it is discernible that there were some dislocation pileups at boundaries of those refined grains. The accumulated dislocations broadened these grain boundaries. These observations lead us to conclude that dynamic recovery (DRV) occurred during FSP. At the recovery state, free dislocations readily rearranged themselves into subgrains surrounded by low-angle grain boundaries, which released the energy stored by the material during FSP. The reduction of the stored energy was the driving force for the following recrystallization stage.

Figure 8 shows the average knoop hardness (HK) profiles for the as cast and FSP A206 specimens. The average microhardness of the as-cast A206 was 85 HK, and one can note the variation in values (See the error bar of the as-cast data in Figure 8c). The existence of casting defects, i.e. porosities and inclusions deteriorated the hardness of the material. The microhardness profiles of the FSP processed specimen were selected from two locations in the FSP region (See Figure 8a). Location one was ~ 300 μm below the surface of the work piece. The material between the surface of the work piece and location 1 has sufficient contact with the tool shoulder, and this region is referred to as the shoulder-affected zone. During FSP, the material in the shoulder-affected zone

experienced both huge downward force and shear force from the tool shoulder. Since the tool shoulder produced more than 80% of the total frictional heat, the material in this region absorbed most of the input energy (in the form of heat and force), which induced the recrystallization to take place more completely. From Figure 8b we can see the grain size at location one was smaller than that in the middle of the FSP region. Location two was in the middle of the FSP nugget, and both the tool shoulder and the tool probe affected the material at this location. Microhardness profiles in the shoulder-affected zone (Location one) as well as in the middle of the FSP zone (Location two) were higher in value than the microhardness profile in the parent material. Moreover, the material in the shoulder-affected zone became even harder. The improvement in microhardness is contributed to: (1) grain refinement – dynamic recrystallization occurred during FSP, which resulted in an obvious grain size decrease (from ~300 μm to 5 μm at location one, to10 μm at location two); based on the Hall – Petch principle, material strengthening can be achieved via grain refinement, and this was the reason that location one was harder than location two; (2) casting defect alleviation – FSP eliminated almost all of porosities; (3) second phase break-up – several types of Al-Cu compounds in this alloy can strengthen the material; once those coarse second phases have been broken up by the stirring action of the FSP tool probe, those fine and homogenously dispersed second phase particles result in a uniform hardness distribution in the FSP region.

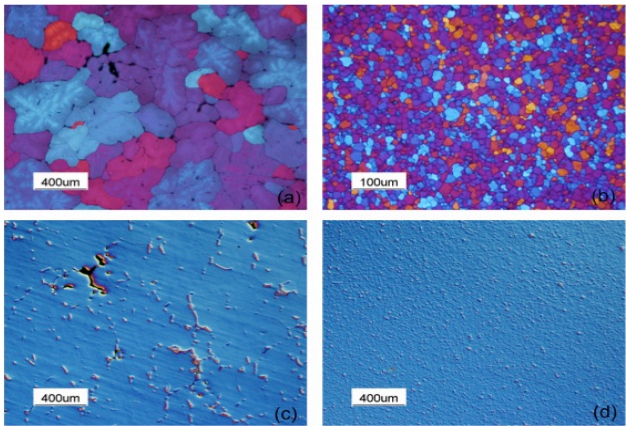

Figure 6: Micrographs of as-cast A206 and FSP A206 (a) grain morphology of as-cast (b) grain morphology of FSP A206 (c) A206second phase distribution of as-cast A206 (d) second phase distribution of FSP A206.

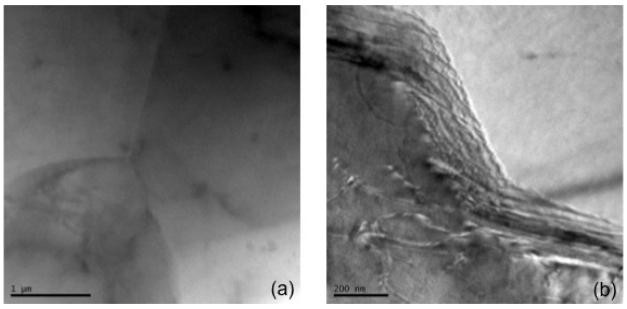

Figure 7: TEM micrographs showing (a) grain morphology showing sharp boundaries (b) dislocations at grain boundaries.

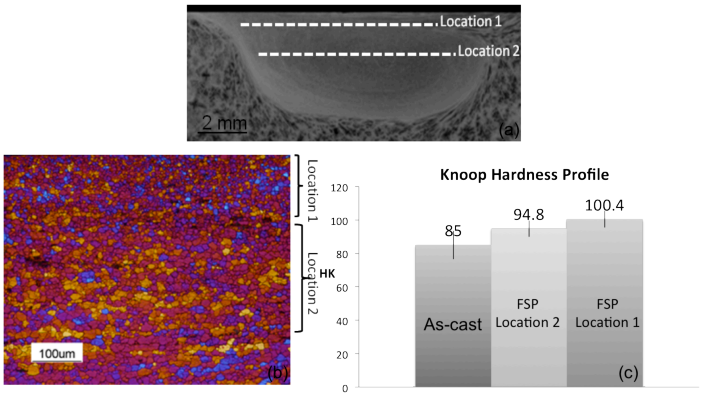

Figure 8: Microhardness profile of the as-cast A206 and FSP A206: (a) macrograph of the FSP region (b) grain size difference in the FSP region (c) microhardness profile.

Table 2. Tensile Property Value

	YS (Mpa)	UTS (Mpa)	Elongation (%)
As Cast	190	262	5.6
FSP	228	342	14.2

Figure 9 shows typical stress-strain curves of as-cast A206 and FSP A206. The yield stress of the as-received A206 was 190 Mpa; the UTS was 262 Mpa, and the elongation was 5.6%. FSP resulted in a significant increase in ductility - the elongation increased to 14.2%. Both the yield stress and the UTS increased after FSP: the yield stress increased from 190 Mpa to 228 Mpa, and the UTS also increased from 262 Mpa to 342 Mpa. Values of these properties are given in Table 2.

FSP has been shown to be an advanced means to locally strengthen the material and increase the ductility of the cast A206 alloy simultaneously. The enhanced yield stress is attributed to dislocation pinning effect. FSP introduces a large amount of dislocations in the work piece. The rearrangement or elimination of these dislocations reduces the internal energy of the system, and this is the thermodynamic driving force for recrystallization to occur. Since aluminum has high stacking fault energy, when the

temperature is elevated (the temperature at center of the FSP nugget was about 500°C), recovery occurs before recrystallization, and free dislocations rearranged themselves into subgrains surrounded by low-angle grain boundaries. However, some dislocations still remained behind at grain boundaries or within those refined grains. The tool probe broke most of the coarse second phases, and those fine and uniformly dispersed second phase particles interact with the tangled dislocations, which further prohibits dislocation movement and thus strengthens the material during low strain deformation. The dislocation pinning effect resulted in increased yield stress. The increase in UTS and ductility resulted from the porosity elimination and the refinement of grains and second phases.

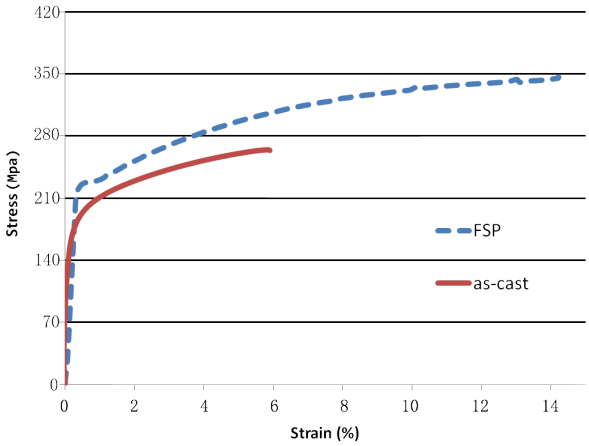

Figure 9: Typical stress-strain curves for as-cast and FSP A206.

CONCLUSIONS

FSP has been applied as an advanced post-processing tool to locally manipulate the microstructure of cast A206 aluminum alloy to refine and strengthen the material. Conclusions of this work are summarized as follows:

- The effect of the tool penetration depth during FSP was investigated. A defect-free FSP finish was acquired when there was sufficient contact between the tool shoulder and the work piece.

- FSP was applied to locally manipulate the A206 microstructure. The grains in the stirred zone of A206 were refined to micrometer levels, and the grain boundaries were clearly revealed. Second phase particles were distributed uniformly in the aluminum matrix after FSP, and the size and aspect ratio of these particles decreased significantly. Porosity was nearly eliminated by FSP. The mechanism of the grain refinement was dynamic recrystallization.

- FSP strengthened A206 locally. Microhardness was increased in the FSP region. The shoulder-affected zone became harder than other locations in the FSP region. Strength

(both the yield strength and the ultimate tensile strength) and ductility of the A206 improved via FSP. These enhanced mechanical properties resulted from elimination of porosity, breaking of coarse second phases and grain refinement.

ACKNOWLEDGMENTS

The authors gratefully acknowledge the member companies of the Advanced Casting Research Center (ACRC) for their support of this work, and for their continued support of research focused on the science and technology of metal casting at Worcester Polytechnic Institute.

REFERENCES

[1] Thomas, W.M.， Nicholas, E.D., Needham, J.C., Murch, M.G., Templesmith, P., and Dawes, C.J., GB Patent Application No. 9125978.8, December 1991.

[2] Hofmann, D.C., and Vecchio, K.S., "Submerged Friction Stir Processing (SFSP): An Improved Method for Creating Ultra-Fine-Grained Bulk Materials," Materials Science and Engineering: A, 402(1-2) pp. 234-241, 2005.

[3] Kwon, Y.J., Saito, N., and Shigematsu, I., "Friction Stir Process as a New Manufacturing Technique of Ultrafine Grained Aluminum Alloy," Journal of Materials Science Letters, 21(19) pp. 1473-1476, 2002.

[4] Su, J. -., Nelson, T. W., and Sterling, C. J., "Grain Refinement of Aluminum Alloys by Friction Stir Processing," Philosophical Magazine, 86 pp. 1-24, 1 January 2006.

[5] Cavaliere, P., and De Marco, P.P., "Friction Stir Processing of a Zr-Modified 2014 Aluminium Alloy," Materials Science and Engineering: A, 462(1-2) pp. 206-210, 2007.

[6] Jata, K., Sankaran, K., and Ruschau, J., "Friction-Stir Welding Effects on Microstructure and Fatigue of Aluminum Alloy 7050-T7451," Metallurgical and Materials Transactions A, 31(9) pp. 2181-2192, 2000.

[7] Jones, M.J., Heurtier, P., Desrayaud, C., "Correlation between Microstructure and Microhardness in a Friction Stir Welded 2024 Aluminium Alloy," Scripta Materialia, 52(8) pp. 693-697, 2005.

[8] Rhodes, C.G., Mahoney, M.W., Bingel, W.H., "Fine-Grain Evolution in Friction-Stir Processed 7050 Aluminum," Scripta Materialia, 48(10) pp. 1451-1455, 2003.

[9] Salem, H. G., "Friction Stir Weld Evolution of Dynamically Recrystallized AA 2095 Weldments," Scripta Materialia, 49(11) pp. 1103-1110, 2003.

[10] Sullivan, A., and Robson, J.D., "Microstructural Properties of Friction Stir Welded and Post-Weld Heat-Treated 7449 Aluminium Alloy Thick Plate," Materials Science and Engineering: A, 478(1-2) pp. 351-360, 2008.

[11] Sutton, M.A., Yang, B., Reynolds, A.P., "Microstructural Studies of Friction Stir Welds in 2024-T3 Aluminum," Materials Science and Engineering A, 323(1-2) pp. 160-166, 2002.

[12] Amirizad, M., Kokabi, A.H., Gharacheh, M.A., "Evaluation of Microstructure and Mechanical Properties in Friction Stir Welded A356 + 15%SiCp Cast Composite," Materials Letters, 60(4) pp. 565-568, 2006.

[13] Ma, Z., Sharma, S., and Mishra, R., "Microstructural Modification of as-Cast Al-Si-mg Alloy by Friction Stir Processing," Metallurgical and Materials Transactions A, 37(11) pp. 3323-3336, 2006.

[14] Ma, Z.Y., Sharma, S.R., and Mishra, R.S., "Effect of Friction Stir Processing on the Microstructure of Cast A356 Aluminum," Materials Science and Engineering: A, 433(1-2) pp. 269-278, 2006.

[15] Rao, A.G., Rao, B.R.K., Deshmukh, V.P., Shah, A.K., Kashyap, B.P., "Microstructural Refinement of a Cast Hypereutectic Al–30Si Alloy by Friction Stir Processing," Materials Letters, 63(30) pp. 2628-2630, 2009.

[16] Zhang, Y., Ma, N., Le, Y., "Mechanical Properties and Damping Capacity After Grain Refinement in A356 Alloy," Materials Letters, 59(17) pp. 2174-2177, 2005.

[17] Sharma, S.R., and Mishra, R.S., "Fatigue Crack Growth Behavior of Friction Stir Processed Aluminum Alloy," Scripta Materialia, 59(4) pp. 395-398, 2008.

[18] Sharma, S.R., Ma, Z.Y., and Mishra, R.S., "Effect of Friction Stir Processing on Fatigue Behavior of A356 Alloy," Scripta Materialia, 51(3) pp. 237-241, 2004.

[19] Lee, W.B., Yeon, Y.M., and Jung, S.B., "The Improvement of Mechanical Properties of Friction-Stir-Welded A356 Al Alloy," Materials Science and Engineering A, 355(1-2) pp. 154-159, 2003.

[20] Ma, Z.Y., Pilchak, A.L., Juhas, M.C., "Microstructural Refinement and Property Enhancement of Cast Light Alloys Via Friction Stir Processing," Scripta Materialia, 58(5) pp. 361-366, 2008.

[21] Zhang, H., Wu, H., Huang, J., "Effect of Welding Speed on the Material Flow Patterns in Friction Stir Welding of AZ31 Magnesium Alloy," Rare Metals, 26(2) pp. 158-162, 2007.

[22] Rajamanickam, N., Balusamy, V., Madhusudhanna Reddy, G., "Effect of Process Parameters on Thermal History and Mechanical Properties of Friction Stir Welds," Materials & Design, 30(7) pp. 2726-2731, 2009.

[23] Peel, M., Steuwer, A., Preuss, M., "Microstructure, Mechanical Properties and Residual Stresses as a Function of Welding Speed in Aluminium AA5083 Friction Stir Welds," Acta Materialia, 51(16) pp. 4791-4801, 2003.

[24] Elangovan, K., and Balasubramanian, V., "Influences of Pin Profile and Rotational Speed of the Tool on the Formation of Friction Stir Processing Zone in AA2219 Aluminium Alloy," Materials Science and Engineering: A, 459(1-2) pp. 7-18, 2007.

[25]Cavaliere, P., Campanile, G., Panella, F., "Effect of Welding Parameters on Mechanical and Microstructural Properties of AA6056 Joints Produced by Friction Stir Welding," Journal of Materials Processing Technology, 180(1-3) pp. 263-270, 2006.

[26] Elangovan, K., and Balasubramanian, V., "Influences of Tool Pin Profile and Welding Speed on the Formation of Friction Stir Processing Zone in AA2219 Aluminium Alloy," Journal of Materials Processing Technology, 200(1-3) pp. 163-175, 2008.

[27] Karthikeyan, L., Senthilkumar, V.S., and Padmanabhan, K.A., "On the Role of Process Variables in the Friction Stir Processing of Cast Aluminum A319 Alloy," Materials & Design, 31(2) pp. 761-771, 2010.

[28] Song, K. H., Fujii, H., and Nakata, K., "Effect of Welding Speed on Microstructural and Mechanical Properties of Friction Stir Welded Inconel 600," Materials & Design, 30(10) pp. 3972-3978, 2009.

[29] Hofmann, D.C., and Vecchio, K.S., "Thermal History Analysis of Friction Stir Processed and Submerged Friction Stir Processed Aluminum," Materials Science and Engineering: A, 465(1-2) pp. 165-175, 2007.

[30] Feng, A.H., Xiao, B. L., and Ma, Z. Y., "Effect of Microstructural Evolution on Mechanical Properties of Friction Stir Welded AA2009/SiCp Composite," Composites Science and Technology, 68(9) pp. 2141-2148, 2008.

[31] Reynolds, A.P., "Flow Visualization and Simulation in FSW," Scripta Materialia, 58(5) pp. 338-342, 2008.

[32] Rhodes, C.G., Mahoney, M. W., Bingel, W. H., "Effects of Friction Stir Welding on Microstructure of 7075 Aluminum," Scripta Materialia, 36(1) pp. 69-75, 1997.

[33] Jata, K.V., and Semiatin, S.L., "Continuous Dynamic Recrystallization during Friction Stir Welding of High Strength Aluminum Alloys," Scripta Materialia, 43(8) pp. 743-749, 2000.

APPENDIX D: *5th International Conference on LMT 2011, Lüneburg, Germany, Materials Science Forum, Vol. 690, pp. 125-128*

Composite Fabrication Via Friction Stir Processing

N. Sun and D. Apelian
Metal Processing Institute
WPI, Worcester, MA 01609 USA

ABSTRACT

Friction stir processing (FSP) is a post-processing method that locally manipulates the microstructure by imparting a high level of energy in the solid state giving rise to improved mechanical properties. Additionally, FSP has emerged as an advanced tool to produce surface composites and synthesize the second phase into the matrix. In the current study, FSP was investigated for the manufacture of localized zones of composite materials made by the emplacement of a second phase into cast A206 Al alloy matrix. Both the discontinuously reinforced aluminum (DRA) and some encapsulated powders (nano-sized SiC or Ta) were used for the second phase emplacement. Through SEM and EDS mapping, the morphology and distribution of second phase particles have been studied. The work shows that friction stir processing is a viable means of producing localized composite zones in Al components.

KEYWORDS: Friction Stir Processing, Composite Fabrication, SiC.

INTRODUCTION

As a recent outgrowth of the Friction Stir Welding (FSW) process [1], Friction Stir Processing (FSP) has been shown to eliminate casting defects and refine the microstructure at a pre-determined location [2,3]; this results in improved mechanical properties and enhanced corrosion resistance [4-6]. There is a growing need for Al metal matrix composites, and FSP is a viable means of producing components with localized composite structures [7]. How does the process work? A high-speed rotating tool with a flat shoulder and probe penetrates into the pre-fixed workpiece; once full contact has been made between the head face of the tool shoulder and the workpiece, the non-consumble tool traverses across the workpiece. Frictional heating (between the tool and the workpiece) is high enough to ensure the needed plastic deformation of the matrix around the moving tool. The second phase is emplaced within the workpiece and is transferred within the matrix, and finally it is dispersed in the FSP processed zone area. Producing metal matrix composites using FSP has advantages compared to traditional manufacturing methods: (i) the composite layer is fabricated locally at pre-determined zones rather than throughout the whole bulk; (ii) FSP processing can easily be carried out as a post casting operation, such as during the machining stage; (iii) since FSP occurs

in the solid state, hydrogen porosity, residual stress, as well as many unwanted interfacial reactions between the reinforcement phase and the matrix are mitigated [8]; lastly, (iv) FSP can be used as a tool to repair localized defects [9].

The aim of this study is to investigate and optimize the friction stir process to produce localized particle reinforced zones in cast aluminum components. In this study, the reinforcement material was deposited in machined cavities in the workpiece, and three methodologies were applied to find the optimum processing method.

EXPERIMENTAL DETAILS

Commercially sand cast A206 was acquired from Eck Industries; the nominal composition of the alloy being Al-4.33Cu-0.077Si-0.046Fe-0.256Mg-0.343Mn. FSP was carried out and the dimensions of the workpiece were 15cm X 7.6cm X 0.6cm. The tool shoulder diameter was 16mm, with a screwed taper probe at its end. The length of the probe was 3.2mm. A three degrees tilt angle was applied during processing. A slot, which was 50mm in length, 2mm in width and 4mm in depth, was machined in the workpiece to accommodate the reinforcement particles into the aluminum matrix. The route along which the tool traversed ahead was offset 1mm from the centerline of the slot to make sure the advancing side of the tool was fully contacted with the reinforced material.

Three methodologies to fabricate composite layers were investigated: mixing-in 20nm Ta powders, mixing-in 100nm SiC powders, and emplacing discontinuously reinforced aluminium (DRA, which is already a solid composite containing 15 wt% SiC in the 6061 Al matrix) in the aluminium matrix, respectively. For composite fabrication with particular reinforcement, powders were encapsulated prior to FSP by a cover. FSP was carried out at a tool rotating speed 1000 RPM and traversing speed 50 mm/min. Effects of multi-pass-FSP (up to two passes) and the amount of the reinforcement material were investigated. Samples were sectioned perpendicular to the FSP traverse direction; SEM and EDS were applied to reveal distributions of the reinforcement material.

RESULTS AND DISCUSSION

The feasibility of composite fabrication via FSP was first explored by mixing-in nano-sized Ta powders as reinforcement particles in the aluminum matrix. The composite layer was fabricated by 100%-cavity-filling (800 mm^3) of nano-sized Ta powders. After one-pass FSP processing, the microstructure of this region was depicted via SEM (Fig. 1a). EDS was applied to detect the Ta powder (Fig. 1b). As shown in Fig. 1a, the light dot, which was marked in the white rectangular shape, was verified as the Ta powder. The grey color represented the aluminum base, and those larger lighter particles (~2 um) were Al-Cu compound precipitations that were broken up during FSP.

The homogenous distribution of Ta powders was attributed to: (1) particle encapsulation – the top of the slot was closed by a cover prior to FSP, which ensured powders were

well confined in the slot and driven by the movement of the matrix materials during FSP; (2) sufficient input heat - input heat was high enough to ensure adequate materials flow, by which the reinforced particles were easily wrapped and moved around the tool; (3) complete contact between particles and the tool - the FSP tool was made up of two parts: a flat shoulder and a screwed probe at the end of the shoulder. The shoulder was the main heat resource [10], however, the probe contributed a lot on the material movement – the soften metal moved from the advancing side to the retreating side, but only limited to the range of probe diameter [11]. This was the reason that the route along which the tool traversed ahead was offset 1mm from the centerline of the slot - to make sure the advancing side of the probe was fully contacted with the reinforced material.

Fig. 1c and 1d are images showing distributions of Ta powders in the FSP region after one-pass FSP. Overall, powders were stirred into the matrix and the distribution was good (Fig. 1c). However, some powders-agglomeration phenomenon was observed under higher magnification (Fig. 1d black circle). Multi-pass FSP processing effects were also studied, and Fig. 1e shows the distribution of Ta powders in the FSP region after two passes. Powders were dispersed more homogeneously compared with the dispersion after one-pass FSP.

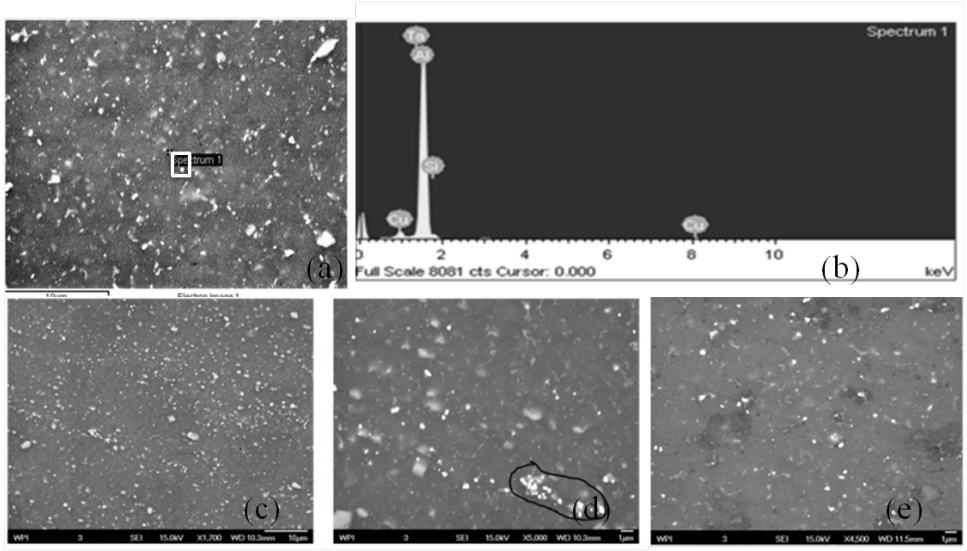

Figure 1. SEM/EDS analysis of the Ta-Al composite layer: (a) micrograph showing Ta inside the composite layer; (b) EDS analysis; (c) Ta distribution in the composite layer after 1-pass FSP; (d) agglomerations inside the composite layer after 1-pass FSP; (e) homogenous Ta distribution in the composite layer after 2-pass FSP.

The distribution of nano-sized SiC powders in the aluminum matrix was quite similar to that of Ta powders. Moreover, effects of multi-pass-FSP (up to two passes) and the amount of the mixing-in SiC powders were investigated. Fig. 2 shows three macrographs showing distributions of SiC in the FSP region under different experimental conditions. Each macrograph is a collage of 24 pictures. Fig. 2a was the optimal distribution, which was quite common after two-pass-FSP with 100% cavity filling (800 mm^3). However, compared with Fig. 2a, when fabricating the composite layer with only one-pass FSP (Fig. 2b), or reducing the amount of reinforced particles to 50% cavity filling (400 mm^3)

(Fig. 2c), the distribution deteriorated. It can be seen that multi-pass FSP ensured adequate material movement thus alleviating particle agglomeration (Fig. 2b); this was found to be the case no matter how many particles were mixed in (Fig. 2a and 2c). When depositing fewer amounts of the reinforcement particles, the particles were prone move towards the bottom of the FSP region; this resulted in the distribution seen in Fig. 2c. For all the experimental conditions that were performed in this study, we observed these trends.

Fig. 3 contains two optical micrographs of the metal matrix composite, which was fabricated by emplacing DRA into the aluminum matrix. In Fig. 3a, the interface zone between the surface composite layer and the aluminum substrate can clearly be seen; the composite layer appears to be well bonded to the aluminum substrate, and structural integrity is attained – no evidence of porosities or severe reinforcement agglomeration. Fig. 3b shows the distribution of SiC inside the composite layer at a higher magnification. Apart from the improved distribution, the morphology of SiC was also changed subsequent to FSP – the size was decreased to less than 10 μm, and aspect ratio to 1. The rotating probe produced a breaking effect on the SiC particles, resulting in the cracking of some large particles and the knocking off of corners and sharpened edges from the large particles [12].

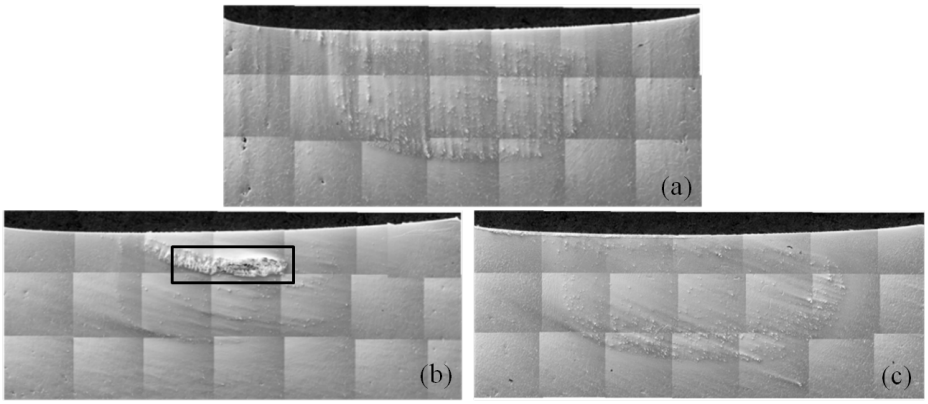

Figure 2. Macrographs of the SiC dispersion in the FSP region – effects of multi-pass FSP and the amount of the SiC particles: (a) 2-pass FSP with 100% cavity filling; (b) 1-pass FSP with 100% cavity filling; (c) 2-pass FSP with 50% cavity filling.

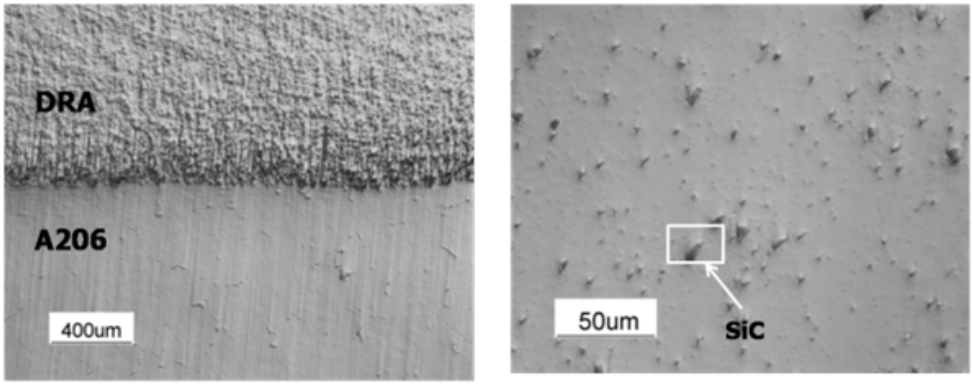

Figure 3. Optical micrographs of DRA/Al composite layer: (a) perfect bonding between surface composite and Al alloy substrate; (b) uniform distribution of DRA in Al alloy matrix.

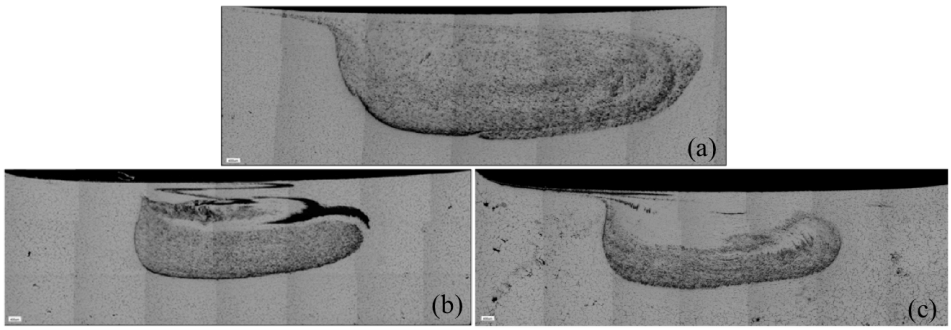

Figure 4. Macrographs of the DRA dispersion in the FSP region – effects of multi-pass FSP and the amount of DRA: (a) 2-pass FSP with 100% cavity filling; (b) 1-pass FSP with 100% cavity filling; (c) 2-pass FSP with 50% cavity filling.

Fig. 4 depicts effects of multi-pass FSP and the amount of emplaced DRA on morphologies of composite layers. It can be seen from Fig. 4 that the DRA distributed similar to how the SiC powders distributed in the aluminum matrix. It was obvious that the optical processing method for DRA-Al composite layer fabrication was two-pass FSP with 100% cavity filling.

SUMMARY

(1) FSP has emerged as an advanced post-processing tool to produce surface composites and synthesize second phase into the Al matrix in the solid state.
(2) Three different methodologies to fabricate the composite layer have been investigated: composite fabrication via FSP can be realized by mixing-in nano-sized Ta powders, mixing-in nano-sized SiC powders, and emplacing discontinuously reinforced aluminum in the cast aluminum matrix.
(3) Effects of process parameters have been explored. A good particulate distribution in the composite layer requires enough heat input, sufficient material wrapping

and plastic deformation during FSP; composite fabrication by two-pass FSP with 100% cavity filling is the optimum procedure in the current study.

ACKNOWLEDGEMENT

The authors gratefully acknowledge the member companies of the Advanced Casting Research Center for their support of this work, and for their continued support of research focused on the science and technology of metal casting at Worcester Polytechnic Institute.

REFERENCES

[1] W.M. Thomas, E.D. Nicholas, J.C. Needham, M.G. Murch, P. Templesmith, C.J. Dawes, GB Patent Application No. 9125978.8, December 1991.

[2] Y.J. Kwon, N. Saito, I. Shigematsu, Friction stir process as a new manufacturing technique of ultrafine grained aluminum alloy, Journal of materials Science Letters 21 (2002) 1473-1476.

[3] Z.Y. Ma, S. Sharma, R.S. Mishra, Microstructural modification of as-cast Al-Si-Mg alloy by friction stir processing, Metallurgical and materials Transactions A 37 (2006) 3323-3336.

[4] M.L. Santella, T. Engstrom, D. Storjohann, T.-Y. Pan, Effects of friction stir processing on mechanical properties of the cast aluminum alloys A319 and A356, Scripta materialia 53 (2005) 201-206.

[5] Z.Y. Ma, A.L. Pilchak, M.C. Juhas, J.C. Williams, Microstructural refinement and property enhancement of cast light alloys via friction stir processing, Scripta materialia, 58 (2008) 361-366.

[6] S.R. Sharma, R.S. Mishra, Fatigue crack growth behavior of friction stir processed aluminum alloy, Scripta materialia 59 (2008) 395-398.

[7] R.S. Mishra, Z.Y. Ma, I. Charit, Friction stir processing: a novel technique for fabrication of surface composite, Materials Science and Engineering A341 (2003) 307-310.

[8] W.Wang, Q.Shi, P.Liu, H.Li, T. Li, A novel way to produce bulk SiCp reinforced aluminum metal matrix composites by friction stir processing, Journal of Materials Processing Technology 209 (2009) 2099-2103.

[9] R.D. Doherty, D.A. Hughes, F.J. Humphreys, J.J. Jonas, D.J. Jensen, M.E. Kassner, W.E. King, T.R. McNelley, H.J. McQueen, A.D. Rollett, Current issues in recrystallization: a review, Materials Science and Engineering A 238 (1997) 219-274.

[10] D.C. Hofmann, D.S. Vecchio, Thermal history analysis of friction stir processed and submerged friction stir processed aluminum, Materials Science and Engineering: A 465 (2007) 165-175.

[11] A.H. Feng, B.L. Xiao, Z.Y. Ma, Effect of microstructural evolution on mechanical properties of friction stir welded AA2009/SiCp composite, Composites Science and Technology 68 (2008) 2141-2146.

APPENDIX E: *4th LMT Conference, Queensland, Australia, 2009*
Materials Science Forum, Vol. 618-619, p361-364, 2009

Microstructural Modification of A206 Aluminum via Friction Stir Processing

N. Sun and D. Apelian
Metal Processing Institute
WPI, Worcester, MA 01609 USA

ABSTRACT

Friction stir processing (FSP) is a post-processing method that locally manipulates the microstructure by imparting a high level of energy in solid state giving rise to improved mechanical properties. FSP was applied to 25.4 mm thick, sand casting A206 aluminum workpiece under different parameters. Effects of FSP on microstructure evolution will be described and discussed. Specifically, through Optical microscopy and SEM measurements the attained refinement in the stirred zone will be reviewed; porosity is significantly reduced and second phase particles are fragmented. Thermal conditions of the FSP zone have been measured as well as studying the effect of the temperature gradients on the resultant structure.

INTRODUCTION

Friction stir processing (FSP) is a solid-state, post-processing method, which was developed by The Welding Institute [1]. During FSP, a rotating column tool with a pin at the end is inserted into and traversed along the workpiece – see Figure 1; the main property of FSP is the combination of mechanical heat and plastic deformation. In the schematic diagram of the process, "A" refers to the advancing side and "R" refers to the retreating side of the workpiece. FSP can be used to refine the microstructure and to attain mechanical property improvements [2]. In addition, FSP can be used to fabricate composite structures on aluminum substrates [3], as well as to homogenize the microstructure of nanophased aluminum alloys [4]. Of these various applications of FSP, microstructural modification in both cast and wrought aluminum alloys has been the primary focus to date [2, 5-6]. Z.Y. Ma et al have studied the effects of FSP on the microstructure of cast A356 aluminum [7-9].

In this study we focus on microstructural modification of cast A206 via FSP. Cast A206 alloy has high strength and good machinability, however it has relatively poor fluidity and it is prone to hot tearing during solidification; moreover, it is susceptible to stress corrosion [10]. The motive behind this study was to ascertain whether FSP is an enabling

technology for post-processing of cast A206 components in order to enhance microstructure and properties.

EXPERIMENTAL PROCEDURES

Commercially cast A206 was acquired from Eck Industries in the T4 condition; the nominal composition of the alloy being Al-4.33Cu-0.077Si-0.046Fe-0.256Mg-0.343Mn. Single pass FSP was carried out and the dimensions of the workpiece were 15cm X 7.6cm X 2.54cm. The tool shoulder diameter is 16mm, with a screwed taper pin at its end. The length of the pin is 3.2mm. Three FSP conditions with different parameters (revolutions per minute and traverse speed) were investigated: 500RPM – 25.4mm/min; 1000RPM – 25.4mm/min; and 1000RPM – 50.8mm/min, respectively. A three degrees tilt angle was applied during processing. Samples were sectioned perpendicular to the FSP traverse direction. Barker's reagent was used as an etchant for metallographic analysis using both optical and scanning electron microscopy.

To study the temperature distribution under different FSP conditions, four K-type thermocouples were inserted into the retreating side of the workpiece to measure and record the thermal data; see Figure 1 for an explanation of the retreating versus advancing sides of the workpiece. The four thermocouples were accommodated in four 38 mm deep holes in the retreating side, 1mm away from the center of the FSP zone. The distance between the thermocouples was 25.4mm.

RESULTS AND DISCUSSIONS

Figure 1 shows macrostructure of the FSPed zone under different processing conditions. The shape of the FSPed zone changes from a basin-like shape at lower rotation speed (500 RPM) to an elliptical shape at higher rotation speeds (i.e., 1000 RPM), which agrees with experimental evidence in cast A356 [8]. At 500RPM-25.4mm/min (Figure 1 a), there is a visible area on the bottom of the advancing side (A), which is the banded structure and it is generated by the insufficient material flow. The banded structure is eliminated when the rotation speed is doubled - Figures 1 b; however, when the traverse speed is doubled (keeping a high rotation speed of 1000RPM), we observe an onion ring structure as shown in the middle of the nugget (Figure 1 c).

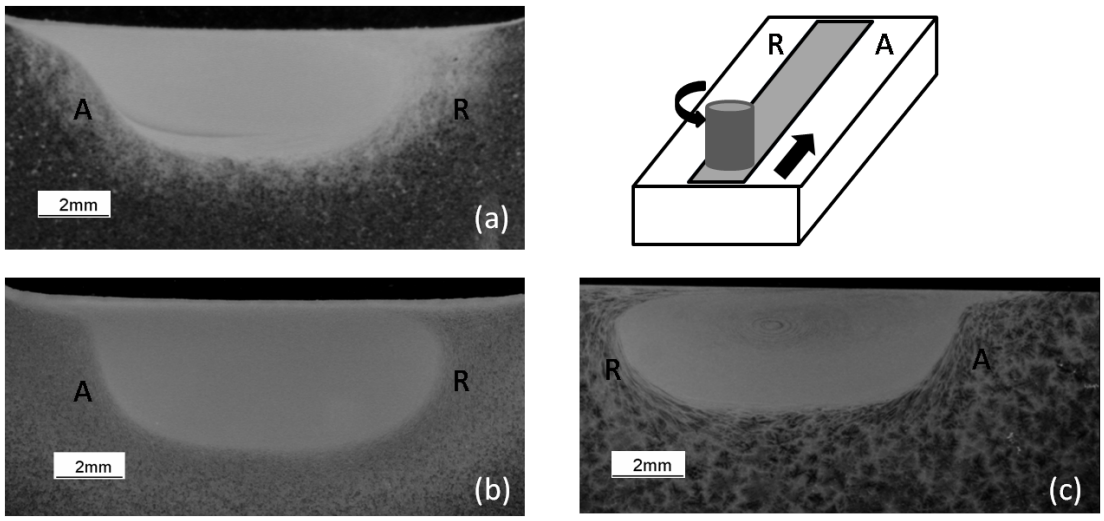

Figure 1. Macrographs of the friction stirred zone in different parameters: (a) 500RPM-25.4mm/min; (b) 1000RPM-25.4mm/min; (c) 1000RPM-50.8mm/min.

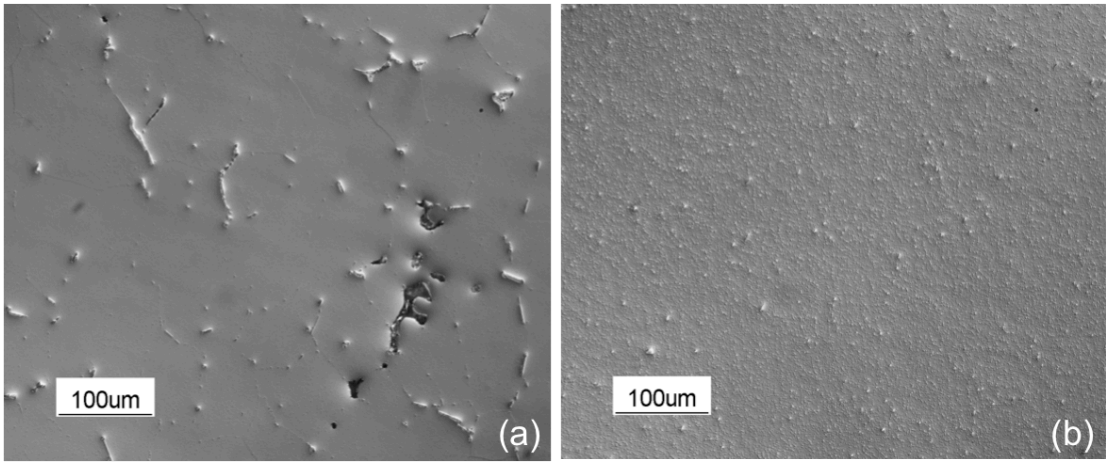

Figure 2. Microstructure of polished A206: (a) without FSP; (b) after FSP

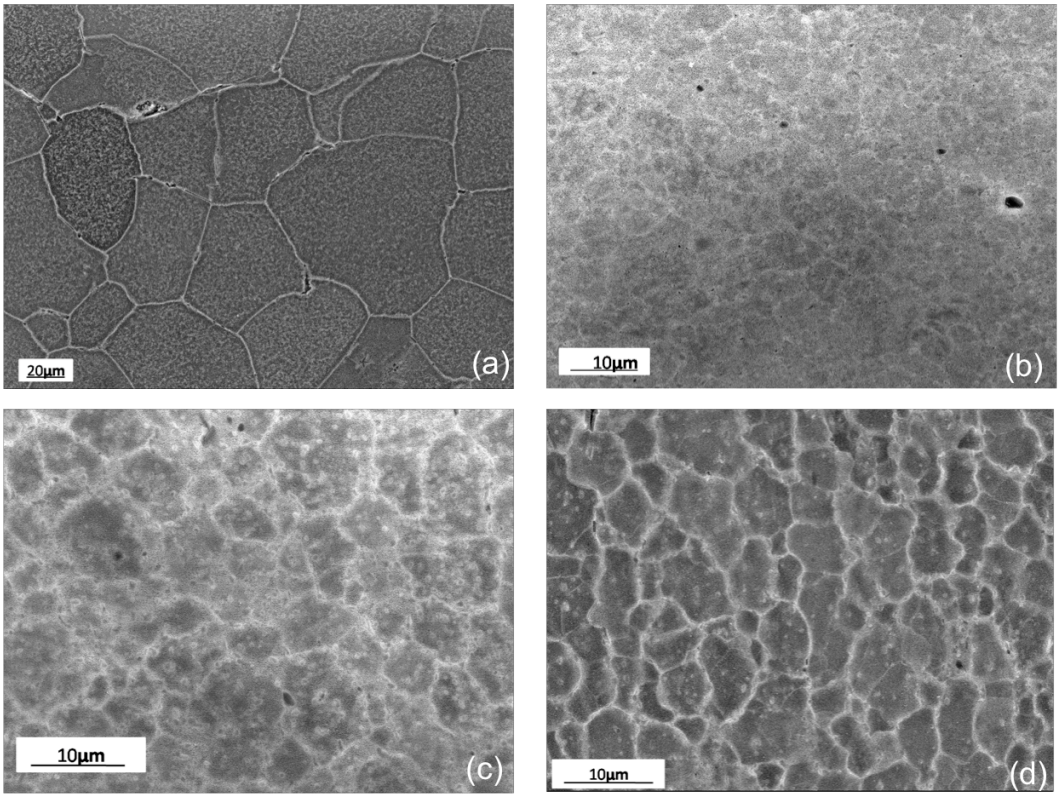

Figure 3. SEM micrographs of A206 grain size: (a) without FSP; (b) FSP 500 RPM-25.4 mm/min; (c) FSP 1000RPM-50.8mm/min; (d) FSP 1000 RPM-25.4mm/min.

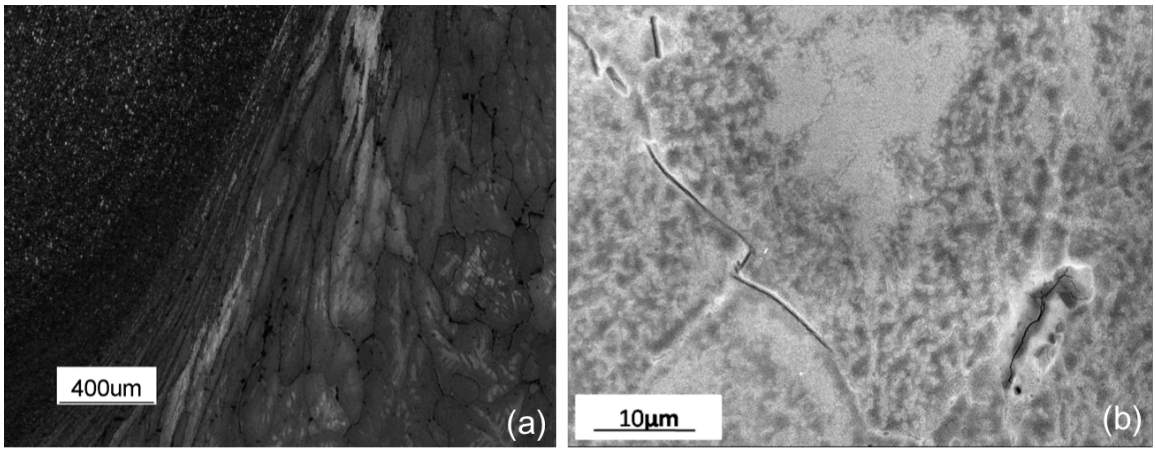

Figure 4. Microstructure of the TMAZ (1000 RPM-50.8mm/min): (a) OM; (b) SEM.

Figure 2 shows optical micrographs of a polished A206. Prior to FSP (Figure 2a), in the as-cast-T4 condition, porosity can be seen in the Al matrix (100-200 µm) as well as the expected coarse needle-like second phase particles. However, after FSP (Figure 2b), we observe a high density of fine and nearly equiaxed second phase particles uniformly distributed within the processed zone; moreover, structural integrity is attained by mitigation of the porosity. For all the experimental conditions that were performed in this study, we observed the same tendency.

Figure 3 are SEM micrographs of A206 showing the evolution of the grain structure during FSP. Without FSP (Figure 3a), the grain size of the as-cast-T4 A206 is ~100μm, but subsequent to FSP (Figure 3c and d), the grain size is decreased to less than 10μm. FSPed zones generated under the three experimental conditions give rise to different grain morphologies. No grains are observed when FSPed at 500 RPM-25.4mm/min; blurred grain boundaries are seen when FSPed at 1000 RPM-50.8 mm/min. In contrast, clear grains are seen when FSPed at 1000 RPM-25.4 mm/min.

It has been pointed out that the grain refinement during FSP is the result of dynamic recrystallization [7- 9]. When FSP conditions are at 500 RPM -25.4 mm/min, the temperature range is 306-354^{0}C; for FSP at 1000 RPM – 25.4-mm/min and 1000 RPM - 50.8 mm/min, the temperature range are 338-422^{0}C and 273-350^{0}C, respectively. When the rotation speed is 500 RPM, mechanical stirring is not sufficient to break up the original grains, however, when the rotation speed is doubled to 1000 RPM, the broken original grains are homogeneously dispersed and subsequently grow. It is clear that the temperatures attained when FSP processed at 1000 RPM – 25.4 mm/min gives rise to optimum conditions for recrystallization vis a vis the other two experimental conditions. In brief, it is the resultant temperature conditions that control nucleation and growth, and not necessarily rotation and traverse speeds.

The microstructure in the thermo-mechanically-affected-zone (TMAZ) has also been investigated. Elongated grains in this region suffer a severe shear force generated by the contact of the material with the lateral surface of the tool pin and the screw flake on the pin (Figure 4a). Specifically when FSPed at 1000 RPM- 50.8 mm/min, high forces exist in three directions giving rise to many torn boundaries as seen in Figure 4b.

CONCLUSIONS

(1) Friction stir processing modifies the microstructure of cast-T4 A206. Coarse needle-like particles are broken up and uniformly dispersed in the aluminum matrix. Grain size is refined from about 100 μm to less than 10 μm.

(2) The FSPed zone macrostructure is controlled by the traverse and rotation speed of the tool; the shape of the FSPed zone changes from a basin-like nugget to an elliptical one.

(3) Dynamic recrystallization is influenced and controlled by the temperatures attained during FSP. The latter is controlled by the rotation speed and traverse speed of the tool. In this study, it was found that 1000 RPM-25.4 mm/min offered optimum condition for grain refinement.

(4) The potential of locally manipulating the structure of cast components to attain enhanced performance via FSP are most promising.

REFERENCES

[1] Thomas W.M. et al. (1991) International Patent Application Number PCT/GB92/02203 and GB Application Number9125978.8.

[2] Sutton M.A., Yang B., Reynolds A.P., & Taylor R. (2001) Microstructural studies of friction stir welds in 2024-T3 aluminum. Materials Science and Engineering A323, 160-166.

[3] Mishra R. S., Ma Z. Y. & Charit I. (2003) Friction stir processing: A novel technique for fabrication of surface composite. Materials Science and Engineering A, 341(1-2), pp. 307-310.

[4] Berbon P.B., Bingel W.H., Mishra R.S., Bampton C.C. & Mahoney M.W. (2001) Scripta Mater. 61.

[5] Su J.-Q., Nelson T.W. & Sterling C.J. (2006) Grain refinement of aluminum alloys by friction stir processing. Philosophical Magazine, Vol.86 No.1, 1-24.

[6] Kwon Y.J., Saito N. & Shigenatsu I. (2002) Friction stir process as a new manufacturing technique of ultrafine grained aluminum alloy. Journal of materials science letters 21, 1473-1476.

[7] Mishra R.S., Ma Z.Y., Sharma S.R. & Mahoney M.W. (2006) Microstructural modification of cast aluminum alloys via FSP.

[8] Ma Z.Y., Sharma S.R. & Mishra R.S. (2006) Effect of friction stir processing on the microstructure of cast A356 aluminum. Materials Science and Engineering A433 269-278.

[9] Ma Z.Y., Sharma S.R. & Mishra R.S. (2006) Effect of multiple-pass friction stir processing on microstructure and tensile properties of a cast aluminum-silicon alloy. Scripta Materialia 54, 1623-1626.

[10] Jorstad J.L. & Apelian D. (2008) High integrity die castings. NADCA publication #404.

ACKNOWLEDGEMENTS

The authors gratefully acknowledge the member companies of the Advanced Casting Research Center (ACRC) for their support of this work, and for their continued support of research focused on the science and technology of metal casting at Worcester Polytechnic Institute.

Appendix F: *Listing of all presentations/proceedings made*

"Localized Microstructure Enhancement via FSP for Die Casting Components", Ning Sun and Diran Apelian, High Tech Die Casting, Vicenza, Italy, accepted by La Metallurgia Italiana, 2012.

"FSP for Localized Strengthening of Die Cast Components", Ning Sun and Diran Apelian, NADCA Congress and Exposition, Indianapolis, IN, USA, 2012.

"Localized Strengthening of Cast Aluminum A206 via FSP", Ning Sun and Diran Apeian, American Foundry Society Annual Conference, Columbus, OH, USA, 2012.

"Defect Elimination of Cast Aluminum A206 Alloy via FSP", Ning Sun and Diran Apelian, TMS Annual Meeting, Orlando, FL, USA, 2012.

"Friction Stir Processing of Aluminum Cast A206 Alloys for High Performance Application", Ning Sun and Diran Apelian, Journal Of metal, Mineral and Materials, vol. 60, No. 11, pp. 44-50, 2011.

"Composite Fabrication via FSP", Ning Sun and Diran Apelian, 5th International Light Metals technology, Hamburg, Germany, 2011, published on Materials Science Forum, Vol. 690, pp. 125-128, 2011.

"Characterization of Composite Fabrication via Friction Stir Processing: Methodology and procedures", Ning Sun and Diran Apelian, MS&T Annual Meeting, Houston, TX, USA, 2010.

"Microstructure Modification of A206 Aluminum via Friction Stir Processing", Ning Sun and Diran Apelian, 6th International Light Metals technology, Queensland, Austrilia, 2009, published on. Materials Science Forum, Vols. 618-619, p361-364, 2009